

# **Gas sensors for detection of volatile organic compounds at room temperature**

Air quality control & medical diagnosis

**Quyen Nguyen Minh**

## **Thesis committee**

### **Promotor**

Prof. Dr C.J.M. van Rijn

Special Professor Microsystem and Nanotechnology for Agrofood and Health

Wageningen University & Research

### **Other members**

Prof. Dr W. G. van der Wiel, University of Twente, Enschede

Dr N. R. Tas, University of Twente, Enschede

Prof. Dr E. J. R. Südhofter, Delft University of Technology

Prof. Dr E. J. Woltering, Wageningen University & Research

This research was conducted under the auspices of the Graduate School VLAG (Advanced studies in Food Technology, Agrobiotechnology, Nutrition and Health Sciences).



# **Gas sensors for detection of volatile organic compounds at room temperature**

Air quality control & medical diagnosis

**Quyen Nguyen Minh**

## **Thesis**

submitted in fulfilment of the requirements for the degree of doctor

at Wageningen University

by the authority of the Rector Magnificus,

Prof. Dr A.P.J. Mol,

in the presence of the

Thesis Committee appointed by the Academic Board

to be defended in public

on November 1<sup>st</sup> 2017

at 4 p.m. in the Aula.

Q. Nguyen Minh

*Gas sensors for detection of volatile organic compounds at room temperature for air quality control and medical diagnosis*

180 pages.

PhD thesis, Wageningen University, Wageningen, the Netherlands (2017)

With references, and summary in English and Dutch

ISBN: 978-94-6343-704-2

DOI: <https://doi.org/10.18174/423305>

## Table of contents

<b>Chapter 1</b>	General Introduction	<b>7</b>
<b>Chapter 2</b>	Fluorinated Alkyne-derived Monolayers on Oxide-free Silicon Nanowires via One-step Hydrosilylation	<b>33</b>
<b>Chapter 3</b>	Preparation and Gas Sensing Properties of Nanocomposite Polymers on Micro-Interdigitated Electrodes for Detection of Volatile Organic Compounds at Room Temperature	<b>57</b>
<b>Chapter 4</b>	Excellent Gas Sensing Performance at Room Temperature of Nanogap Interdigitated Electrodes for the Detection of Acetone at Low Concentration	<b>77</b>
<b>Chapter 5</b>	Improving Detection Limit in Capacitive Sensor Systems	<b>99</b>
<b>Chapter 6</b>	General Discussion	<b>121</b>
	Appendix A	<b>135</b>
	Appendix B	<b>150</b>
	Appendix C	<b>162</b>
	Appendix D	<b>165</b>
	Summary	<b>169</b>
	Samenvatting	<b>171</b>
	Acknowledgements	<b>173</b>
	Author biography	<b>175</b>
	List of Publications	<b>177</b>



# Chapter 1



## General Introduction

Nanotechnology will not only be effective in getting advantageous properties of materials and structures at the nano-scale but it will also minimize the total size of the devices (miniaturization). Supported by NanoNextNL, this thesis focuses on the investigation and development of devices based on nanotechnology for health care and real-life applications. Specially, this thesis will focus on gas sensors from two approaches: air quality monitoring for human safety and medical diagnosis using nanotechnology. Some background information on the necessity of gas sensors in industries and medical diagnosis, nanowire field effect transistor based gas sensors and chemocapacitive gas sensors for the detection of acetone will be presented in this chapter.

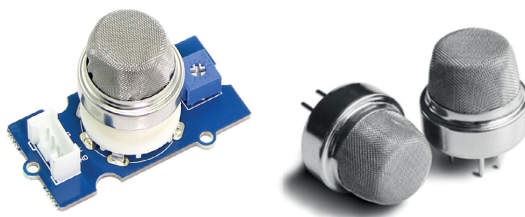
### 1. Air quality control in laboratory, manufactory, warehouse, etc.

Issues regarding to air pollution are drawing most society and scientists' attention with the development of various modern industries. The rise of modern industries leads to the atmospheric air containing numerous types of natural and artificial chemical species.[1] Some of these species are vital to our lives while others are considerably harmful to human health. To improve the quality of our lives, the application of gas sensors is critically essential to control the contents of hazardous gases in the atmosphere: air pollution caused by industry and exhausted gases from automobiles; or environmental monitoring during manufacturing process and in laboratories for human safety. Asphyxiation, explosions and human health damage are critical incidents related to dangerous substances, toxic and combustible gases during industrial processes and manufacture. Gas sensors are essential in manufacturing of many industries (**Figure 1**), they play an important role in the prevention of the previously mentioned issues in various modern technology processes where the detection, analysis and control of gases are necessary.[2] These gases include both organic and inorganic compounds that are oxygen-deficient and harmful to human health and ecological system such as CO, CO<sub>2</sub>, SO<sub>2</sub>, NO<sub>2</sub>, CH<sub>4</sub>, C<sub>3</sub>H<sub>8</sub>, ketone, alcohol and other volatile organic compounds (VOCs), etc.



**Figure 1.** Chemical sensors are widely used in many industries.

It is very important to study gas-sensing performance towards these VOCs for air quality control in industrial manufacturing process and laboratories. Developments of gas sensors with high gas sensing performances have attracted considerable attention, many studies has been conducted for the detection of toxic, hazardous, flammable and explosive volatile gases.[3–5] Gas sensors for VOCs can detect an amount of combustible and flammable gases to a greater or lesser extent. Thus, such sensors can be able to sound the alarm to prevent accidents due to gas leakages in gas containers, oilrigs and trunk pipelines and they are highly attractive for gas “on-site” monitoring in industries.[6] In laboratories, gas sensors can be used as powerful supports in emergency rescue for monitoring air quality, gas purity and sensing dangerous gas leakages. This helps to save human lives and expensive equipment and sophisticated systems.



**Figure 2.** Air quality sensor type MQ5 and VOC sensors MQ138 for IAQ monitor application (Winsen Electronics) as incorporated components in many gas detecting systems and their compatible PCB for computer controlling systems.

Acetone, one of the most common volatile organic compounds, is commonly investigated both in biological and environmental samples, and has been widely used for most synthesis as reaction reagent, solvent and cleaning agent, etc. It is nontoxic at a low concentration ( $\leq 10\,000$  ppm), however acetone can cause harm and danger to human health when the concentration exceeds to a certain amount and can also affect environmental safety. A high amount of acetone can cause several syndromes to human body such as fatigue, headache

and nausea when being inhaled,[7] irritated eyes and skin or damage throat when being exposed when its concentration above 10 000 ppm.[8,9] Therefore, it is highly essential and significant to effectively detect acetone gas in different ranges of concentration, especially in industry, in-house environment such as laboratories and warehouses. Gas sensors that can detect numerous VOCs or toxic gases are of great importance. By evaluating and controlling the composition of the air these devices make it possible to control the quality of the surrounding atmosphere. Various methods have been developed for the determination of acetone in air. A few examples of commercial gas sensors used in air quality control are given in this chapter. **Figure 2** shows an example of gas sensors used as incorporated components in gas detecting systems from Winsen Electronics. For instance, MQ138 sensor is developed with  $\text{SnO}_2$  as sensitive material, which has lower conductivity in clean air. Upon exposure of VOCs, the sensor's conductivity gets higher along with the gas concentration rising. Users can convert the change of conductivity to correspond output signal of gas concentration through a simple circuit. This gas sensor has high sensitivity to toluene, acetone, alcohol, methanol, also can monitor hydrogen and other combustible and flammable VOCs. It is a type of low-cost sensor for many gas sensing applications. In **Figure 3**, other types of gas sensor as hand-held devices are introduced. This has great advantages in environment control because of its compact and portable properties.





**Figure 3.** Several examples of gas sensors operating as hand-held devices for common gases such as natural gas; propane; butane; methane; acetone; alcohol; ammonia; steam; carbon monoxide; gasoline; jet fuel; hydrogen sulfide; smoke; industrial solvents; lacquer, etc. (i.e. from Logoele Electronic, REED).

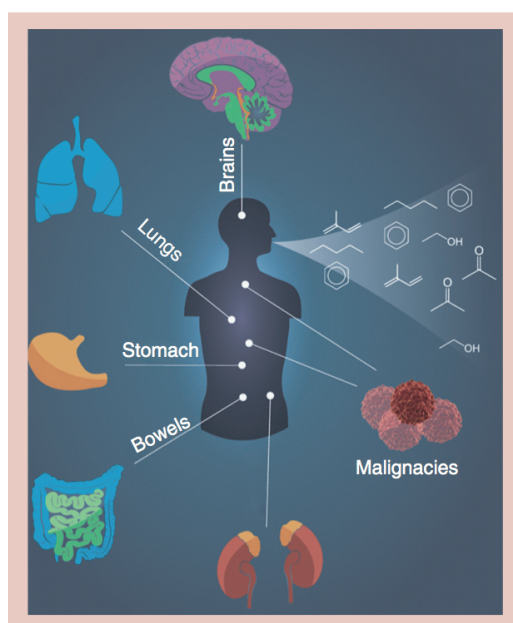
Not only being widely used for in-house air quality control but acetone sensors has been further exploited for medical diagnosis as well. A number of recent investigations prove that acetone, as one of the biomarkers in human breath; represents for diabetes diagnosis because of its change in concentration can be an indication of diabetes.[10]

## 2. Acetone as a biomarker in medical diagnosis for Diabetes

### *VOCs in diseases prognosis and diagnosis*

Breathing is one of the most common and most important functions of human organisms. Our exhaled breath is a mixture of inorganic compounds and volatile organic compounds (VOCs) with concentrations ranging from part per billions (ppb) to part per millions (ppm) (in one standard volume from nano-mole to micro-mole concentration of species). Some inert gases in our breath are, for instance,  $N_2$ ,  $O_2$ ,  $CO_2$ ,  $H_2O$  and thousands of other trace

gases.[11,12] These exhaled breath gases include inorganic molecules such as NO, NH<sub>3</sub> or CO and VOCs such as acetone, methanol or isoprene, etc. The VOCs are products of core metabolic processes[13] and are related to health conditions, or may reflect a potential disease of the individual or a recent exposure to a drug or an environmental pollutant.[14] Ever since the century of Hippocrates many scientists have studied and used the difference among these trace gases, organic and inorganic compounds in human breath to recognize many diseases. An abnormality in the concentration of certain trace gases could provide essential clues to diagnose corresponding diseases. For example, a smell of ureum in the breath is associated with kidney failure, a fishy smell is considered as a result of liver malfunctioning, and a sweet odor of acetone in human breath is directly related to diabetes. An early physician word for diabetes is acetone. **Table 1** shows a list of potential biomarkers together with their physiological origin of related diseases, which have been investigated in the 18th-19th century.[15,16]



**Figure 4.** Links between volatile organic compounds, various organs in the human body and exhaled breath samples.[17]

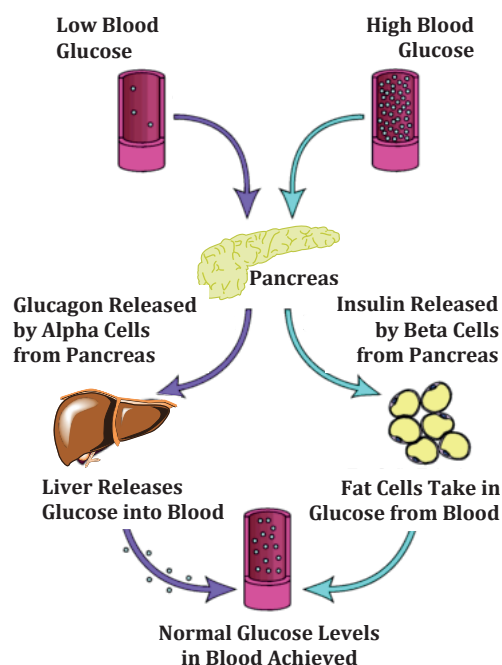
**Table 1.** Some biomarkers and their related diseases with recognition of physiological ranges in human breath collected by statistical medical research.

Biomarkers	Physiological origin	Related diseases	Physiological ranges in human breath
<b>Ethane</b>	Lipid peroxidation	Oxidative stress	1-11 ppb
<b>Pentane</b>	Lipid peroxidation	Oxidative stress	Less than ethane
<b>Isoprene</b>	Cholesterol biosynthesis	Cholesterol	55-121 ppb
		metabolic disorder	12-580 ppb
<b>Acetone</b>	Decarboxylation of acetoacetate and acetyl-CoA	Diabetes mellitus	293-870 ppb
		ketonemia	1.2-1880 ppb
<b>Ethanol</b>	Alcohol ingestion	Alcohol poisoning	27-152 ppb
			13-1000 ppb
<b>Methanol</b>	Degradation of natural pectin from plants; ingestion	Methanol Intoxication	160-2000 ppb
<b>NH<sub>3</sub></b>	Metabolic product of amino acid	Uremia,	422-2389 ppb
		Kidney impairment	200-1750 ppb
<b>CO</b>	Inhalation from incomplete burning of carbon containing fuels, e.g. smoking	Lung diseases	<6 ppm
<b>NO</b>	L-arginine oxidation	Asthma, lung diseases	1-9 ppb, lower respiratory
			0.2-1 ppm, upper respiratory
			1-30 ppm, nasal level

With these biomarkers, scientists have studied and developed many types of sensor based on breath analysis to help early disease diagnosis.

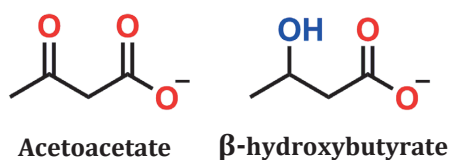
***Acetone as breath marker in Diabetes diagnosis (the relation of acetone to blood glucose level)***

In the human body, endogenous products are excreted in the blood and transported to all tissues and organs of the body for normal activities. When starving or during diet, glucose in the blood is decreasing. Glucagon is released by alpha cells from pancreas and liver tissue releases glucose backward to blood and achieves normal glucose level in blood that is used as a source of energy. In normal conditions, ketone bodies occur almost entirely in both liver, kidney and lung with a small amount. Fasting, diabetes mellitus and strenuous exercise increase the endogenous generation of ketone bodies. If the glucose level in blood increases drastically, pancreas will release insulin by Beta cells as a signal for fatty cells to take in glucose from the blood. The main function of insulin is to help glucose move from digested food to enter into cells efficiently (glycogenesis). Sometimes, the body stops making insulin (so-called type-1 diabetes), or the insulin does not work properly (type-2 diabetes). It happens when the metabolism of the body breaks down, the lack of insulin producing from pancreas for type-1 as well as in type-2, fatty cells cannot take in glucose from blood normally thus glucose still stays in the blood then causes the problem as high blood sugar level. As a product of this failure process, an extent amount acetone is formed by decarboxylation of acetoacetate, which derives from lipolysis or lipid peroxidation (see **Figure 5**).



**Figure 5.** Body metabolism in both low and high sugar level in blood.

Together with acetoacetate and  $\beta$ -hydroxybutyrate, acetone occurs naturally throughout the body, which can be formed in the mammalian body from fatty acid oxidation. In this process endogenous acetone is produced by hepatocytes via decarboxylation of excess Acetyl-CoA.[18] Acetone is eliminated from the body either by excretion in urine and exhaled breath or by enzymatic metabolism. Two of these ketone bodies, acetoacetate and  $\beta$ -hydroxybutyrate, are organic acids that can cause metabolic acidosis when produced in large amounts, known as diabetes mellitus.



For diabetic patients, insulin deficiency accelerates the movement of free fatty acids in adipose tissues. A process called intrahepatic metabolism in the body then shifts from fat synthesis to fat oxidation and ketogenesis. Excessive ketone bodies, acetoacetates, from ketogenesis are spontaneously decarboxylated to form acetone and leads to the acetone noticeable concentration in human breath as a result.[19]

The ‘sweet and fruity odor’, a common feature of ketosis of the breath originates from acetone. The average concentration of acetone for a healthy human body is believed to be lower than 0.8 ppm and for diabetic patients higher than 1.8 ppm in their breathe.[20] Therefore, acetone has been widely accepted as a biomarker of diabetes, especially in type-1 of diabetes[15,21] and in the first stage of diabetes diagnosis for type-2.

For diabetic patients, there are many ways to examine whether the glucose level in their blood is abnormal or not. One of the most common and efficient methods is to check the glucose level in patient’s blood by a device known as blood-tester, so-called glucose monitoring device, which has been investigated and improved in the last decade. By pricking a drop of blood from the finger of a patient the glucose level in the blood can be obtained. With the range of glucose level from 100-125 mg/dL or above, it is believed that the patient has pre-diabetes, whereas a healthy human body has a glucose level from 60-100 mg/dL. Result from this quick test, patients can determine if they need further medical treatment such as an insulin injection. Puncturing of the finger is painful with a risk of infection for all diabetic patients. It is no doubt that scientists and researchers have taken these disadvantages as the motivation to search for non-invasive techniques to monitor glucose in diabetic patients’ blood since the first commercial glucose testing devices in the 1970s.[22] The new breath analyzing technique is a non-invasive and indirect glucose determination for diabetes diagnosis.

The correlation between concentration of acetone in patients’ breath and the glucose level in their blood has been studied for years. Acetone detection has to satisfy a sensitivity requirement up to 0.1 ppm accuracy. Beside the sensitivity, a good selectivity is required for detecting acetone amongst two hundred other VOCs in the breath. For instance, alcohol and isoprene are also VOCs, which have similar hydrocarbon properties as acetone, and this will make detection of acetone among these organic compounds more difficult. Or

water vapor in human breath is also a complicating factor. Studies have shown a reduced concentration of key VOC's due to their absorption into water condensate in the collective apparatus.[12] Stability of devices is also needed in breath analyzing sensors to ensure all parameters involving gas detection under different environmental conditions still maintain their values and selectivity to distinguish target gas among others exhaled gases.

Therefore, it is necessary to develop a gas-sensor type with high selectivity, sensitivity, fast response and high stability.

### ***Principal requirement for gas sensors***

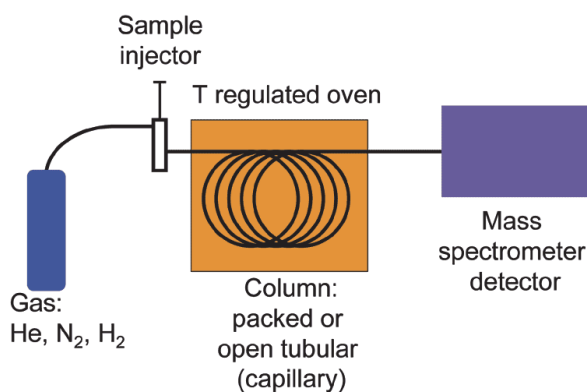
The most important features for gas sensors are sensitivity, response time, minimum detectable gas concentration, reproducibility, repeatability (recovery method, recovery time), and selectivity.

- a) Sensitivity: The sensitivity is defined as the ratio of measured parameters after exposure to the detected gas.
- b) Selectivity: Whether the sensor can give a significant signal for a given specific gas.
- c) The minimum detectable gas concentration: The lowest gas concentration that can be detected.
- d) Repeatability: The gas sensors have to be reused many times.
- e) Recovery method: The method used to allow the sensor to return to the original state after sensing gases.
- f) Recovery time: The time duration for the parameter to return to its original value.
- g) Response time: The time duration for the parameter to change by a certain percentage of its original value.

### ***3. Acetone detection: From conventional methods to a portable analyzing platform***

Sensing mechanism of most gas sensors studied is based on electro-transduction. Some other gas sensors have been reported based on photoluminescence spectroscopy and others based on the adsorbed mass using a quartz crystal microbalance. Current methods have been utilized to analyze trace compound in human exhaled breath including *Gas Chromatography* (GC) with flame ionization detection (FID),[23] *Mass Spectrometry* (MS),

or *Ion Mobility Spectrometry* (IMS).[24] IMS can also be integrated with MS to become IMMS for enhancement of each other efficiency and accuracy. IMMS can become a powerful technique in identification of molecular structure and separate such complex composition in the samples. Many studies have proved that IMMS, with its sourcing power, the region around 50 to over 100 ppm can be detected the same range in comparison with capillary gas chromatography (GC).[25] It is because of humidity negative effect to the GC column damage, these methods still need to extend pretreatment steps of the testing breath before analysis.[26] Lately, *Selected Ion Flow Tube Mass Spectrometry* (SIFT-MS)[27,28] has been investigated and it shows great potential on real-time concentration monitoring of several breath markers such as acetone, ethanol, ammonia and isoprene. With major advantage in high selectivity, sufficient sensitivity, low limit detection as a standard diagnostic tool, SIFT-MS however still presents its disadvantages in high cost and limited portability as they usually involve measurements with in-situ sampling on sorption tubes, desorption with a solvent flow and the determination and analysis is only possible in laboratories.[29]



**Figure 6.** Schematic illustration of GC-MS technique

*Proton Transfer Mass Spectrometry*, (PMT-MS) is promising to be able to analyze extremely low concentrations of analyte down to a few part per trillion (ppt). The mechanism of this technique depends on protonation of the chemical species, which come



from transfer of protonated water. This is because almost all VOCs have proton affinities greater than water; hence, there is a complete transfer.[30] The advantage of this method is that water does not interfere with gases such as NO, CO<sub>2</sub>, O<sub>2</sub>. Usually coupled with GC, PMT-MS shows its potential in increasing its accuracy for additional separation.[31]

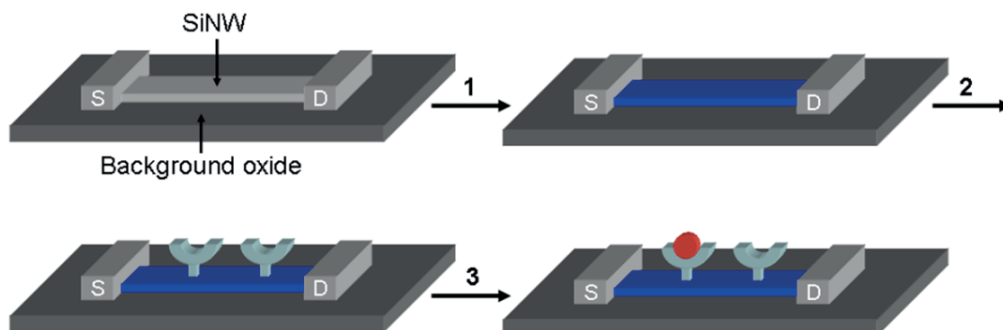
During the last forty years, the identification of VOCs in exhaled human breath has attracted many researches in analytical chemistry for its application in disease prognosis and diagnosis. However, there are still many requirements that need to be obtained such as the ability to detect multiple analytes at the same time and obtain sensitivity of devices down to trace concentration ppb in variable environments.[32]

### **3.1. Metal-oxide semiconductor gas sensor**

While conventional methods in laboratory are time-consuming, costly, and complex to use, and also not permit direct sample monitoring, another common trend to be applied to solve these issues is using metal oxide semiconductors (MO<sub>x</sub>). Having been widely investigated as materials of choice, MO<sub>x</sub> gas sensors can be developed with, for instance, SnO<sub>2</sub>[33,34], WO<sub>3</sub>[35,36], TiO<sub>2</sub>[33,37] and ZnO[37,38] as sensing materials. Further than that, a numerous diversity of these metal oxides are widely studied for acetone detection using nanotechnology such as hydrothermal synthesized SnO<sub>2</sub>-reduced graphene oxide hybrid composite[39]; Ag-decorated SnO<sub>2</sub> hollow nanofibers[40]; cuboid WO<sub>3</sub> nanosheets[41]; TiO<sub>2</sub> nanorods decorated with NiO nanoparticles[42]; p-Type Na:ZnO nanoflowers[43]; α-Fe<sub>2</sub>O<sub>3</sub> nanoparticles[44] or porous ZnFe<sub>2</sub>O<sub>4</sub> nanospheres[45] and W-doped NiO hierarchical nanostructure[46], etc. Some of these sensors demonstrate good detection sensitivity and robustness, and also, they are further developed to monitor a variety of toxic and inflammable gases (i.e. methanol, ethanol, isopropanol, acetone and acetic acid) in many air monitoring systems, gas leak detectors in industries and medical diagnosis equipment.[47] MO<sub>x</sub> sensors have shown their great competitiveness in fabrication costs but brought along other drawbacks. For example, generally they require external heating elements or energy excitement (UV) in their sensor structures and thereby, may suffer from poor stability and long recovery time. This leads to additional energy use during gas measurements.

### **3.2. Nanowire field effect transistor gas sensor**

An important class of gas sensors is based on a change in electrical conductivity of a metal oxide surface layer due to the adsorption of gas molecules. The semiconductor metal oxides contain lattice defects due to an excess or deficiency of metal or oxygen in the lattice. Association of electrons within these defects following chemisorption of the analyte allows a certain change of the electrical conductivity of the metal oxide. For polycrystalline ceramic or thin film devices, only a small fraction of the species adsorbed near the grain boundaries is active in modifying the electrical transport properties. This results in a lower sensitivity of the device because of the limited surface-to-volume ratio.[48] Moreover, most solid-state thin film devices operate at high temperatures (200 – 600 °C) to achieve enhanced chemical reactivity between sensing materials and targeted gases.[49] One-dimensional (1D) nanostructures, such as nanowires, have initiated intensive research due to their unique properties and their potential for fabrication at nano scale in miniaturized portable devices. 1-D systems have the smallest dimension structure that can be used for efficient transport of electrons, they also have a high surface-to-volume ratio and may display quantum effects so that their electrical properties are strongly influenced by minor adsorption of the analyte. The charge transport in 1D nanostructure potentially enables the detection of a single target molecule. 1D nanostructures provide a sensing model for label-free and direct electrical read-out when nanostructure is employed as a semiconducting channel in a *field-effect transistor (FET)* configuration.[50] The so-called nanowire FET sensors have an advantage over resistor-based sensors because the response can be easily amplified due to current modulation by gate electrode. Furthermore, the control on charge carrier density by the gate electrode can be exploited to increase sensitivity. Nanowire FET sensors also exhibit excellent signal-to-noise behavior. This is of great value for clinical diagnosis and other sensitive bio-detection applications. This type of sensors opens new capabilities, which are not available in large scale devices, such as studying single molecule properties, detecting a very small amount of analytes in the range of ppb to ppm, etc.



**Figure 7.** Schematic representation of a SiNW-based device (top-left), of which the nanowire has been chemically modified (step 1), followed by the immobilization of receptors (step 2) and the binding of an analyte (step 3). S and D stand for source and drain, respectively.[51]

To date, a variety of materials have been used for 1-D gas sensors such as CNT, Si, SnO, ZnO, In<sub>2</sub>O<sub>3</sub> nanowires and graphene.[11,15,18–21,23] However, Si-NWs have a unique place in the development of portable analyzing platform research because silicon is one of the most characterized materials with respect to structure, size and electronic properties that can be controlled in a reproducible way.

Therefore, part of this thesis will discuss on studying and developing Gas sensors as SiNW based FETs for acetone detection in diabetes.

### 3.3. Chemocapacitor gas sensor

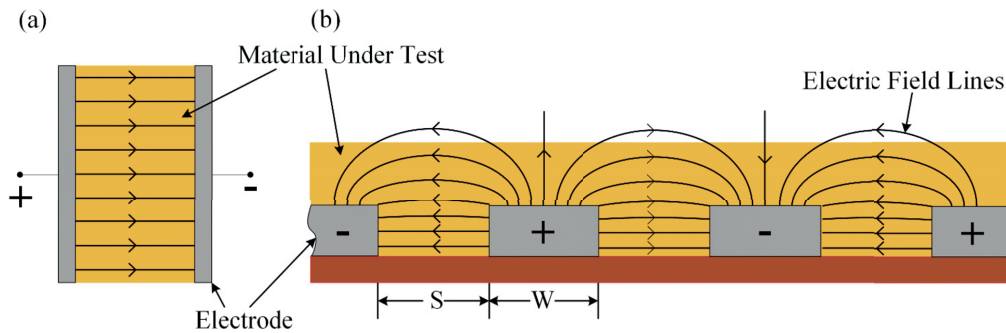
As one of the electrical detection methods, capacitive sensing has been exploited for many different applications,[52–54] such as displacement sensors,[55] humidity sensors,[56] acceleration sensors,[57] pressure sensors[58] and finger print sensors,[59] etc. Notwithstanding, capacitive gas sensors have been employed for the detection of organic and inorganic compounds for many purposes.[60–65]

Capacitive sensors are well known for its simplicity, given by comb-like or ring-like structure of multiple pairs of interdigitated electrodes (IDEs) using micro-fabrication

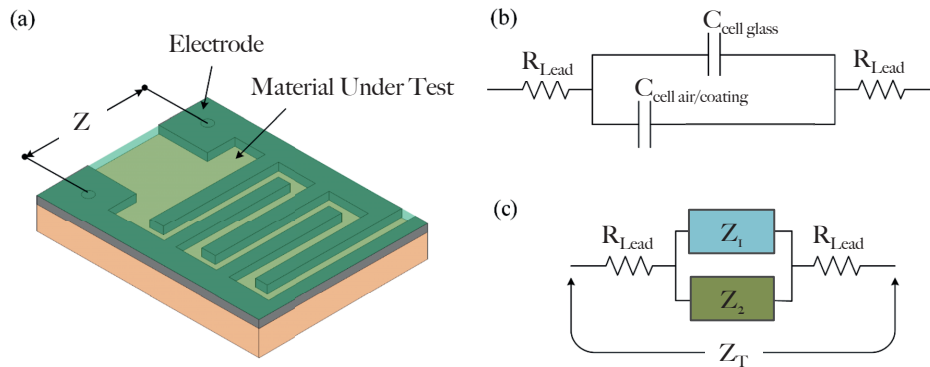
process. IDEs show great advantages because of its design and its surface can be functionalized in sensing applications. In principal, IDEs consist of many arrays of parallel plate capacitors.[66] The capacitance of a parallel-plate capacitor can be described using the conventional parallel-plate capacitor formula as below:

$$C = \epsilon \frac{A}{d} \eta \quad (1)$$

Where  $C$  is the capacitance,  $\epsilon$  is the relative permittivity of the material multiplied by the permittivity of the vacuum,  $A$  is the electrode area which is finger length times finger width,  $(l \times w)$ ,  $\eta$  number of fingers and  $d$  is the distance between plates which corresponds to the gap between electrodes in a planar capacitor. The larger  $\epsilon$  is, the larger the resulting capacitance becomes. Different sensing targets with different relative permittivity leads to change in capacitance when an analyte is being exposed. A schematic explanation of this approximation is shown in **Figure 8** and **Figure 9**.

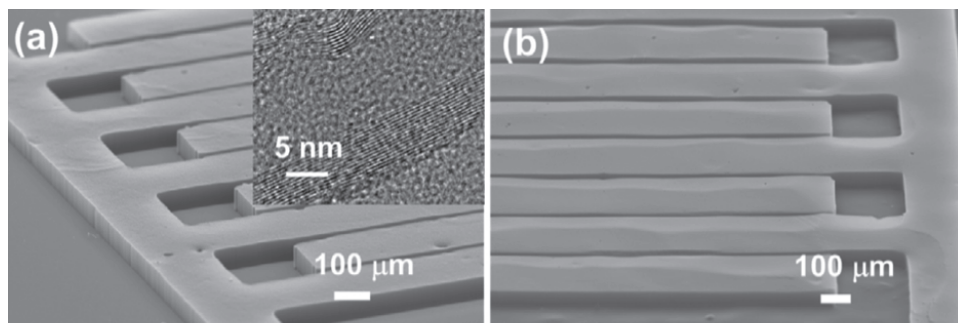


**Figure 8.** Top view of a basic IDEs and the electric field lines distributed between each fingers. Electric fields of the (a) parallel plate capacitor and (b) co-planar interdigitated sensor. The electric field emanating from the surface of the microelectrodes provides determination of the change in capacitance due to the change in dielectric properties above the surface.[67]



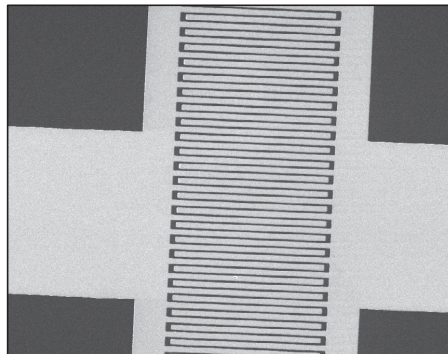
**Figure 9.** Interdigitated electrode: (a) configuration of the interdigitated impedance cell; (b) simplified electrical circuit of the interdigitated impedance cell; and (c) analogy of Figure 8b (previous figure).[67]

The fabrication of IDEs employs great potential in micro and nano-electronics because of its cost-effectiveness and large-scalability in industries. IDEs can be widely used for sensing applications in many different ways. For instance, as a chemoresistor, they can be used as a gas-sensing platform,[68] a humidity sensor,[69] or an integrated DNA chip with microfluidics channels.[70] For biological purposes, IDEs can also be exploited as a very effective sensor for impedimetric detection, which measures the change of impedance instead of resistance.[71,72]



**Figure 10.** SEM images of (a) the as-grown pattern, (b) the CNT pattern after transfer and inversion used as a supercapacitor.[73]

Furthermore, with conventional micro-fabrication process, micro IDEs and nanogap IDEs exhibit their excellence in large scalability, thus promises a new generation of cost-effective and portable devices (**Figure 10** and **Figure 11**).



**Figure 11.** A SEM image of an interdigitated capacitor for acetone sensor at room temperature.[74]

#### 4. Aim of this Research

Despite the fundamental scientific relevance of acetone sensing, many questions remain unanswered. How can surface functionalization alter the properties of silicon nanowire

channel in field effect transistors with respect to sensing performance of a gas sensor? How does the polarity / surface energy of the monolayer on silicon nanowires change when acetone molecules are present? Which problems need to be dealt with when developing an acetone gas sensor at room temperature? How can acetone be detected by a non-conductive polymer? In which ways we can develop sensing materials to improve sensitivity of the devices, regards to low concentration of gas vapor, for example, ranging from 1000 ppm to less than 10 ppm? How stable are these chemical sensors under different humid conditions and for long-term storage? How does miniaturization can affect detection limit factor in the sense of improving structure of device from micro to nano level? How to improve sensing signals and optimize limiting factors in order to achieve the desired level of detection? When there are many parameters of a sensor that can be interfered, which will be the most optimal choice to effectively enhance the quality of sensing behaviors and cost-efficiency and worthwhile? While several of these questions have been answered for a selected series of gas sensors, systematic studies are still rare. The aim of the research described in this thesis is to partly fill this gap, largely address the above mentioned issues by focusing on three aspects: to study the principle of the detection of acetone molecule in gas phase by fluorinated monolayers in field effect transistors system as well as non-conductive polymer in a chemocapacitive platform; to determine the interference of nanostructure (monolayers and nanocomposite with nanoparticles embedded in polymer network) in sensing layers of the devices in relation to the enhancement of analyte's adsorption into these layers; and finally, to evaluate and optimize sensing properties of both micro IDEs and nanogap IDEs, with the aim to sense acetone at a low concentration. Fortunately, these goals have come within reach.

## **5. Outline of this Thesis**

In this thesis, the development of different gas sensors for acetone detection at low concentration will be presented and discussed with two approaches: acetone gas sensor as a functionalized SiNW-FET and acetone gas sensor as a chemocapacitor using micro and nano IDEs structure.

In Chapter 2 the development of SiNWs FETs devices and their sensing performance toward VOCs at ppm level are described, whereas Chapter 3 and 4 deal with the detection of acetone by micro and nanogap IDEs devices used nanocomposite as sensing material. Chapter 5 discussed the optimization of the nanogap IDEs in comparison with micro IDEs with respect to improving the detection limit of the sensors.

Acetone at ppm level has to be selectively detected amongst more than two hundred kinds of other VOCs in the exhaled breath. Aiming for a portable device, in **Chapter 2**, we investigated the development of acetone sensors with acetone trapping alkyne based Self Assembled Monolayers (SAMs) provides on a silicon nanowire field-effect transistor (SiNW-FET). Surface characteristics of the nanostructured-functionalized layer will be studied by Auger system (AES), Scanning Electronic Microscopy (SEM) and Atomic Force Microscopy (AFM). Nuclear Magnetic Resonance (NMR) and X-rays Photoelectron Spectroscopy (XPS) are used to assess properties of the surface modified organic monolayers. Preliminary sensing behaviors of SiNW-FET were performed towards octanone at 500 ppb. Key desired parameters for gas analysing sensors such as selectivity, sensibility, stability and response/recovery time were evaluated. The observed results were further discussed regards to sensing acetone within same regime.

In **Chapter 3**, we focused on the use of a novel nanocomposite as sensing material for acetone using a micro-IDEs structure based on chemocapacitive sensing. The nanocomposite layer contained functionalized silicon nanoparticles incorporated in a polymer network: poly (4- vinyl phenol) (PVPH). PVPH is sensitive to acetone because of its high physisorption. Sensing performance of the device as a chemocapacitor at room temperature were pursued and they were tested with acetone and other different analytes, for example, acetonitrile and heptane to understand the sensing mechanism of acetone of the whole system. Stability and durability of the devices were also examined in this study.

To improve the sensitivity of acetone sensor using chemocapacitor structure, in **Chapter 4**, we pursue nanotechnology approaches by designing and creating a new structure of IDEs with nano gaps (50 to 250 nm) using conventional micro-fabrication process. A thin layer of polymer (PVPH) was then filled in between the nano gaps of the



IDEs and this could enhance the sensitivity of the device. The nanogap IDEs structure is particularly of interests for the development of high-performance acetone sensors for the application of medical diagnosis in Diabetes for its ability in detecting acetone at sub-ppm level.

To reach the optimal sensing behavior of acetone sensors using nanogap-IDEs, in **Chapter 5**, we investigated sensing performance of nanogap IDEs in comparison with micro IDEs. We discussed the improvement of signal-to-noise ratio of the acetone responses when using nanogap IDEs. The response towards acetone of nanogap IDEs was compared with micro IDEs as presented in the previous chapter in different conditions: when using same material (PVPH) and when the percentage of change remained equal, 0.2 % at 1000 ppm acetone. Furthermore, to study the reliability of these devices as chemocapacitors and the effect of surrounding ambient environment onto gas sensors, we extended our measurements with nanogap sensors in different humidity levels at room temperature and how humidity could interfere the detection limit of the sensors.

**Chapter 6** summarizes the most important achievements and places them in a wider context. Moreover, we address the potential of using of FET, micro-IDEs and nanogap-IDEs devices towards acetone and other VOCs at low concentrations in industry and medical diagnosis.

## References

- [1] P.N. Cheremisinoff, *Air Pollution Control and Design for Industry*, NewYork: M.Dekker, 1993.
- [2] Honeywell, *Flammable Gas Hazards*, Honeywell Gasb. (2013) 18–19.
- [3] B. Zhang, W. Fu, H. Li, X. Fu, Y. Wang, H. Bala, X. Wang, G. Sun, J. Cao, Z. Zhang, Synthesis and enhanced gas sensing properties of flower-like ZnO nanorods decorated with discrete CuO nanoparticles, *Mater. Lett.* 176 (2016) 13–16.
- [4] T. Li, W. Zeng, H. Long, Z. Wang, Nanosheet-assembled hierarchical SnO<sub>2</sub> nanostructures for efficient gas-sensing applications, *Sensors Actuators B Chem.* 231 (2016) 120–128.
- [5] A.L. Zou, Y. Qiu, J.J. Yu, B. Yin, G.Y. Cao, H.Q. Zhang, L.Z. Hu, Ethanol sensing with Au-modified ZnO microwires, *Sensors Actuators B Chem.* 227 (2016) 65–72.
- [6] G. Korotcenkov, *Introduction BT - Handbook of Gas Sensor Materials: Properties, Advantages and Shortcomings for Applications Volume 1: Conventional Approaches*, in: G. Korotcenkov (Ed.), Springer New York, New York, NY, 2013: pp. 1–45.
- [7] S. Wang, P. Wang, Z. Li, C. Xiao, B. Xiao, R. Zhao, T. Yang, M. Zhang, Facile fabrication and enhanced gas sensing properties of In<sub>2</sub>O<sub>3</sub> nanoparticles, *New J. Chem.* 38 (2014) 4879–4884.
- [8] K. Muthukrishnan, M. Vanaraja, S. Boomadevi, R.K. Karn, V. Singh, P.K. Singh, K. Pandiyan, Studies on acetone sensing characteristics of ZnO thin film prepared by sol–gel dip coating, *J. Alloys Compd.* 673 (2016) 138–143.
- [9] F.S. Dias, L.G. Tartuci, H. de F. Gorgulho, W.S. Machado, Characterization of a carbon xerogel-based sensor for detection of acetone, ethanol, and methanol vapors, *Sensors Actuators B Chem.* 231 (2016) 440–449.
- [10] M.K. Nakhleh, H. Amal, R. Jeries, Y.Y. Broza, M. Aboud, A. Gharra, H. Ivgi, S. Khatib, S. Badarneh, L. Har-Shai, L. Glass-Marmor, I. Lejbkiewicz, A. Miller, S. Badarny, R. Winer, J. Finberg, S. Cohen-Kaminsky, F. Perros, D. Montani, B. Girerd, G. Garcia, G. Simonneau, F. Nakhoul, S. Baram, R. Salim, M. Hakim, M. Gruber, O. Ronen, T. Marshak, I. Doweck, O. Nativ, Z. Bahouth, D. Shi, W. Zhang, Q. Hua, Y. Pan, L. Tao, H. Liu, A. Karban, E. Koifman, T. Rainis, R. Skapars, A. Sivins, G. Ancans, I. Liepniece-Karele, I. Kikuste, I. Lasina, I. Tolmanis, D. Johnson, S.Z. Millstone, J. Fulton, J.W. Wells, L.H. Wilf, M. Humbert, M. Leja, N. Peled, H. Haick, *Diagnosis and Classification of 17 Diseases from 1404 Subjects via Pattern Analysis of Exhaled Molecules*, *ACS Nano.* 11 (2017) 112–125.
- [11] P.I. Gouma, Nanostructured polymorphic oxides for advanced chemosensors, *Rev. Adv. Mater. Sci.* 5 (2003) 147–154.
- [12] M. Phillips, J. Greenberg, Ion-trap detection of volatile organic compounds in alveolar breath, *Clin. Chem.* 38 (1992) 60–65.
- [13] J. Kong, N.R. Franklin, C. Zhou, M.G. Chapline, S. Peng, K. Cho, H. Dai, Nanotube Molecular Wires as Chemical Sensors, *Science* (80-. ). 287 (2000) 622 LP-625.
- [14] J.D. Holmes, K.P. Johnston, R.C. Doty, B.A. Korgel, Control of Thickness and Orientation of Solution-Grown Silicon Nanowires, *Science* (80-. ). 287 (2000) 1471 LP-1473.
- [15] W. Cao, Y. Duan, *Breath Analysis: Potential for Clinical Diagnosis and Exposure Assessment*,

- Clin. Chem. 52 (2006) 800 LP-811. <http://clinchem.aaccjnls.org/content/52/5/800.abstract>.
- [16] B. Buszewski, M. Kęsy, T. Ligor, A. Amann, Human exhaled air analytics: biomarkers of diseases, *Biomed. Chromatogr.* 21 (2007) 553–566.
- [17] M.K. Nakhleh, Y.Y. Broza, H. Haick, Monolayer-capped gold nanoparticles for disease detection from breath, *Nanomedicine*. 9 (2014) 1991–2002.
- [18] W. Miekisch, J.K. Schubert, G.F.E. Noeldge-Schomburg, Diagnostic potential of breath analysis—focus on volatile organic compounds, *Clin. Chim. Acta.* 347 (2004) 25–39.
- [19] G.E. Umpierrez, M. DiGirolamo, J.A. Tuvlin, S.D. Isaacs, S.M. Bhoola, J.P. Kokko, Differences in metabolic and hormonal milieu in diabetic- and alcohol-induced ketoacidosis, *J. Crit. Care.* 15 (2000) 52–59.
- [20] C. Deng, J. Zhang, X. Yu, W. Zhang, X. Zhang, Determination of acetone in human breath by gas chromatography–mass spectrometry and solid-phase microextraction with on-fiber derivatization, *J. Chromatogr. B.* 810 (2004) 269–275.
- [21] M.J. Henderson, B.A. Karge, G.A. Wrenshall, Acetone in the Breath: A Study of Acetone Exhalation in Diabetic and Nondiabetic Human Subjects, *Diabetes*. 1 (1952) 188 LP-193.
- [22] B.J. Novak, D.R. Blake, S. Meinardi, F.S. Rowland, A. Pontello, D.M. Cooper, P.R. Galassetti, Exhaled methyl nitrate as a noninvasive marker of hyperglycemia in type 1 diabetes, *Proc. Natl. Acad. Sci.* 104 (2007) 15613–15618.
- [23] J.M. Sanchez, R.D. Sacks, GC Analysis of Human Breath with A Series-Coupled Column Ensemble and A Multibed Sorption Trap, *Anal. Chem.* 75 (2003) 2231–2236.
- [24] H. Lord, Y. Yu, A. Segal, J. Pawliszyn, Breath Analysis and Monitoring by Membrane Extraction with Sorbent Interface, *Anal. Chem.* 74 (2002) 5650–5657.
- [25] P. Dwivedi, P. Wu, S.J. Klopsch, G.J. Puzon, L. Xun, H.H. Hill, Metabolic profiling by ion mobility mass spectrometry (IMMS), *Metabolomics*. 4 (2008) 63–80.
- [26] W.-H. Cheng, W.-J. Lee, Technology development in breath microanalysis for clinical diagnosis, *J. Lab. Clin. Med.* 133 (1999) 218–228.
- [27] D. Smith, P. Španěl, Selected ion flow tube mass spectrometry (SIFT-MS) for on-line trace gas analysis, *Mass Spectrom. Rev.* 24 (2005) 661–700.
- [28] P. Španěl, D. Smith, Selected ion flow tube: a technique for quantitative trace gas analysis of air and breath, *Med. Biol. Eng. Comput.* 34 (1996) 409–419.
- [29] K. Toda, J. Li, P.K. Dasgupta, Measurement of ammonia in human breath with a liquid-film conductivity sensor, *Anal. Chem.* 78 (2006) 7284–7291.
- [30] A. Hansel, T.D. Märk, Foreword, *Int. J. Mass Spectrom.* 239 (2004) vii–viii.
- [31] C. Warneke, J.A. de Gouw, W.C. Kuster, P.D. Goldan, R. Fall, Validation of Atmospheric VOC Measurements by Proton-Transfer- Reaction Mass Spectrometry Using a Gas-Chromatographic Preseparation Method, *Environ. Sci. Technol.* 37 (2003) 2494–2501.
- [32] C.E. Davis, M. Frank, B. Mizaikoff, H. Oser, Editorial the future of sensors and instrumentation for human breath analysis, *IEEE Sens. J.* 10 (2010) 3–6.

- [33] O.K. Tan, W. Cao, W. Zhu, J.W. Chai, J.S. Pan, Ethanol sensors based on nano-sized  $\alpha$ -Fe<sub>2</sub>O<sub>3</sub> with SnO<sub>2</sub>, ZrO<sub>2</sub>, TiO<sub>2</sub> solid solutions, *Sensors Actuators, B Chem.* 93 (2003) 396–401.
- [34] J. Zhao, L.-H. Huo, S. Gao, H. Zhao, J.-G. Zhao, Alcohols and acetone sensing properties of SnO<sub>2</sub> thin films deposited by dip-coating, *Sensors Actuators, B Chem.* 115 (2006) 460–464.
- [35] M. Blo, M.C. Carotta, S. Galliera, S. Gherardi, A. Giberti, V. Guidi, C. Malagù, G. Martinelli, M. Sacerdoti, B. Vendemiati, A. Zanni, Synthesis of pure and loaded powders of WO<sub>3</sub> for NO<sub>2</sub> detection through thick film technology, *Sensors Actuators, B Chem.* 103 (2004) 213–218.
- [36] R. Ionescu, A. Hoel, C.G. Granqvist, E. Llobet, P. Heszler, Low-level detection of ethanol and H<sub>2</sub>S with temperature- modulated WO<sub>3</sub> nanoparticle gas sensors, *Sensors Actuators, B Chem.* 104 (2005) 132–139.
- [37] B.L. Zhu, C.S. Xie, W.Y. Wang, K.J. Huang, J.H. Hu, Improvement in gas sensitivity of ZnO thick film to volatile organic compounds (VOCs) by adding TiO<sub>2</sub>, *Mater. Lett.* 58 (2004) 624–629.
- [38] X.L. Cheng, H. Zhao, L.H. Huo, S. Gao, J.G. Zhao, ZnO nanoparticulate thin film: Preparation, characterization and gas-sensing property, *Sensors Actuators, B Chem.* 102 (2004) 248–252.
- [39] D. Zhang, A. Liu, H. Chang, B. Xia, Room-temperature high-performance acetone gas sensor based on hydrothermal synthesized SnO<sub>2</sub>-reduced graphene oxide hybrid composite, *RSC Adv.* 5 (2015) 3016–3022.
- [40] X. Xu, Y. Chen, G. Zhang, S. Ma, Y. Lu, H. Bian, Q. Chen, Highly sensitive VOCs-acetone sensor based on Ag-decorated SnO<sub>2</sub> hollow nanofibers, *J. Alloys Compd.* 703 (2017) 572–579.
- [41] M. Yin, L. Yu, S. Liu, Synthesis of thickness-controlled cuboid WO<sub>3</sub> nanosheets and their exposed facets-dependent acetone sensing properties, *J. Alloys Compd.* 696 (2017) 490–497.
- [42] G.-J. Sun, H. Kheel, S. Park, S. Lee, S. Eon Park, C. Lee, Synthesis of TiO<sub>2</sub> nanorods decorated with NiO nanoparticles and their acetone sensing properties, *Ceram. Int.* 42 (2016) 1063–1069.
- [43] R. Jaisutti, M. Lee, J. Kim, S. Choi, T.-J. Ha, J. Kim, H. Kim, S.K. Park, Y.-H. Kim, Ultrasensitive Room-Temperature Operable Gas Sensors Using p-Type Na:ZnO Nanoflowers for Diabetes Detection, *ACS Appl. Mater. Interfaces.* 9 (2017) 8796–8804.
- [44] S. Liang, J. Li, F. Wang, J. Qin, X. Lai, X. Jiang, Highly sensitive acetone gas sensor based on ultrafine  $\alpha$ -Fe<sub>2</sub>O<sub>3</sub> nanoparticles, *Sensors Actuators B Chem.* 238 (2017) 923–927.
- [45] X. Zhou, J. Liu, C. Wang, P. Sun, X. Hu, X. Li, K. Shimano, N. Yamazoe, G. Lu, Highly sensitive acetone gas sensor based on porous ZnFe<sub>2</sub>O<sub>4</sub> nanospheres, *Sensors Actuators B Chem.* 206 (2015) 577–583.
- [46] C. Wang, J. Liu, Q. Yang, P. Sun, Y. Gao, F. Liu, J. Zheng, G. Lu, Ultrasensitive and low detection limit of acetone gas sensor based on W-doped NiO hierarchical nanostructure, *Sensors Actuators B Chem.* 220 (2015) 59–67.
- [47] A. Reungchaiwat, T. Wongchanapiboon, S. Liawruangrath, S. Phanichphant, Home-made Detection Device for a Mixture of Ethanol and Acetone, *Sensors (Basel).* 7 (2007) 202–213.
- [48] W.-Y. Chung, G. Sakai, K. Shimano, N. Miura, D.-D. Lee, N. Yamazoe, Preparation of indium oxide thin film by spin-coating method and its gas-sensing properties, *Sensors Actuators B Chem.* 46 (1998) 139–145.

- [49] J. Shieh, H.M. Feng, M.H. Hon, H.Y. Juang, WO<sub>3</sub> and W<sub>0.5</sub>Ti<sub>0.5</sub>O thin-film gas sensors prepared by sol-gel dip-coating, *Sensors Actuators B Chem.* 86 (2002) 75–80.
- [50] J. Janata, M. Josowicz, Conducting polymers in electronic chemical sensors, *Nat Mater.* 2 (2003) 19–24.
- [51] L.C.P.M. de Smet, D. Ullien, M. Mescher, E.J.R. Sudhölter, Organic Surface Modification of Silicon Nanowire-Based Sensor Devices, in: A.B.T.-N.-I. and A. Hashim (Ed.), *InTech*, Rijeka, 2011: p. Ch. 13.
- [52] M.E.S.T.S.U.O.M.O.E.O.M.A.D.M.H.A.M.C.O.M. Ebru Akoglu, *Measurement Instrumentation Sensors*, 2007.
- [53] P. Gründler, Conductivity Sensors and Capacitive Sensors, in: *Chem. Sensors An Introd. Sci. Eng.*, Springer Berlin Heidelberg, Berlin, Heidelberg, 2007: pp. 123–132.
- [54] I. Bilican, M.T. Guler, N. Gulener, M. Yuksel, S. Agan, Capacitive solvent sensing with interdigitated microelectrodes, *Microsyst. Technol.* 22 (2016) 659–668.
- [55] Y. Lai, E. V Bordatchev, S.K. Nikumb, Metallic micro displacement capacitive sensor fabricated by laser micromachining technology, *Microsyst. Technol.* 12 (2006) 778.
- [56] N.J.R. Muniraj, MEMS based humidity sensor using Si cantilever beam for harsh environmental conditions, *Microsyst. Technol.* 17 (2011) 27–29.
- [57] L.A. Rocha, R.A. Dias, E. Cretu, L. Mol, R.F. Wolffenbuttel, Auto-calibration of capacitive MEMS accelerometers based on pull-in voltage, *Microsyst. Technol.* 17 (2011) 429–436.
- [58] Y. He, J. Liu, L. Li, J. He, A novel capacitive pressure sensor and interface circuitry, *Microsyst. Technol.* 19 (2013) 25–30.
- [59] B.A. Ganji, M.S. Nateri, A high sensitive MEMS capacitive fingerprint sensor using slotted membrane, *Microsyst. Technol.* 19 (2013) 121–129.
- [60] T.P. Vello, R.F. de Oliveira, G.O. Silva, D.H.S. de Camargo, C.C.B. Bufon, A simple capacitive method to evaluate ethanol fuel samples, *Sci. Rep.* 7 (2017) 43432.
- [61] B.S. Noremberg, R.M. Silva, O.G. Paniz, J.H. Alano, M.R.F. Gonçalves, S.I. Wolke, J. Labidi, A. Valentini, N.L. V Carreño, From banana stem to conductive paper: A capacitive electrode and gas sensor, *Sensors Actuators B Chem.* 240 (2017) 459–467.
- [62] A. Hazra, Capacitive modeling of TiO<sub>2</sub> nanotube based gas/vapor sensor devices, in: *2016 IEEE Nanotechnol. Mater. Devices Conf.*, 2016: pp. 1–2.
- [63] S. Homayoonnia, S. Zeinali, Design and fabrication of capacitive nanosensor based on MOF nanoparticles as sensing layer for VOCs detection, *Sensors Actuators B Chem.* 237 (2016) 776–786.
- [64] C. Sapsanis, H. Omran, V. Chernikova, O. Shekhah, Y. Belmabkhout, U. Buttner, M. Eddaoudi, K. Salama, Insights on Capacitive Interdigitated Electrodes Coated with MOF Thin Films: Humidity and VOCs Sensing as a Case Study, *Sensors.* 15 (2015) 18153.
- [65] M.E. Gimon-Kinsel, K.J. Balkus Jr, Pulsed laser deposition of mesoporous niobium oxide thin films and application as chemical sensors, *Microporous Mesoporous Mater.* 28 (1999) 113–123.
- [66] A. V Mamishev, K. Sundara-Rajan, F. Yang, Y. Du, M. Zahn, Interdigital sensors and

transducers, *Proc. IEEE.* 92 (2004) 808–845.

[67] M.R. Khan, S.-W. Kang, Highly Sensitive Multi-Channel IDC Sensor Array for Low Concentration Taste Detection, *Sensors.* 15 (2015) 13201.

[68] T.-H. Joubert, J. du Toit, B. Mkwakikunga, P. Bosscha, Handheld chemiresistive gas sensor readout system, in: 2017: p. 100360R–100360R–10.

[69] G. Niarchos, G. Dubourg, G. Afroudakis, M. Georgopoulos, V. Tsouti, E. Makarona, V. Crnojevic-Bengin, C. Tsamis, Humidity Sensing Properties of Paper Substrates and Their Passivation with ZnO Nanoparticles for Sensor Applications, *Sensors.* 17 (2017) 516.

[70] D. Berdat, A.C. Martin Rodriguez, F. Herrera, M.A.M. Gijs, Label-free detection of DNA with interdigitated micro-electrodes in a fluidic cell, *Lab Chip.* 8 (2008) 302–308.

[71] T. Tang, R.J. Sadleir, Quantification of Intraventricular Hemorrhage with Electrical Impedance Tomography Using a Spherical Model, *Physiol. Meas.* 32 (2011) 811–821.

[72] M. Varshney, Y. Li, Interdigitated array microelectrodes based impedance biosensors for detection of bacterial cells, *Biosens. Bioelectron.* 24 (2009) 2951–2960.

[73] C. Chun-Hung, T. Dah-Shyang, C. Wen-Hung, C. Yi-Deng, L. Kuei-Yi, H. Ying-Sheng, Miniature asymmetric ultracapacitor of patterned carbon nanotubes and hydrous ruthenium dioxide, *Nanotechnology.* 23 (2012) 485402.

[74] Q. Nguyen Minh, A. Kuijk, S.P. Pujari, F. van de Bent, J. Baggerman, H.D. Tong, H. Zuilhof, C.J.M. van Rijn, Preparation and gas sensing properties of nanocomposite polymers on micro-Interdigitated electrodes for detection of volatile organic compounds at room temperature, *Sensors Actuators B Chem.* 252 (2017) 1098–1104.

## Chapter 2



### Fluorinated alkyne-derived monolayers on oxide-free silicon nanowires via one-step hydrosilylation

#### **Abstract**

Passivation of oxide-free silicon nanowires (Si NWs) by the formation of high-quality fluorinated 1-hexadecyne-derived monolayers with varying fluorine content has been investigated. Alkyl chain monolayers ( $C_{16}H_{30-x}F_x$ ) with a varying number of fluorine substituents ( $x = 0, 1, 3, 9, 17$ ) were attached onto hydrogen-terminated silicon (Si-H) surfaces with an effective one-step hydrosilylation. This surface chemistry gives well-defined monolayers on nanowires that have a cylindrical core-shell structure, as characterized by X-ray photoelectron spectroscopy (XPS), Fourier transform infrared spectroscopy (FT-IR) and static contact angle (SCA) analysis. The monolayers were stable under acidic and basic conditions, as well as under extreme conditions (such as UV exposure), and provide excellent surface passivation, which opens up applications in the fields of field effect transistors, optoelectronics and especially for disease diagnosis.

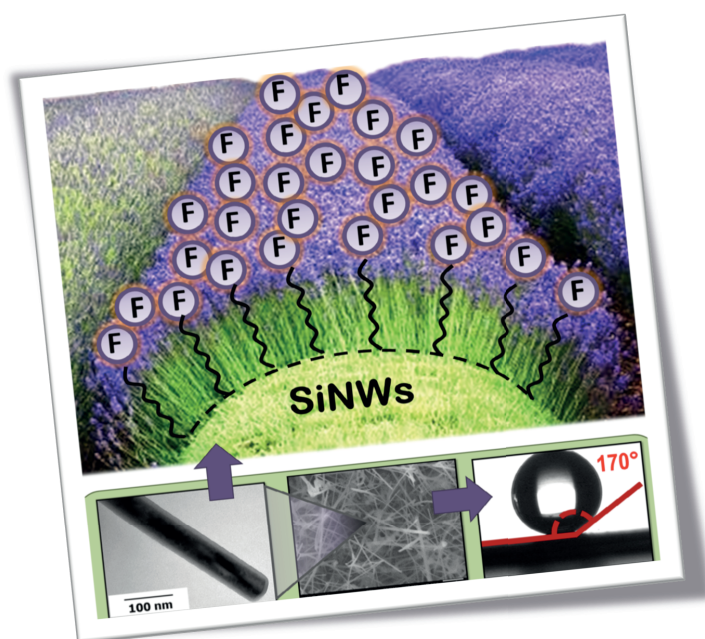
*This chapter has been published as:*

*"Fluorinated alkyne-derived monolayers on oxide-free silicon nanowires via one-step hydrosilylation", [Quyen Nguyen Minh](#), Sidharam P. Pujari, Bin Wang, Zhanhua Wang, Hossam Haick, Han Zuilhof, Cees J.M. van Rijn, Applied Surface Science, **2016**.*

**Keywords**

Silicon nanowires, surface modification, oxide-free silicon, fluorinated monolayers, hydrosilylation.

**Graphical Abstracts**





## 1. Introduction

Silicon (Si) has been exploited in many applications in the field of semiconductors, such as optoelectronic devices,[1, 2] molecular electronics[3] and bioelectronics.[4] Particularly, nanoelectronics with low-dimensional systems based on Silicon (Si) have been extensively researched, for instance (0D)-nanoparticles,[5] (1D)-nanowires[6] or (2D)-nanosheets.[7] Si NWs are of considerable interest and widely studied because of their good electrical conductivity properties for semiconducting devices.[8] Si NWs devices are now subject to numerous studies in diagnostics based on a selective and sensitive response to analytes using a functionalized FET channel.[9] One of the approaches is to create an active channel layer by the chemical adsorption of organic molecules via Si-O or Si-C bonds onto the Si surface, which passivates the surface of pure Si.[10-13] This strategy improves the surface properties of the NWs as well as enhances the electron transport in Si NWs based FETs.[14, 15] Since Si surface atoms are easily oxidized, as-prepared Si NWs, as well as other Si materials, are always coated with a native oxide layer. As a result, the device's performance is strongly diminished by charge scattering and trapping in the oxide layer of Si NWs.[16] Hydrogen fluoride etching can remove the oxide layer, and form a Si-H terminated surface. However, the Si H-terminated surface is unstable and prone to be oxidized again. To prevent this, the Si-H surface can be passivated by an organic monolayer to prevent oxidation.[17] The covalent binding of organic molecules onto the Si surface enhances device performance by minimizing the charge trapping sites and thereby increasing the carrier mobility.[18] Previous research has shown that the carrier mobility can be well controlled by the passivation of Si NWs surfaces via either Si-C or Si-O bonds.[18] In addition, several studies have concluded that the removal of the oxide layer before covalent Si-C or Si-O surface bond formation can increase the trans-conductance values[19] and enhances the performance of FETs with higher on-off ratio.[20]

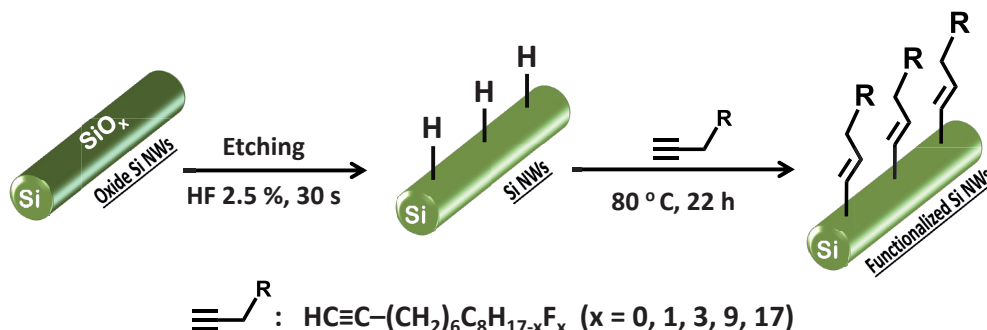
Silane chemistry, yielding Si-O linked monolayers, is widely used for the functionalization of Si surfaces.[21, 22] Nevertheless, there are some drawbacks and limitations of this chemistry, such as unstable monolayers which result in a decreased electrical sensitivity of devices. Also, other Si-C-linked monolayer-forming methods such as electrochemical functionalization,[23] and transition metal-catalyzed alkylation[24] are inadequate

35

techniques for stable[25] monolayer formation. Alternatively, Bashouti and co-workers applied a 2-step chlorination-alkylation method to Si NWs.[26] Although this approach leads to less surface oxidation and more densely packed monolayers, it required rather harsh preparation conditions. Finally, the attachment of 1-alkenes onto Si surfaces under UV light is another popular method for Si surface functionalization,[27, 28] which is much milder again, but also provides only an intermediate electrical passivation. Therefore, all these cases, either the surface stability and/or passivation is less than optimal or, the processes require hazardous chemicals and/or extreme reaction conditions which limits industrial applications.

Silicon surface modification using alkynes has been shown to be a highly efficient and mild method to form highly passivating organic monolayers with Si-C≡C bonds on a Si wafer surface.[29, 30] This method not only results in well-defined monolayers on Si surfaces with good packing density and high surface coverage, but provides stronger Si-C bonds as well.[30, 31] Therefore, it seemed to have high potential to apply this method to the surface functionalization of Si NWs. In addition, the mild reaction conditions allow for the introduction of a range of functional groups on the surface. In this regard, the use of fluorinated alkynes would provide an easily accessible additional tool, namely the stepwise variation of the work function of the underlying Si NWs surface.[32-34]

In this study, we investigated the formation of five different 1-hexadecyne-derived monolayers with a varying number of fluorine atoms ( $\text{HC}\equiv\text{C}-(\text{CH}_2)_6\text{C}_8\text{H}_{17-x}\text{F}_x$ ;  $x = 0, 1, 3, 9, 17$ ) onto oxide-free hydrogen-terminated Si NWs by a one-step hydrosilylation using 1-alkynes **F0** to **F17** (Scheme 1). These monolayers were characterized in detail by X-ray photoelectron spectroscopy (XPS), infrared spectroscopy (IR), static contact angle measurements, scanning electron microscopy (SEM) and transmission electron microscopy (TEM). The complete passivation of the oxide layer on the Si NWs was studied by UV-VIS measurements in the presence of Rhodamine B as an indicator. The stability of the monolayers on the Si NWs surfaces was evaluated under acidic (pH 3) and basic (pH 11) conditions for 1 week. Finally, preliminary data show their usefulness as components of electrically active sensing devices.



**Scheme 1.** Passivation of Si NWs by the formation of fluorinated hexadecyne-derived monolayers via a one-step hydrosilylation method.

## 2. Experimental methods and test procedure

Chemicals, synthesis of fluorinated monomer as well as detailed reaction schemes towards monolayers on oxide-free Si NWs are described in the Supporting Information in section 1, 2 and 3, respectively.

Compound **F17** (See *Supporting Information* section 3) was obtained via a four-step reaction starting from the coupling of a heptadecafluoro-1-iodooctane ( $\text{C}_8\text{F}_{17}\text{I}$ ) to a 5-hexene-1-ol. Reduction of the product heptadecafluoro-5-iodotetradecan-1-ol ( $\text{C}_8\text{F}_{17}\text{-CH}_2\text{-CHI-(CH}_2\text{)}_4\text{-OH}$ ) by  $\text{LiAlH}_4$ , followed by reaction with  $\text{HBr}$  then yields 14-bromoheptadecafluorotetradecane ( $\text{C}_8\text{F}_{17}\text{-(CH}_2\text{)}_6\text{-Br}$ ). This is reacted with  $\text{LiC}\equiv\text{CH}$  to finally provide 1-alkyne **F17** (99.98% purity), in a manner that is both more environmentally friendly and efficient than previous routes.[35]

### 2.1. Equipment - Surface Characterization Methods

**X-ray Photoelectron Spectroscopy (XPS).** Using a JPS-9200 Photoelectron Spectrometer (JOEL, Japan), monolayers on Si NWs were characterized under UHV conditions with monochromatic  $\text{Al K}\alpha$  X-ray radiation at 12 kV and 20 mA, analyzer pass energy of 10 eV, and an angle between sample and detector (takeoff angle  $\varphi$ ) of  $80^\circ$ .

Narrow-range (elemental) XPS spectra were corrected with a linear background before fitting. XPS data were analyzed by Casa XPS software (version 2.3.15). In all XPS spectra, the alkyl carbon (C-H) C 1s binding energy at 285.0 eV was used as a reference for spectrum calibration. All other carbon peaks were then fitted with an equal full width at half-maximum (FWHM) for each individual component.

**Static Contact Angle (SCA).** An automated contact angle Krüss DSA 100 goniometer was used to study the wetting of modified surfaces by water, ethylene glycol, dimethylformamide and hexadecane via measurements of the SCAs of the two sides of a drop (6  $\mu$ L) within 20 s after drop deposition. At least five droplets were dispensed, and the SCAs were then determined using the Tangent 1 fitting mode, with error of  $\pm 2^\circ$ .

**Scanning Electron Microscopy (SEM).** The morphology of Si NWs was observed by a high vacuum and partial vacuum ( $10 - 10^{-4}$  Pa) JSM 5600 LV (Japan) Scanning Electron Microscope at accelerating voltages of 10 kV.

**Transmission Electron Microscopy (TEM).** Samples were prepared by depositing a 6  $\mu$ L drop of Si NWs dispersed in ethanol (about 50  $\mu$ g/mL) onto a carbon-coated copper grid. The samples were observed with a JEOL JEM-1010 transmission electron microscope at an accelerating voltage of 80 kV. Pictures were taken with a SIS MegaView III digital camera (Soft Imaging Systems) and were analyzed by the AnalySISv. 2.0 software.

**Fourier Transform Infrared Spectroscopy (FT-IR).** To study the formation of monolayers on nanowires, we measured IR in transmission mode with a Bruker Tensor 27 spectrometer. Samples were sonicated in  $\text{CCl}_4$  to obtain nanowire suspensions without other carbon interference, followed by the addition of oven-dried KBr powder to the suspension. The mixtures were then dried in a vacuum oven ( $10^{-3}$  bar, 25  $^\circ\text{C}$ , 24 h) to remove remaining solvent, and packed into circular pallets of 1 cm diameter and 1 mm thick under 8000 psi pressure. The transmittance data of these pallets were collected and analyzed by OPUS software version 7.2, spectra from 4000 to 400  $\text{cm}^{-1}$  (resolution 2  $\text{cm}^{-1}$ , 500 scans).

**Ultraviolet Visible Spectroscopy (UV-VIS).** To examine the complete passivation of Si NWs by fluorinated alkyne monolayers, the **Si-H** NWs and modified Si NWs samples were tested in a solution of 5  $\mu\text{M}$  Rhodamine B (RhB) in EtOH as an indicator. The **Si-H** NWs; **F0**,

**F1, F3, F9** and **F17**-modified Si NWs (from same fabrication batch that leads to same density of NWs) were removed from their substrates by mild sonication (1 min in absolute EtOH), resulting in NWs suspensions. These suspensions were transferred to separate quartz cuvetts containing RhB (5  $\mu$ M in EtOH). All these samples were then exposed to UV light using a Camag UV lamp (254 nm, 8 W) at RT, for 1 and 24 h. The UV-VIS spectra of as-prepared samples and exposed samples were then measured with a Cary 50 scan Varian spectrometer with a Xenon lamp. The UV-VIS data of these samples were measured and compared to pure RhB in EtOH at the same concentration which has a typical peak at 550 nm.

## 2.2. Preparation of Fluorinated alkyne-derived monolayers onto Si-H NWs

After the etching process, the H-terminated Si NWs on the Si substrate (See *Supporting Information* section 2) were immediately added into a three-necked glass flask with flattened bottom containing the fluorinated alkyne ( $\text{HC}\equiv\text{C}-(\text{CH}_2)_6\text{C}_8\text{H}_{17-x}\text{F}_x$ ;  $x = 0, 1, 3, 9$  or  $17$ ) in an inert atmosphere glovebox (RT,  $\text{N}_2$  atmosphere with  $< 0.1\%$   $\text{O}_2$ ). The reactor was preliminarily purged at RT for 30 min using a  $\sim 10$  mbar vacuum at one side and continuous refilling with Ar via a thin capillary from the other side. The entire flask was placed in an 80  $^\circ\text{C}$  sand bath, and the reaction was allowed to proceed with no additional stirring for 22 h. Samples were then taken out of the reactor and washed extensively with dry hexane and dichloromethane, after which they were completely dried with a stream of argon (all in the glovebox). Subsequently, further characterization of these functionalized Si NWs was performed.

## 3. Results and Discussion

### Passivation of Si NWs

Si NWs were prepared on Si (111) surfaces by chemical vapor deposition of  $\text{B}_2\text{H}_6$  and  $\text{SiH}_4$ . This process typically resulted in Si NWs that were significantly contaminated with organics. The optimal cleaning procedure was obtained by first using organic solvents to briefly clean the samples and then immerse these samples in piranha for 10 min before

continuing with etching and surface modification steps (detail information can be found in Supporting Information).

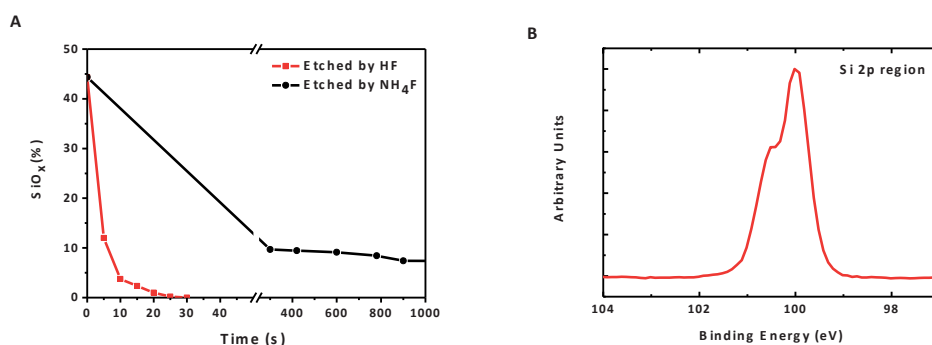
**Table 1.** XPS survey scan-based elemental composition (in %) of Si NWs before [a] and after [b] HF etching in comparison with those after modification.

Si NWs	C 1s 285.0 eV	O 1s 531.0 eV	F 1s 686.0 eV	Si 2p [% SiO <sub>x</sub> ] <sup>[c]</sup> 99.0 - 100.0 eV
Untreated <sup>[a]</sup>	8.9	44.4	0.4	25.8 [20.5]
10 min Piranha then 30 s HF (2.5 %) etching <sup>[b]</sup>	2.4	4.3	0.6	92.7 [< 0.1]
<b>F3</b>	40.85	6.62	9.09	43.43 [< 0.1]
<b>F17</b>	28.34	3.49	25.79	42.37 [< 0.1]

<sup>[a]</sup> Si NWs before etching, <sup>[b]</sup> Si NWs after etching. <sup>[c]</sup> The Si 2p signal from SiO<sub>x</sub> at 103.0 - 106.0 eV (in square brackets) was fitted and calculated from the total signal of Si 2p region from 90.0 - 109.0 eV.

Next, to obtain oxide-free, functionalized Si NWs via H-terminated Si NWs, etching is a crucial step. **Table 1** shows a XPS survey scan-derived element quantification of C, O, F and Si before and after etching (see Figure S1 for XPS wide scan). This etching was optimized, using 40 % NH<sub>4</sub>F and 2.5 % HF solutions. Typically, HF etches much more effectively than NH<sub>4</sub>F, as can be seen by comparing **Figure 1A**. After 15 min of NH<sub>4</sub>F etching under conditions that etch planar Si(111) effectively,<sup>[35, 36]</sup> on the Si NWs an oxide layer was detected of ~7 % of the total Si 2p signal, which does not diminish further upon doubling

the etching time (see Figure S2-A for XPS Si 2p data). In contrast, 30 s of HF etching works effectively, and yields a significant decrease in the  $\text{SiO}_x$  peak at 103.6 eV, from 20.5 % in the untreated sample to < 0.1 % after HF treatment (see Table 1, Figure 1B and Figure S3-A for XPS Si 2p narrow scan). The difference between the two etching procedures lies in the pH, and results in rather different surface compositions. Upon etching with HF (pH 1–2), stable  $\text{Si-H}_x$  species ( $x = 1-3$ ) were mostly found on the surface; on the other hand, etching with  $\text{NH}_4\text{F}$  (pH 12–14) resulted in a significant amount of  $\text{Si-(O-)}_x$  species ( $x = 1-3$ ). Even at high  $\text{NH}_4\text{F}$  concentration and prolonged processing, this Si oxide layer cannot be removed completely, because the Si surfaces were negatively charged and stabilized/passivated by electrostatically attracted  $\text{NH}_4^+$  ions.[37] Therefore, HF was subsequently used in our surface modification procedure of Si NWs.



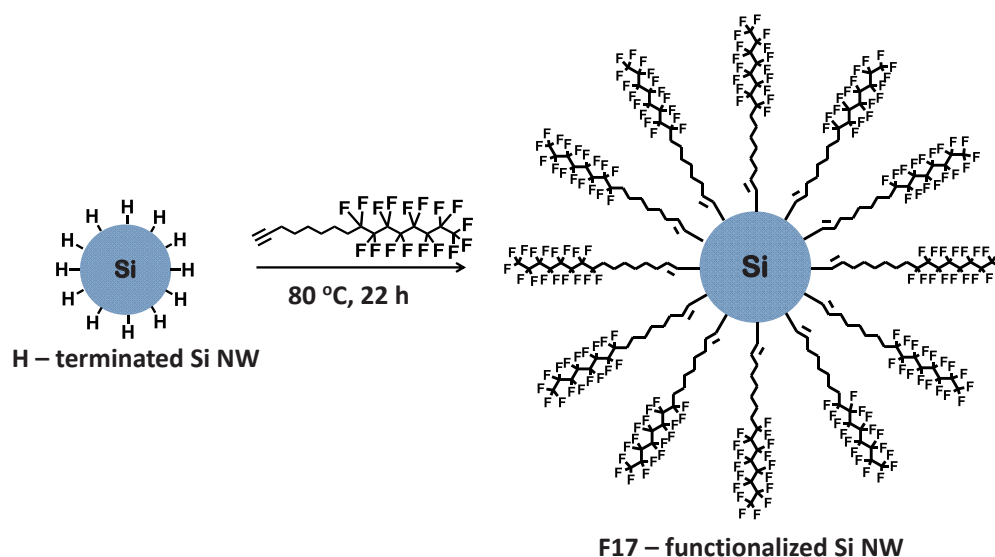
**Figure 1.** Decrease of native oxide  $\text{SiO}_x$  on Si NWs as a function of etching time. The percentage of the  $\text{SiO}_x$  peaks as a fraction of the entire Si content was determined by fitting the signals observed for  $\text{SiO}_x$  at 103.0 - 106.0 eV and Si 2p at 99.0 - 100.0 eV. (A) - Etchant: 40%  $\text{NH}_4\text{F}$  (in black) and 2.5% HF (in red); (B) - XPS Si 2p narrow scan of **Si-H** NWs surface after etching.

As observed in the XPS wide scan of Si NWs etched with HF for 30 s (Figure S3-C), a small amount of oxygen is still present (in all experiments, the oxygen content is < 5 %), possibly resulting from the physical adsorption of water vapor and other oxygen sources during the surface modification process.[38] Therefore, we considered a narrow spectrum of Si 2p region to confirm growth of the silicon oxide layer. Peaks at 103.6 eV were used to identify

the oxidation of Si at the outer surface of Si NWs. Generally, the absence of this peak was used as a proof that no Si–O bond was present on the Si surface (Figure 1B), and Si–H bond formation had been successful.

### Formation of Fluorinated Monolayers by One-step Hydrosilylation on Si NWs

We adapted a one-step modification procedure for grafting 1-alkyne fluoro-hydro monolayers on planar Si (111) surfaces[35] to the modification of the Si NWs under current study (see Scheme 2). After HF treatment, samples were immediately transferred into Schlenk tubes containing an alkyne (**F0**, **F1**, **F3**, **F9** or **F17**). Oxygen levels were minimized by purging with argon, and the reaction was allowed to proceed for 22 h at 80 °C under ambient light.

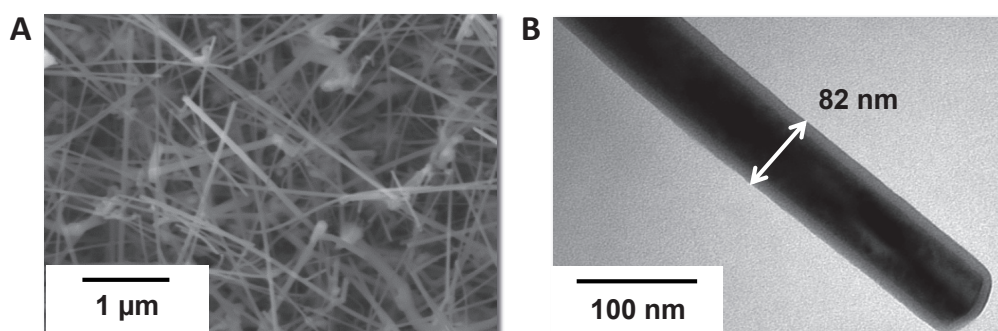


**Scheme 2.** One-step hydrosilylation of H-terminated Si NWs using fluorinated-C<sub>16</sub>-alkynes (cross-section configurations of individual NWs).



### Morphology of Molecule Modified Si NWs

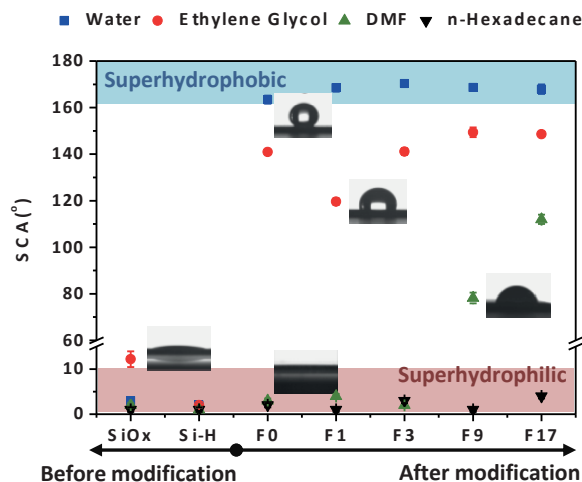
After the reaction, the modified Si NWs were cleaned, and analyzed for their morphology by SEM and TEM. SEM images showed that resulting Si NWs are well recognizable in the as-synthesized samples (**Figure 2A**). As shown in *Supporting Information* Figure S5 compared to Figure 2A, the morphological difference between the Si NWs before and after surface modification is insignificant on this scale. Corresponding TEM images show the diameter of a single wire to be 80-100 nm (**Figure 2B**).



**Figure 2.** Representative SEM image of Si NWs after modification with fluorinated alkyne-derived monolayers (**F17**) (A) (other SEM images in *Supporting Information* Figure S5), and TEM image of a single nanowire with a diameter of 82 nm (B).

### Wettability of Modified Si NWs

Static contact angle (SCA) measurements were used to determine the solvent repellence of surfaces containing monolayer-modified Si NWs. In this study, SCAs were measured for all monolayer-modified Si NWs and compared to as-fabricated  $\text{SiO}_x/\text{Si}$  NWs and **Si-H** NWs (etched in 2.5 % HF 30 s). To this aim SCA measurements were performed with solvents of different surface tension: n-hexadecane (27.5 mN/m), dimethylformamide (DMF; 37.1 mN/m), ethylene glycol (EG; 47.7 mN/m) and water (72.8 mN/m). Typical images of droplets on  $\text{SiO}_x$  NWs, **Si-H** NWs and various monolayer-modified Si NWs are shown together with the SCA results in **Figure 3**.



**Figure 3.** Static Contact Angle ( $\theta$ ) at 20 °C of Si NWs with native oxide, hydrogen-terminated, and **F0**-, **F1**-, **F3**-, **F9**-, **F17**- derived monolayers measured with water, EG, and DMF. For n-hexadecane, all samples had  $\theta < 10^\circ$ .

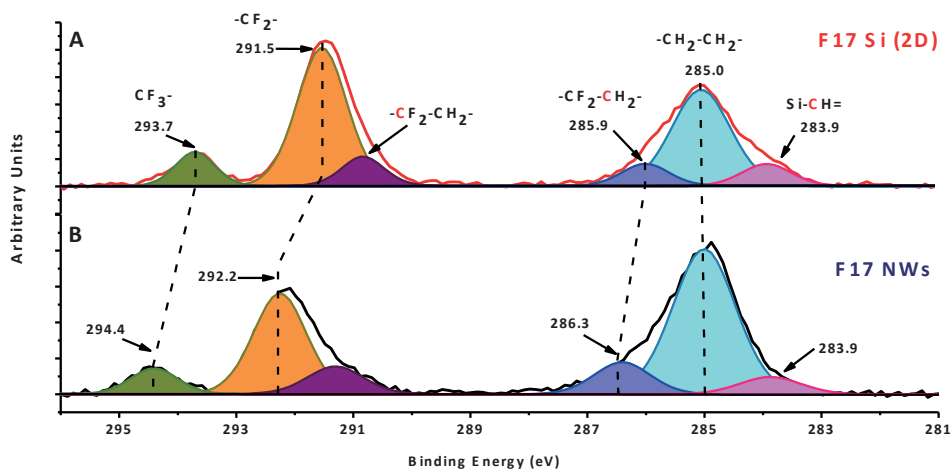
Surfaces covered with unmodified Si NWs (SiO<sub>x</sub>/Si NWs and **Si-H** NWs) demonstrated no solvent repellence, and immediately absorbed all four liquids. The SCAs of these unmodified samples were all below  $10^\circ$ . This superhydrophilic and superoleophilic behavior is caused by the structure of Si NWs on the substrate surface; Si NWs form a hierarchical surface structure with sub-micrometer gaps, yielding a “homogenous-rough surface” which allows rapid penetration of liquid into the Si NWs layer.[39] In contrast, all **F<sub>x</sub>**-modified Si NWs exhibited both superhydrophobic ( $> 163^\circ$  for water) and highly oleophilic ( $< 10^\circ$  for n-hexadecane) properties. Water drops roll off easily from these surfaces by tilting  $< 1^\circ$ , the rolling-off movements were captured in videos (see *Supporting Information* Video S1 for **F0** and S2 for **F17**) according to our previous work.[40] The hydrophobicity of monolayer-modified Si NWs (from **F1** to **F17**) is typical for the presence of fluorinated species.[41] As compared to the SCA of fluorinated monolayers on 2D surfaces, however, the SCA for surfaces covered with our modified Si NWs is significantly higher ( $> 165^\circ$  for Si NWs compared to  $125^\circ$  for 2D), which is caused by the increased roughness of the surface.[42] In addition to repelling water, the monolayer modified Si

NWs surfaces also showed repellence towards EG and DMF. For EG, a reduced SCA was observed for **F1** modified Si NWs compared to the other fluorinated Si NWs: 120° compared to 140°. This is caused by the larger dipole moment of the **F1** molecule (due to the presence of one single polar C–F bond), which makes the surface more polar than the other fluorinated molecules and even **F0**.<sup>[43]</sup> In addition, the work of adhesion ( $W_A$ ) of all monolayers with different test solvents were then calculated using equation S1 (see *Supporting Information* Section 6). However, **F1** monolayers tested with ethylene glycol gave the strongest  $W_A$  value of 24.1 mJ.m<sup>-2</sup>, in line with the dipole of the C–F bond and concomitantly higher interaction with polar groups in the liquid.<sup>[41, 44]</sup> Towards DMF the **F17** and **F9** monolayers yield the highest SCA values (112° and 78°, respectively), while **F0**, **F1** and **F3** monolayers show complete wetting (SCA < 10°). This is in agreement with a low energy hierarchical surface reported by Zhang et al.<sup>[45]</sup> Moreover, this effect is also caused by the competition between the hierarchical structure formed by the Si NWs that leads to complete wetting and the repellence caused by the fluorinated monolayer. For **F0**, **F1** and **F3** the effect of the structure prevails while for **F9** and **F17** the effect of monolayer is dominant over the structure effect (see *Supporting Information* Figure S6).

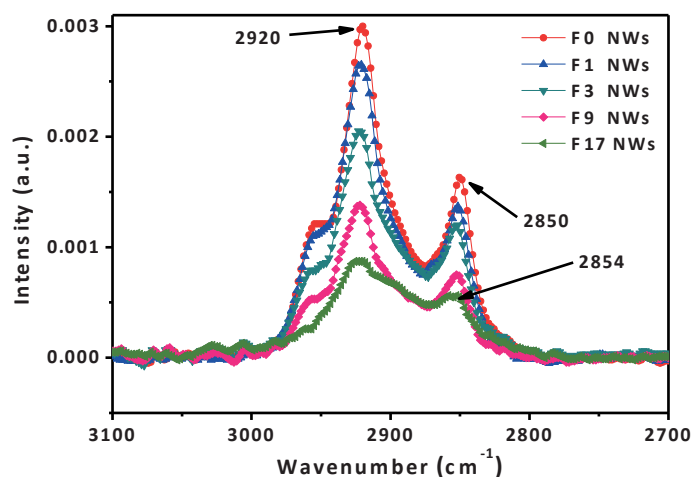
### Surface characterization of the Si NWs

The surface of the monolayer-modified Si NWs was characterized in detail using XPS and infrared spectroscopy. As a typical example, the XPS data obtained for the **F17** monolayer-modified Si NWs are discussed, and the C1s data are shown in **Figure 4** (see Figure S4 for the other fluorinated monolayers). The wide-range survey spectrum is in line with the proposed structure of **Scheme 2**. Notably, the Si 2p data, with the detection limit of our equipment (< 0.1%), do not show a SiO<sub>x</sub> oxide peak at 103.6 eV, and the only Si component present is assigned to pure Si at 99.0 eV. Some oxygen (2-3%) is still present in all cases, which we attribute to the physisorption of hydrocarbon impurities. This physisorption is likely enhanced by the ‘forest-like’ structure of the Si NWs on the wafer surface.<sup>[38]</sup> The **F17**-derived C1s spectrum exhibits six distinctive peaks (see Figure 4B), which are a near-complete overlay with the spectrum obtained for planar **F17** modified Si (111) surfaces<sup>[35]</sup> (see for a side-by-side comparison Figure 4). A peak which was assigned to Si–

$\text{CH}=\text{CH}-$  groups at 283.9 eV is observed beside the  $\text{CH}_2$  peak at 285.0 eV. The relative ratio of the intensity of these two peaks is roughly 7.1 : 1, in excellent agreement with that expected from the depicted molecular structure (7.0 : 1). The center-to-center difference between the C-Si peak and the  $-\text{CH}_2-\text{CH}_2-$  peak was 1.1 eV, as also observed in a previous study on Si NWs from Bashouti and co-workers.[46] Interestingly, we found that the center-to-center difference between the  $-\text{CF}_2-\text{CH}_2-$  and  $-\text{CH}_2-\text{CH}_2-$  peak was 1.3 eV, whereas for planar Si surfaces 0.9 eV was found. Also, the C-F peaks observed for Si NWs occur consistently at slightly higher values than observations for flat Si (111) surfaces. This holds not only for **F17**, but also for **F9** and **F3**, the energy difference ( $\Delta$ ) was about 0.3 – 0.7 eV (see Table S3 for C-H region of modified Si NWs with fluorinated alkyne derived monolayers; Table S3 and S4 for peak shifting assigned to  $\text{CF}_3$  signals and  $\text{CF}_2$  signals, respectively). This shift may be related to charging effects of adjacent fluorine atoms of Si NWs present in the ‘forest’ of Si NWs.



**Figure 4.** XPS C1s narrow scan of fluoro-alkyne-derived monolayers on Si NWs (**F17** NWs) as compared to fluoro-alkyne derived monolayers on a planar surface (**F17** Si 2D) showing peak shifts:  $\text{CF}_3-$  ( $\Delta\text{eV} = 0.7$ ),  $-\text{CF}_2-$  ( $\Delta\text{eV} = 0.7$ ) and  $-\text{CF}_2-\text{CH}_2-$  ( $\Delta\text{eV} = 0.4$ ).



**Figure 5.** Infrared spectra (C-H stretching region) of fluorinated alkyne-derived monolayers (**F0**, **F1**, **F3**, **F9**, **F17**) on Si NWs surfaces. KBr pallets were prepared from suspensions of modified Si NWs.

The quality of the fluorinated monolayers on the Si NWs was evaluated by infrared transmission-adsorption spectroscopy (**Figure 5**). Peaks of symmetric and anti-symmetric  $\text{CH}_2$  stretching vibrations were found around  $2920 - 2923 \text{ cm}^{-1}$  and  $2850 - 2854 \text{ cm}^{-1}$ , respectively, (see more details in Table S1). The absolute value of the wavenumber at which these peaks occurred shifted about  $3 \text{ cm}^{-1}$  from **F0** to **F17** for Si NWs, equal to observations for flat surfaces,[35, 44] which is caused by the presence of an increasing number of fluorine atoms. Furthermore, the peak around  $2920 \text{ cm}^{-1}$  becomes broader for **F0** going to **F17**. This is caused by the increasing electrostatic repellence of **F0** to **F17**, which leads to less ordering and less dense packing when more fluorine atoms are present. The intensity of this peak starts to decrease from **F0** to **F17** because a number of  $-\text{CH}_2-$  have been replaced by  $-\text{CF}_2-$  and  $-\text{CF}_3$ . In addition, this peak shifts  $\sim 3 \text{ cm}^{-1}$  towards lower wavenumber compared to corresponding flat **F17**-coated Si surfaces.[33] This suggests less short-range ordering of the alkyne chains, which can be attributed to the curvature of the Si NWs surface[47, 48] (more details in Figure S6). Figure 5 also shows the effects of methyl-containing contaminants, which decrease with further fluorination as expected. Finally, all

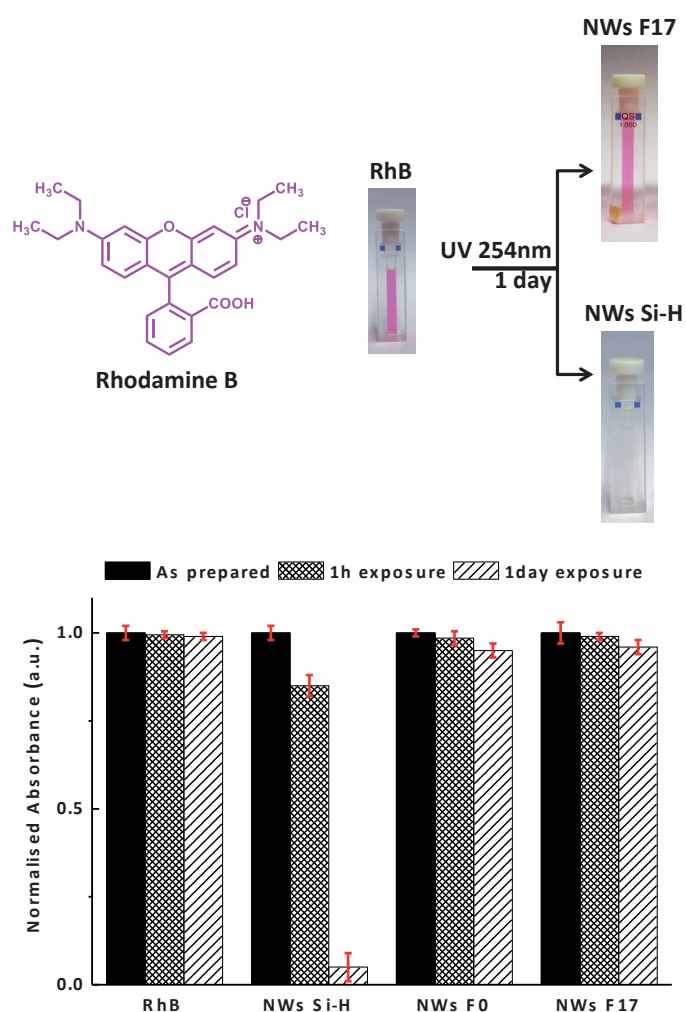
modified samples display clear peaks corresponding to the Si–C=C stretching vibrations at 1585 - 1615  $\text{cm}^{-1}$  (see *Supporting Information*, Figure S7), confirming the proper monolayer formation.

### Stability of fluorinated alkyne-derived monolayers

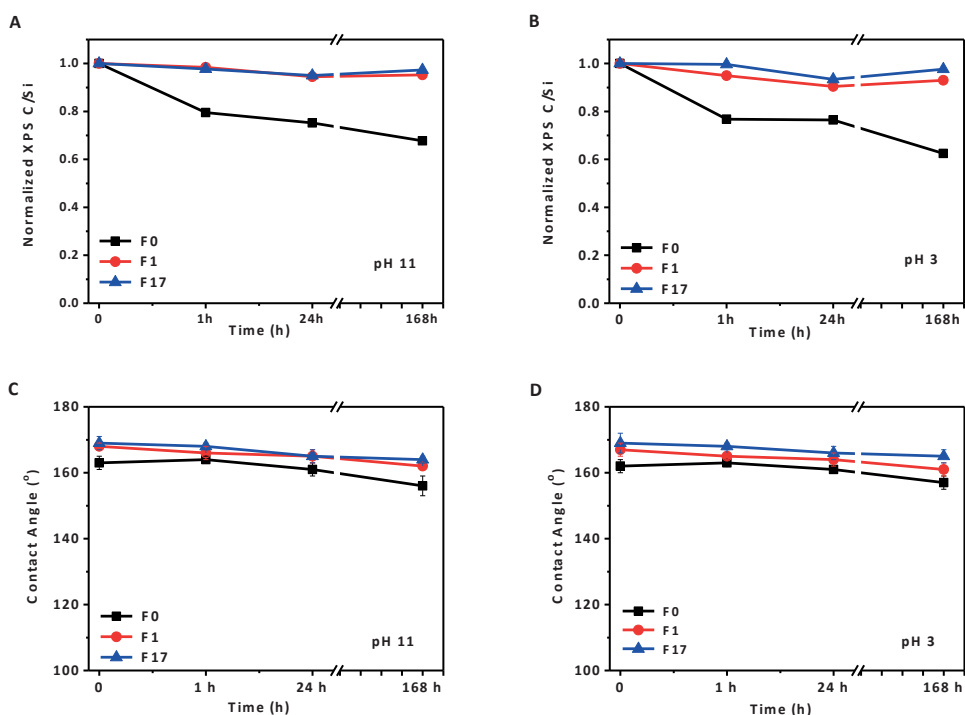
The potential use of monolayer-modified Si NWs critically depends on the stability. Therefore this stability was investigated under two different sorts of conditions: upon irradiation with UV light, and under acid and basic conditions. In order to assess the stability of the electrical passivation provided by these fluorinated monolayers on non-oxidized NWs, we investigated the photo electrochemical degradation of rhodamine B (RhB) by UV-irradiated (254 nm, with the lamp-to-samples distance of 1 cm) Si NWs. Here we use the observation that uncoated, including H-terminated, Si NWs display a significant photocatalytic activity: upon irradiation of uncoated Si NWs in water,  $\text{OH}^\bullet$  radicals are formed. These oxidize RhB, yielding the transformation of the colored RhB solutions into colorless ones, a process easily followed by UV-VIS spectroscopy.[49, 50] Therefore, the stability of RhB solution in irradiated Si NWs is a good indicator of the overall surface passivation, since coated Si NWs prevent water to come close to the nanowire, and do accordingly not easily produce  $\text{OH}^\bullet$  radicals.

**Figure 6** summarizes the degradation of RhB versus time by normalized absorbance of Rhodamine B solutions (5  $\mu\text{M}$ , without Si NWs, and in the presence of **Si-H**, **F0**, **F17** Si NWs (more detailed timelines, data in Figure S8). Directly after preparation, all samples showed a similar absorbance at 550 nm. Upon exposure to UV, the absorbance of the RhB solution stayed constant. However, upon addition of Si-H Si NWs, complete discoloration of RhB occurs after 24 h of UV irradiation. In contrast, almost no degradation was detected in the presence of all **F<sub>x</sub>** modified Si NWs, even after prolonging the irradiation time to 24 h. Apparently, coating with a densely packed  $\text{C}_{16}$  monolayer will nearly fully block the photocatalytic activity, independent of the degree of fluorination. It is known that the hydrosilylation by 1-alkynes will retain a fraction of the Si-H sites at the Si surface.[30] Therefore it can be concluded that the packing is so dense that these remaining Si-H sites atoms on the **F0** and **F17** Si NWs surfaces are effectively shielded from the participation in

the degradation of RhB, proving long-term photoelectrical passivation, even upon UV (254 nm) irradiation.



**Figure 6.** Normalized UV-VIS absorbance data at 500 nm for F0, F17 and Si-H NWs in 5  $\mu$ M RhB solution. Absorbance is shown directly after preparation, and after 1 and 24 h of irradiation at 254 nm.



**Figure 7.** Normalized data of C/Si ratio from XPS survey scans studied at pH 11 (A) and pH 3 (B), followed by static water contact angle measurements pH 11 (C) and pH 11 (D) of **F0** (black square), **F1** (red circle), and **F17** (blue triangle) monolayers on Si NWs surfaces after taking samples out from basic and acidic conditions after the indicated time period.

To determine the hydrolytic stability, the prepared **F<sub>x</sub>**-modified Si NWs were immersed up to 1 week in acidic (HCl, pH 3) and basic (NaOH, pH 11) media under agitation,[25] and subsequently cleaned with excess of deionized water and CH<sub>2</sub>Cl<sub>2</sub>. The stability of the samples was evaluated by SCA and XPS. As representatives, the results for **F0**, **F1** and **F17** derived monolayers are shown in **Figure 7**. In general, there is no significant change in SCA after 1h and 24 h of basic or acidic treatment compared to freshly made monolayers. Only upon immersion for 7 days, the SCA was slightly reduced (about 6°), although still maintaining a high monolayer quality and yielding for both **F1** and **F17** still SCA > 160°. In



line with this, the XPS data showed that the C content of the **F1** and **F17** modified Si NWs remained almost constant, while for **F0**-modified Si NWs, the C content decreased notably in both acidic and basic conditions. These results showed that fluorinated alkyne monolayers on Si NWs are outstandingly stable, and continue to be superhydrophobic even under prolonged acidic and basic conditions.

Finally to provide proof-of-concept of the usefulness of thus modified Si NWs for volatolomics studies,[51] we prepared FETs based on the surface-modified Si NWs for their sensing of volatile organic compounds (VOCs). As one representative example, a typical  $I_{ds}$ - $V_g$  plot of a FET device that uses **F9** Si NWs as conducting channel is shown in supporting information **Figure S9A**. The **F9** Si NWs FET shows p-type transport behavior of the **F9** Si NWs FET with  $I_{on}$  = 16  $\mu$ A, which is defined as  $I_{ds}$  value at  $V_g$  = -40 V, analogous to that of related silane-based Si NWs FET devices.[10] A gas response of the **F9**-Si NWs FETs to a lung cancer-related VOC (2-octanone) shown in supporting information **Figure S9B**. Using a gate voltage  $V_g$  = -25 V, this device presented a clear  $I_{ds}$  values versus time response upon exposure to 500 ppb 2-octanone [reference: dry  $N_2$ ]. The adsorption of the ketone to the monolayer thus apparently leads to easily discernable changes in the work function of the Si NWs. Although preliminary, this result shows the potential of the **F<sub>x</sub>** Si NWs FETs to detect analytes at low concentrations (ppb), which implies an improvement over analogous devices based on silane chemistry. In combination with their high stability, this opens up the use of such monolayer-modified Si NWs for a much wider range of sensing and optoelectronic studies, which are currently ongoing within our laboratories.

#### 4. Conclusions

Silicon nanowires (Si NWs) can be effectively functionalized using hydrosilylation of 1-alkynes to yield highly uniform fluorinated alkyne-derived Si-C=C linked monolayers on all facets of the persistently oxide-free NW. The obtained monolayers on Si NWs display superhydrophobic behavior, and a high stability under both acidic and basic conditions for a week, and also under prolonged UV (254 nm) irradiation. The monolayer coating provides excellent electrical passivation, and – as shown in preliminary experiments – display significant potential in the use of single-channel FETs, e.g. for the detection of volatile organic compounds.

## References

- [1] J.A. Duffie, W.A. Beckman, *Solar Engineering of Thermal Processes: Fourth Edition*, 2013.
- [2] F. Pacheco-Torgal, M.V. Diamanti, A. Nazari, C.G. Granqvist, *Nanotechnology in eco-efficient construction: Materials, processes and applications*, 2013.
- [3] D.O. Demchenko, P.D. Heinz, B. Lee, Determining factors of thermoelectric properties of semiconductor nanowires, *Nanoscale Res. Lett.*, 6 (2011) 1-6.
- [4] T. Adam, U. Hashim, Highly sensitive silicon nanowire biosensor with novel liquid gate control for detection of specific single-stranded DNA molecules, *Biosensors and Bioelectronics*, 67 (2015) 656-661.
- [5] I.H. Son, J.H. Park, S. Kwon, S. Park, M.H. Rummeli, A. Bachmatiuk, H.J. Song, J. Ku, J.W. Choi, J.M. Choi, S.G. Doo, H. Chang, Silicon carbide-free graphene growth on silicon for lithium-ion battery with high volumetric energy density, *Nat. Commun.*, 6 (2015) 7393.
- [6] M.O. Noor, U.J. Krull, Silicon nanowires as field-effect transducers for biosensor development: A review, *Analytica Chimica Acta*, 825 (2014) 1-25.
- [7] H. Okamoto, Y. Kumai, Y. Sugiyama, T. Mitsuoka, K. Nakanishi, T. Ohta, H. Nozaki, S. Yamaguchi, S. Shirai, H. Nakano, Silicon Nanosheets and Their Self-Assembled Regular Stacking Structure, *Journal of the American Chemical Society*, 132 (2010) 2710-2718.
- [8] E. Garnett, P. Yang, Light Trapping in Silicon Nanowire Solar Cells, *Nano Letters*, 10 (2010) 1082-1087.
- [9] H. Haick, Y.Y. Broza, P. Mochalski, V. Ruzsanyi, A. Amann, Assessment, origin, and implementation of breath volatile cancer markers, *Chemical Society Reviews*, 43 (2014) 1423-1449.
- [10] R. Ermanok, O. Assad, K. Zigelboim, B. Wang, H. Haick, Discriminative power of chemically sensitive silicon nanowire field effect transistors to volatile organic compounds, *ACS applied materials & interfaces*, 5 (2013) 11172-11183.
- [11] A. Bayn, X. Feng, K. Mullen, H. Haick, Field effect transistors based on polycyclic aromatic hydrocarbons for the detection and classification of volatile organic compounds, *ACS applied materials & interfaces*, 5 (2013) 3431-3440.
- [12] Y. Paska, T. Stelzner, S. Christiansen, H. Haick, Enhanced Sensing of Nonpolar Volatile Organic Compounds by Silicon Nanowire Field Effect Transistors, *ACS Nano*, 5 (2011) 5620-5626.
- [13] B. Wang, H. Haick, Effect of chain length on the sensing of volatile organic compounds by means of silicon nanowires, *ACS applied materials & interfaces*, 5 (2013) 5748-5756.
- [14] Y. Qu, L. Liao, Y. Li, H. Zhang, Y. Huang, X. Duan, Electrically Conductive and Optically Active Porous Silicon Nanowires, *Nano Letters*, 9 (2009) 4539-4543.
- [15] W. Lu, C.M. Lieber, Nanoelectronics from the bottom up, 6 (2007) 841-850.
- [16] P. Yu, C.-Y. Tsai, J.-K. Chang, C.-C. Lai, P.-H. Chen, Y.-C. Lai, P.-T. Tsai, M.-C. Li, H.-T. Pan, Y.-Y. Huang, C.-I. Wu, Y.-L. Chueh, S.-W. Chen, C.-H. Du, S.-F. Horng, H.-F. Meng, 13% Efficiency Hybrid

Organic/Silicon-Nanowire Heterojunction Solar Cell via Interface Engineering, ACS Nano, 7 (2013) 10780-10787.

[17] W.J.I. DeBenedetti, Y.J. Chabal, Functionalization of oxide-free silicon surfaces, J. Vac. Sci. Technol., A, 31 (2013) 050826.

[18] H. Haick, P.T. Hurley, A.I. Hochbaum, P. Yang, N.S. Lewis, Electrical Characteristics and Chemical Stability of Non-Oxidized, Methyl-Terminated Silicon Nanowires, Journal of the American Chemical Society, 128 (2006) 8990-8991.

[19] R. Boukherroub, S. Morin, P. Sharpe, D.D.M. Wayner, P. Allongue, Insights into the Formation Mechanisms of Si-OR Monolayers from the Thermal Reactions of Alcohols and Aldehydes with Si(111)-H<sub>1</sub>, Langmuir, 16 (2000) 7429-7434.

[20] R. Haight, L. Sekaric, A. Afzali, D. Newns, Controlling the Electronic Properties of Silicon Nanowires with Functional Molecular Groups, Nano Letters, 9 (2009) 3165-3170.

[21] W. Xu, S.S.S. Vegunta, J.C. Flake, Surface-modified silicon nanowire anodes for lithium-ion batteries, Journal of Power Sources, 196 (2011) 8583-8589.

[22] R. Ermanok, O. Assad, K. Zigelboim, B. Wang, H. Haick, Discriminative Power of Chemically Sensitive Silicon Nanowire Field Effect Transistors to Volatile Organic Compounds, ACS Applied Materials & Interfaces, 5 (2013) 11172-11183.

[23] R.L. Cicero, C.E.D. Chidsey, G.P. Lopinski, D.D.M. Wayner, R.A. Wolkow, Olefin Additions on H-Si(111): Evidence for a Surface Chain Reaction Initiated at Isolated Dangling Bonds, Langmuir, 18 (2002) 305-307.

[24] A. Saghatelian, J. Buriak, V.S.Y. Lin, M. Reza Ghadiri, Transition metal mediated surface modification of porous silicon, Tetrahedron, 57 (2001) 5131-5136.

[25] N.S. Bhairamadgi, S.P. Pujari, F.G. Trovela, A. Debrassi, A.A. Khamis, J.M. Alonso, A.A. Al Zahrani, T. Wennekes, H.A. Al-Turaif, C. van Rijn, Y.A. Alhamed, H. Zuilhof, Hydrolytic and Thermal Stability of Organic Monolayers on Various Inorganic Substrates, Langmuir, 30 (2014) 5829-5839.

[26] M.Y. Bashouti, T. Stelzner, S. Christiansen, H. Haick, Covalent Attachment of Alkyl Functionality to 50 nm Silicon Nanowires through a Chlorination/Alkylation Process, J. Phys. Chem. C, 113 (2009) 14823-14828.

[27] J.M. Buriak, Illuminating Silicon Surface Hydrosilylation: An Unexpected Plurality of Mechanisms, Chemistry of Materials, 26 (2014) 763-772.

[28] M.V. Lee, R. Scipioni, M. Boero, P.L. Silvestrelli, K. Ariga, The initiation mechanisms for surface hydrosilylation with 1-alkenes, Phys. Chem. Chem. Phys., 13 (2011) 4862-4867.

[29] O. Yaffe, L. Scheres, L. Segev, A. Biller, I. Ron, E. Salomon, M. Giesbers, A. Kahn, L. Kronik, H. Zuilhof, A. Vilan, D. Cahen, Hg/Molecular Monolayer-Si Junctions: Electrical Interplay between Monolayer Properties and Semiconductor Doping Density, J. Phys. Chem. C, 114 (2010) 10270-10279.

[30] H. Shpaisman, O. Seitz, O. Yaffe, K. Roodenko, L. Scheres, H. Zuilhof, Y.J. Chabal, T. Sueyoshi, S. Kera, N. Ueno, A. Vilan, D. Cahen, Structure Matters: Correlating temperature dependent electrical transport through alkyl monolayers with vibrational and photoelectron spectroscopies, Chem. Sci., 3 (2012) 851-862.

- [31] B. Rijkse, S.P. Pujari, L. Scheres, C.J.M. van Rijn, J.E. Baio, T. Weidner, H. Zuilhof, Hexadecadienyl Monolayers on Hydrogen-Terminated Si(111): Faster Monolayer Formation and Improved Surface Coverage Using the Enyne Moiety, *Langmuir*, 28 (2012) 6577-6588.
- [32] T. Toledano, A. Biller, T. Bendikov, H. Cohen, A. Vilan, D. Cahen, Controlling Space Charge of Oxide-Free Si by in Situ Modification of Dipolar Alkyl Monolayers, *J. Phys. Chem. C*, 116 (2012) 11434-11443.
- [33] D.M. Alloway, A.L. Graham, X. Yang, A. Mudalige, R. Colorado, V.H. Wysocki, J.E. Pemberton, T. Randall Lee, R.J. Wysocki, N.R. Armstrong, Tuning the Effective Work Function of Gold and Silver Using  $\omega$ -Functionalized Alkanethiols: Varying Surface Composition through Dilution and Choice of Terminal Groups, *J. Phys. Chem. C*, 113 (2009) 20328-20334.
- [34] O. Yaffe, Y. Qi, L. Scheres, S.R. Puniredd, L. Segev, T. Ely, H. Haick, H. Zuilhof, A. Vilan, L. Kronik, A. Kahn, D. Cahen, Charge transport across metal/molecular (alkyl) monolayer-Si junctions is dominated by the LUMO level, *Phys. Rev. B: Condens. Matter*, 85 (2012) 045433.
- [35] S.P. Pujari, E. Spruijt, M.A. Cohen Stuart, C.J.M. van Rijn, J.M.J. Paulusse, H. Zuilhof, Ultralow Adhesion and Friction of Fluoro-Hydro Alkyne-Derived Self-Assembled Monolayers on H-Terminated Si(111), *Langmuir*, 28 (2012) 17690-17700.
- [36] L. Scheres, A. Arafat, H. Zuilhof, Self-Assembly of High-Quality Covalently Bound Organic Monolayers onto Silicon, *Langmuir*, 23 (2007) 8343-8346.
- [37] W.W. Chen, X.H. Sun, S.D. Wang, S.T. Lee, B.K. Teo, Etching Behavior of Silicon Nanowires with HF and NH<sub>4</sub>F and Surface Characterization by Attenuated Total Reflection Fourier Transform Infrared Spectroscopy: Similarities and Differences between One-Dimensional and Two-Dimensional Silicon Surfaces, *J. Phys. Chem. B*, 109 (2005) 10871-10879.
- [38] L.J. Webb, D.J. Michalak, J.S. Biteen, B.S. Brunschwig, A.S.Y. Chan, D.W. Knapp, H.M. Meyer, E.J. Nemanick, M.C. Traub, N.S. Lewis, High-Resolution Soft X-ray Photoelectron Spectroscopic Studies and Scanning Auger Microscopy Studies of the Air Oxidation of Alkylated Silicon(111) Surfaces, *J. Phys. Chem. B*, 110 (2006) 23450-23459.
- [39] I. Liascukienė, M. Steffenhagen, S.J. Asadauskas, J.-F. Lambert, J. Landoulsi, Self-Assembly of Fatty Acids on Hydroxylated Al Surface and Effects of Their Stability on Wettability and Nanoscale Organization, *Langmuir*, 30 (2014) 5797-5807.
- [40] K. Ellinas, S.P. Pujari, D.A. Dragatogiannis, C.A. Charitidis, A. Tserepi, H. Zuilhof, E. Gogolides, Plasma Micro-Nanotextured, Scratch, Water and Hexadecane Resistant, Superhydrophobic, and Superamphiphobic Polymeric Surfaces with Perfluorinated Monolayers, *ACS applied materials & interfaces*, 6 (2014) 6510-6524.
- [41] R. Colorado, T.R. Lee, Wettabilities of Self-Assembled Monolayers on Gold Generated from Progressively Fluorinated Alkanethiols, *Langmuir*, 19 (2003) 3288-3296.
- [42] A. Lafuma, D. Quere, Superhydrophobic states, *Nat. Mater.*, 2 (2003) 457-460.
- [43] Z. Wang, S.P. Pujari, B. van Lagen, M.M.J. Smulders, H. Zuilhof, Highly Polymer-Repellent yet Atomically Flat Surfaces Based on Organic Monolayers with a Single Fluorine Atom, *Adv. Mater. Interfaces*, (2016) doi: 10.1002/admi.201500514.

- [44] S. Zhang, A.C. Jamison, D.K. Schwartz, T.R. Lee, Self-Assembled Monolayers Derived from a Double-Chained Monothiol Having Chemically Dissimilar Chains, *Langmuir*, 24 (2008) 10204-10208.
- [45] P. Zhang, S. Wang, S. Wang, L. Jiang, Superwetting Surfaces under Different Media: Effects of Surface Topography on Wettability, *Small*, 11 (2015) 1939-1946.
- [46] M.Y. Bashouti, T. Stelzner, A. Berger, S. Christiansen, H. Haick, Chemical Passivation of Silicon Nanowires with C1-C6 Alkyl Chains through Covalent Si-C Bonds, *J. Phys. Chem. C*, 112 (2008) 19168-19172.
- [47] R.L. Jones, N.C. Pearsall, J.D. Batteas, Disorder in Alkylsilane Monolayers Assembled on Surfaces with Nanoscopic Curvature, *J. Phys. Chem. C*, 113 (2009) 4507-4514.
- [48] M.J. Hostetler, J.J. Stokes, R.W. Murray, Infrared Spectroscopy of Three-Dimensional Self-Assembled Monolayers: N-Alkanethiolate Monolayers on Gold Cluster Compounds, *Langmuir*, 12 (1996) 3604-3612.
- [49] M. Shao, L. Cheng, X. Zhang, D.D.D. Ma, S.-t. Lee, Excellent Photocatalysis of HF-Treated Silicon Nanowires, *Journal of the American Chemical Society*, 131 (2009) 17738-17739.
- [50] N. Megouda, Y. Cofininier, S. Szunerits, T. Hadjersi, O. Elkechai, R. Boukherroub, Photocatalytic activity of silicon nanowires under UV and visible light irradiation, *Chemical communications*, 47 (2011) 991-993.
- [51] G. Konvalina, H. Haick, Sensors for Breath Testing: From Nanomaterials to Comprehensive Disease Detection, *Acc. Chem. Res.*, 47 (2014) 66-76.

## Chapter 3



### Preparation and Gas Sensing Properties of Nanocomposite Polymers on Micro-Interdigitated Electrodes for Detection of Volatile Organic Compounds at Room Temperature

#### **Abstract**

A room-temperature chemocapacitive gas sensor based on polymeric nanocomposites (NC), consisting of amine-terminated silicon nanoparticles (Si NPs-NH<sub>2</sub>) and poly (4-vinyl phenol), was fabricated on a micro-gap interdigitated electrode (M-IDE) and used for the detection of acetone. Several polymers were explored to capture acetone, of which poly (4-vinyl phenol) showed best results. The response of the sensor was significantly improved by the addition of silicon nanoparticles to the polymer layer. The response characteristics of the NC film towards volatile organic compounds (VOCs) were determined and compared with the pristine polymeric layer in this study. It was shown that the polymeric NC layer could detect acetone at room temperature within one minute. The sensing response towards acetone at room temperature proved that the turn-on and -off exposure to this analyte was reversible with good reproducibility (5 % decay) after multiple cycles of gas exposure. The proof-of-concept results are promising for the development of novel gas detectors that are applicable in many fields such as industrial and laboratorial security.

*This chapter has been published as:*

*"Preparation and Gas Sensing Properties of Nanocomposite Polymers on Micro-Interdigitated Electrodes for Detection of Volatile Organic Compounds at Room Temperature", [Quyen Nguyen Minh](#), Anke Kuijk, Sidharam P. Pujari, Franc van der Bent, Hien D. Tong, Han Zuilhof, and Cees J.M. van Rijn. Sensors and Actuators B: Chemical, Elsevier, **2017**.*

### Abbreviations

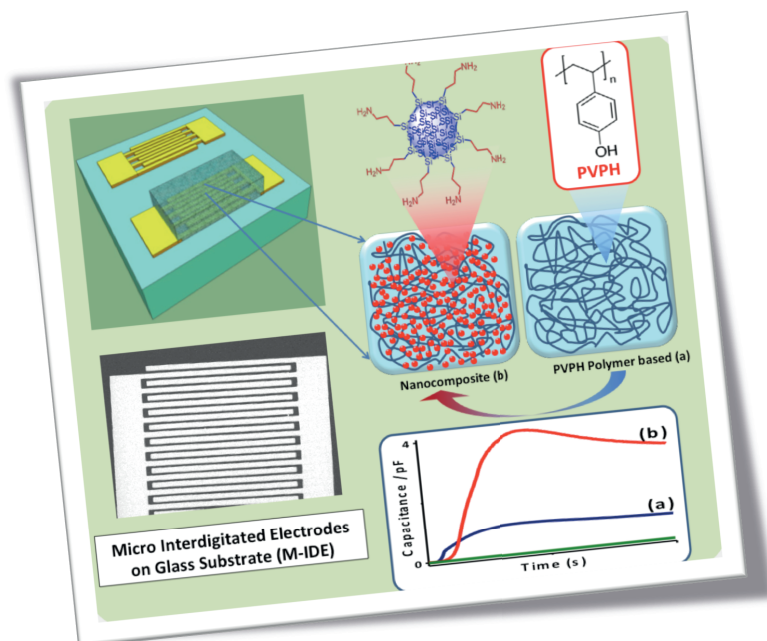
General: VOCs, volatile organic compounds; M-IDE, micro-gap interdigitated electrodes; Si NPs, silicon nanoparticles; NC, nanocomposite.

Polymers: PS, polystyrene; PVDF, poly vinylidene fluoride; PMMA, poly (methyl methacrylate); PECH, poly epichlorohydrin; PVPH, poly (4-vinylphenol).

### Keywords

Micro Interdigitated Electrodes, VOCs, Gas sensor, Nanocomposite, Chemocapacitor, Acetone, Poly (4-vinyl phenol).

### Graphical Abstracts





## 1. Introduction

Detection of volatile organic compounds (VOCs) is essential in both laboratories and industrial applications such as air quality monitoring, controlled-industrial processing, human safety, etc.[1-4] Chemical sensors for VOCs are therefore widely developed in many varieties, all with the same purpose of use, namely to detect an analyte at any required concentration. For instance, spectrometry and spectroscopy-based gas sensing techniques are able to provide most accurate (down to ppb or ppt levels) and selective measurements.[5-7] However, their disadvantages are obvious: the required equipment is typically bulky and quite expensive. In addition, most of the measurements and/or subsequent data analyses are time-consuming. Smaller, more easily applicable sensors include metal oxide-based chemiresistors [8, 9] and quartz crystal microbalance sensors.[10, 11] These have also shown good sensitivity/selectivity characteristics including competitiveness in fabrication costs, yet have their own drawbacks. The metal oxide-based sensors, for example, generally require external heating elements and suffer from poor stability and long recovery times. Field effect transistors, especially with organic sensing layers, remain unstable in the presence of water vapor, as well as when exposed to oxygen, and additionally, they are costly and have a complicated fabrication process.[12, 13] With a simple design, chemocapacitors are well known for their applications in humidity sensing,[14, 15] and also have been widely used for the quantitative detection of organic solvent molecules in the gas phase.[16-18] Moreover, chemocapacitors can be cost-effectively manufactured at a high production yield. It also combines good long-term stability and reproducibility with small chances of defects or damage.[19] In general, a typical chemocapacitor consists of two interdigitated planar electrodes that are covered with a dielectric sensing layer. Analytes are detected by this structure because they change the permittivity and thickness of the chemical sensing layer, both of which change the capacitance of the device. In most cases, polymers are used as sensing materials for VOCs detection because they provide an excellent linearity of the sensor signal as a result of the physical sorption of the gas molecules. Additionally, polymer films are known for their long-term stability and offer a good compromise between response time, selectivity and reversibility. The low selectivity of polymers is an issue, often solved by using an array of

sensors, which use different polymer layers to identify vapors. Among various polymers that have been exploited as active layers for VOCs detection on gas sensors, a nanocomposite with well-embedded nanoparticles in a polymer network has been shown to significantly enhance the sensing performance of the device.[20, 21]

Acetone is one of the most common VOCs, is hazardous and may therefore easily damage the human body i.e. eyes, nose, and nervous system when the concentration exceeds 170 ppm.[3] In order to modulate acetone levels with respect to human safety in (a) air indoor environment monitoring; (b) storage place of synthetic products (paints, wax and fuels) and acetone industrial process; or (c) laboratories and chemical industries etc., we aim to detect acetone vapour by an advanced chemocapacitor.

In this paper, we developed an schematically simple chemocapacitor that circumvents these disadvantages and that detects VOCs, acetone in particular, in a sensitive and rapid configuration at room temperature. Here, we present preliminary studies of acetone adsorption on micro-gap interdigitated electrodes (M-IDEs) coated with different polymers that are sensitive towards acetone vapor according to previous work [22, 23] (i.e. PS, PVDF, PVDF-PMMA, PMMA, PECH, PVPH, NIPAM, P2VP). Emphasis is on the development of these sensors based on nanocomposite (NC) materials of poly (4-vinyl phenol) (PVPH) and amino-terminated silicon ( $\text{Si}(\text{NH}_2)_x$ ) nanoparticles. And lastly, based on a combination of sensor response studies, we provide an indication of the potential of such devices as active components in robust, sensitive, portable and low power gas sensors.

## 2. Material and Methods

### 2.0. Chemicals

Polystyrene (PS), poly (methyl methacrylate) (PMMA), polyepichlorohydrin (PECH), poly (4-vinylphenol) (PVPH), poly (N-isopropylacrylamide) (NIPAM); poly (2-vinylpyridine) (P2VP), absolute ethanol (98 %), acetone (99.8 %), (3-aminopropyl)trimethoxysilane (97%) and sodium citrate tribasic dihydrate (99%) were purchased from Sigma Aldrich. Poly vinylidene fluoride (PVDF) was obtained from Alfa Aesar. All reagents were used as received.

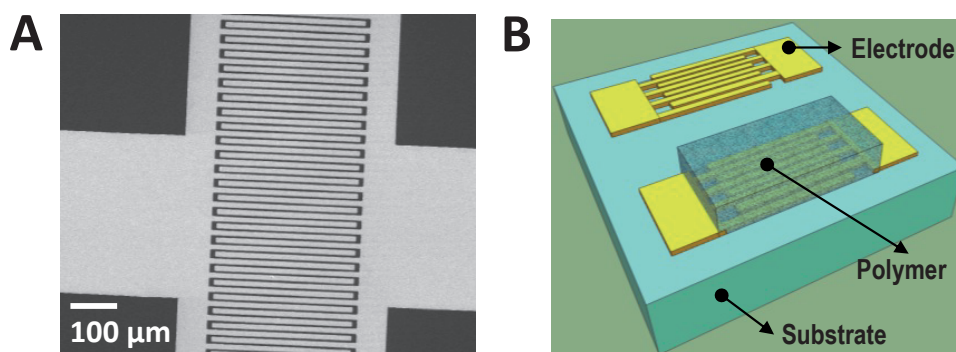
### 2.1. Synthesis of amino-functionalized silicon nanoparticles (Si NPs) in water

The Si NP precursor solution was prepared by adding 50 mL of (3-aminopropyl)trimethoxysilane to 200 mL N<sub>2</sub>-saturated aqueous solution dispersed with 9.3 g of sodium citrate tribasic dihydrate (see supporting information Scheme 1),[24] and the mixture was stirred for 10 min. The resultant precursor solution was transferred into a transparent glass vessel with a volume of 30 mL. The Si NPs (2 - 5 nm in diameter by DLS and TEM; maximum emission at 460 nm; see supporting information Scheme S2) were prepared by a microwave-assisted reaction at 160 °C for 15 min. After that, the Si NP sample was removed and cooled down to < 30 °C. It is worthwhile pointing out that, compared to the weak luminescence of the precursor solution, the resultant Si NPs sample displayed an intense blue-coloured fluorescence under UV irradiation.

### 2.2. Fabrication of micro gap interdigitated electrode (M-IDE) chemocapacitors

The micro-gap interdigitated electrodes (M-IDE) were fabricated by the vapour deposition of 110 - 120 nm gold onto a (electrically insulating) boron glass substrate. A conventional comb structure with 124 fingers was designed and fabricated on this substrate, with an electrode finger length of 300 µm, a finger width of 10 µm and a gap

width of 6  $\mu\text{m}$  (see **Figure 1A**). This design allows the formation of a homogenous polymeric active layer onto the IDE as schematically depicted in **Figure 1B**.



**Figure 1.** A SEM image of M-IDE (A) and 3D schematic drawing of the IDE with an ideally coated polymeric active layer (B).

### 2.3. Preparation and characterization of polymer layers and nanocomposite (PVPH Si NPs) active layers on M-IDE sensors

In brief, all polymers (PS, PVDF, PVDF-PMMA, PMMA, PECH, PVPH) were dissolved in sufficient solvent (see **Table 1**) with a weight concentration (wt.) of 10 % by sonication and/or stirring for more than 16 h until clear polymer solutions were collected. Solutions of PVPH were prepared in concentrations of 10, 20, and 30 wt.% to study the effect of layer thickness on sensitivity. For the nanocomposite active layer (PVPH-Si NPs), synthesized Si NPs were completely dispersed in polymer solution by means of sonication at room temperature for about 20 min. The mixture was then stirred for 16 h. The NP content was varied to yield solutions of 0.1 wt. %, 1 wt. %, 5 wt. %, 10 wt. % and 20 wt. % Si NPs. For gas-sensing measurements, M-IDEs were cleaned by rinsing with ethanol and acetone. Subsequently, a 6  $\mu\text{L}$  drop of the polymer solution was dropped on the M-IDE followed by spin coating at 500 rpm for 1 min to form a thin layer. After that, the sample was annealed at 60  $^{\circ}\text{C}$  for at least 30 min.

Scanning electron microscopy (JEOL, SEM 5600-LV, Japan) was used to observe the surface morphology of the sensing layer. In the energy-filtered transmission electron microscopy (JEOL JEM 2200-FS, Japan), zero-loss electrons were used for the energy-filtered micrographs with a slit width of 20 eV. Elemental analysis was done in HAADF mode with a step-size of 1 nm on an Oxford Instruments EDS analyser. The chemical bonding states were analyzed by using X-ray photo spectroscopy (XPS, JPS 9200, JEOL, Japan). Fourier transform infrared spectroscopy (FT-IR, model Tensor 27, Bruker, USA) was also used for the analysis of chemical bonds in NC active layers.

#### **2.4. Sampling setup**

A dedicated gas sensor characterization setup was designed to carry out electrical measurements in controlled environment with the sample mounted on a probe holder placed inside a designed 4 mL flow chamber (Figure S7). Nitrogen ( $N_2$ , > 98 % dry) was used as carrier gas while acetone was used as sensing analyte by bubbling the nitrogen carrier gas through acetone. The humidity was kept throughout the experiment, approximately 8 – 10 %. The mixed airflow was regulated with a mass flow controller from Bronkhorst®, The Netherlands to create an analyte/ $N_2$  flow of 400 mls/min during the sensing experiments. This leads to a concentration of 23 % acetone in  $N_2$ , as was calculated using vapour pressure. The flow chamber was equipped with a humidity sensor - HIH-4602-A (0-100% RH, TO-5, HONEYWELL S&C) to measure the relative humidity (accuracy  $\pm 1$  %RH) and temperature (accuracy  $\pm 0.2$  °C).

#### **2.5. Gas sensing measurements**

Real-time capacitance of the sensor upon exposure to acetone at room temperature was consequently recorded with an HP 4192A LF impedance analyser (Hewlett Packard, USA). The time-dependent capacitance change was measured at a fixed frequency of 30 kHz, which choice was based on a good and stable signal-to-noise ratio (see supporting information, Figure S11). The input voltage was 1 V. All capacitance measurements of

polymer films were performed at room temperature (24 °C). The measurement parameters and the data acquisition and storage were controlled with LabView™ 2011 software version 11.0. All reported capacitance graphs show the increase in capacitance with respect to the capacitance measured in a pure nitrogen environment.

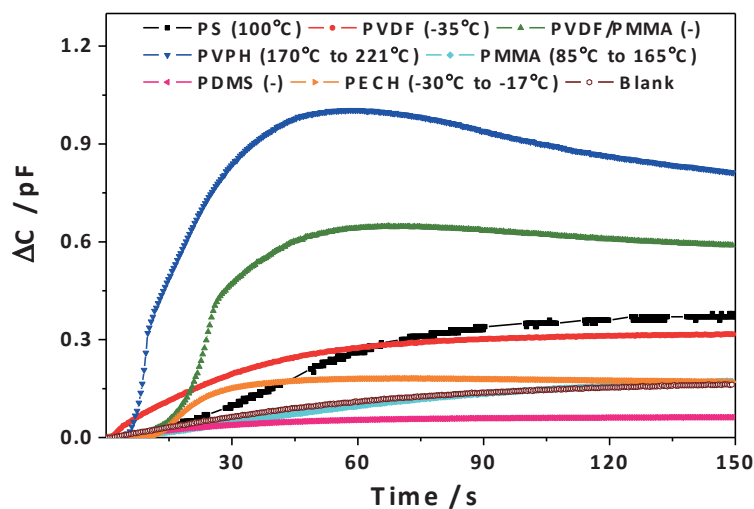
### 3. Results and discussion

#### 3.1. Polymer-Coated Micro Interdigitated Electrodes

Chemo-capacitive sensors detect gasses by measuring changes in the dielectric constant of media that are caused by the presence of analyte gasses. In the case of multi-layered chemocapacitors based on interdigitated electrodes, the capacitance of the device can be calculated by a parallel partial capacitance technique.[25] In our design (see **Figure 1**), this leads to a calculated value of 1.3 pF, while we measured 2.2 pF. Although it is possible to measure changes in capacitance with these bare IDEs (see **Figure 2**, blank), sensitivity and specificity can be significantly increased by coating the IDE surface with a polymer (which increases the capacitance of the IDE to 5-7 pF). Therefore, to capture and concentrate an analyte gas (acetone) in the sensor, a polymer layer was applied to the surface of the IDE.

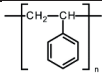

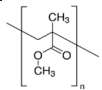
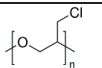
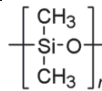
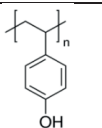
**Figure 2** shows the real-time evolution of the change in capacitance during acetone exposure of various polymers coatings (see for details of gas measurements *Supporting Information* Section 3, Figure S7). All curves showed an increase in capacitance when acetone (with a dielectric constant of 21) is introduced. The tested polymers are listed in **Table 1**. These polymers were selected because of their known affinity for acetone in other types of sensors.[22, 23] From literature, we expected the glass transition temperature ( $T_g$ ) of the applied polymers to be important for the response rate of the sensor. At  $T_g$  well below the temperature of use (herein room temperature), the analyte molecules that are absorbed to the polymer layer are expected to diffuse rapidly into the material due to the mobility of random polymer chains.[26] In general, this contributes to a faster response and recovery time and also reduces the chance of hysteresis effects. The effect of  $T_g$  on the response of the sensor is clearly visible in **Figure 2**. The PMMA and PS coated M-IDEs (with

higher  $T_g$ ) respond much slower than the other polymers such as PVDF, PECH or PDMS, which have a much lower  $T_g$ . However, even though PVPH has a high  $T_g$  (170 – 221 °C), the response of this polymer to acetone is both fast and strong.[22] In this case, the  $T_g$  seems to be not so important. Of all the polymers we tested, highest acetone responses were observed from a PVPH coated M-IDE. Therefore, we used this polymer in our further study.



**Figure 2.** Time-dependent capacitive responses towards acetone vapor of different polymers on M-IDEs compared to a blank M-IDE at room temperature,  $T_g$  (°C) of each polymer is shown in brackets. All polymer layers were prepared from 10 wt. % solutions. Acetone was introduced at  $t = 0$  s and continuously supplied during the full 150 s.

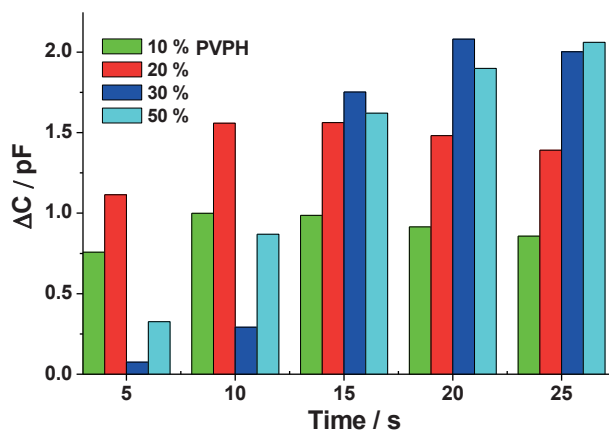
**Table 1.** Polymers tested for their acetone affinity.

Name	Abbrev.	Chemical Structure	Solvent	T <sub>g</sub> (°C)	Dielectric constant ( $\epsilon_r$ )
Polystyrene	PS		Toluene	100	2.4 - 2.7
Poly-vinylidene fluoride	PVDF		Dimethyl-formamide	-35	8.0 - 9.5
Poly-(methyl methacrylate)	PMMA		Dimethyl-formamide	85 to 165	2.8 - 4
Poly-epichlorohydrin	PECH		Tetrahydrofuran	-30 to -17	1.7
Poly-dimethyl-siloxane	PDMS		-	-125	2.75
Poly (4-vinyl phenol)	PVPH		Ethanol	170 to 221	3.5 - 5 [27-29]

Apart from the difference in affinity towards acetone for different polymers, the thickness of the polymer layer is also an important parameter for the response of the sensor. Theoretically, optimal sensitivity is obtained when the polymer layer is thick enough to enclose the electric field of the IDE.[30] In our configuration, this means a thickness of 15  $\mu\text{m}$ . We investigated the influence of the PVPH layer thickness by increasing the concentration of the polymer solution used for spin coating. The lowest concentration that was used, 10 wt. %, corresponds to a resulting layer of 1  $\mu\text{m}$  as measured by SEM. **Figure 3**



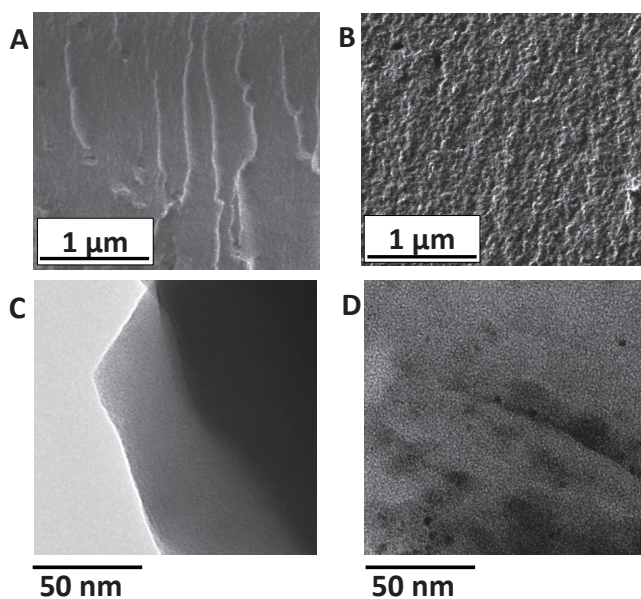
shows the response towards acetone of M-IDEs coated with varying thicknesses of PVPH. As expected, the strength of the signal increases with increasing PVPH concentration (thicker polymer layer). However, at the same time, the response of the sensor is slower. This is caused by the slower diffusion of acetone throughout the entire polymer layer.[26] Optimum conditions that lead to a fast response time in combination with a high capacitive change are reached when a solution of 20 wt. % PVPH is used for coating. Therefore, we chose 20 wt. % PVPH (herewith **PVPH 20**) as fixed concentration for our further studies. Note that with this concentration typically a polymer layer of several microns thick was obtained. This means that the polymer layer does not include the full electric field of the M-IDE and the sensor will be susceptible to adsorption of the analyte onto the polymer surface and swelling/deswelling processes in addition to absorption of the analyte in the polymer bulk. This explains the shape of the curves in **Figure 2** (and see also **Figure 5** below): initially, the capacitance increases because acetone adsorbs on the polymer surface and diffuses into the polymer layer. Subsequently, the polymer layer deswells, which decreases the capacitance at longer time scales.



**Figure 3.** Capacitive responses towards acetone of M-IDEs coated with PVPH layers prepared from solutions of different concentrations. Increasing PVPH concentration corresponds with thicker polymer layers (10 wt. % PVPH corresponds to a 1  $\mu\text{m}$  thick polymer layer).

### 3.3 Polymer-based nanocomposite as a sensitive layer towards analytes on M-IDE

In order to further increase the sensitivity of our M-IDE sensor, we added amine-functionalized silicon nanoparticles (Si NPs) to the polymer layer. These NPs could potentially improve the device in two ways: First, addition of the Si NPs disrupts the structure of the nanocomposite, and thereby increases the porosity of the polymer layer, and thus increases the polymer surface available for adsorption and diffusion rates. This would lead to faster response times and allows for more acetone to be captured in the layer.[29] Second, specific chemical interactions (from H-bond to imine formation) between the amine groups on the NPs and acetone might enhance both specificity and sensitivity of the sensor.



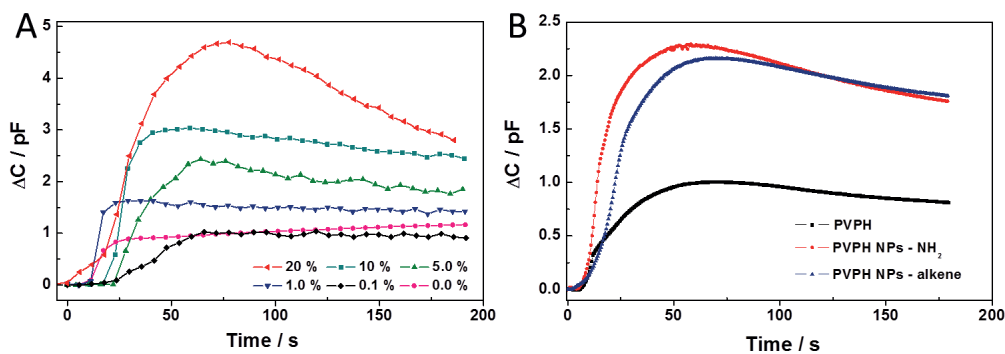
**Figure 4.** Cross-sectional SEM images of a pure PVPH layer (A) and a NC film of PVPH with 1 wt. % Si NPs (B). TEM images of pure PVPH (C) and the NC containing PVPH and 1 wt. % Si NPs (D).

**Figure 4 A and B** showed the morphology of both the pure PVPH polymer layer and the NC film with 1 wt. % of NPs, respectively. As expected, the surface of the polymer layer with NPs added is rougher after breaking it for SEM measurements than the pristine film, indicating a higher porosity. A higher porosity after mixing NPs into a polymeric system was also observed by Chen *et al.*[29] TEM images show that the nanoparticles are well dispersed in the polymer layer and do not form large clusters (**Figure 4D**). Further characterization of the NC layer can be found in the supporting information.

The acetone response of M-IDEs coated with NCs containing different amounts of NPs is shown in **Figure 5A**. Indeed, the response increased with an increasing concentration of NPs present in the polymer layer. Again, the decrease in capacitance measured at longer time scales is probably caused by deswelling effect of the NC layer. The maximum response that was measured, a factor 5 increase (from 1 to 5 pF), was measured when 20 wt. % NPs were added. However, that signal was not stable over time. NC layers with NP concentrations of 10 wt. % and lower showed more stable responses. Less than 1 wt. % of NPs in the NC layer did not noticeably enhance the response of the PVPH layer. We calculated the increase of polymer surface available for the adsorption of the different samples shown in **Figure 5A**. The results are shown in **Table 3** (for calculation details see *Supporting Information*). Assuming the polymer layer is 3  $\mu\text{m}$  thick, the surface of the M-IDE is increased from 0.6  $\text{mm}^2$  to 73  $\text{mm}^2$  by the addition of 1 wt. % NPs to the 20 wt. % PVPH solution used for spin-coating.

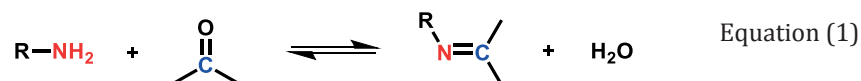
**Table 3.** Calculated surface enhancement due to nanoparticles addition.

NPs (wt. %)	0.1 %	1.0 %	5.0 %	10.0 %	20.0 %
Surface enhancement factor	14	124	560	1008	1677



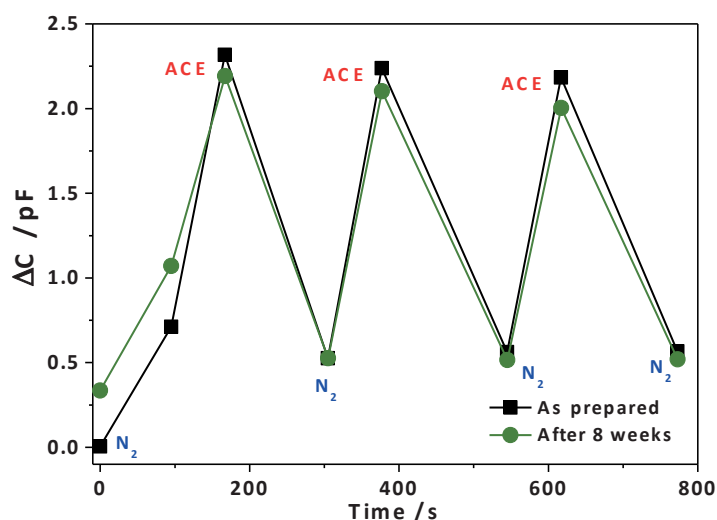
**Figure 5.** Time-dependent capacitive response towards acetone of NC sensing layers on M-IDEs. Comparison of different concentrations of NPs in 20 wt. % PVPH (A). Comparison of NC sensing layers containing  $\text{NH}_2$  functionalized and alkene functionalized NPs. For these layers 5 wt. % of NPs was added to 10 wt. % of PVPH (B).

Apart from the surface enhancement effect, we tested whether the  $\text{NH}_2$  groups on the surface of the nanoparticles led to any additional signal enhancement towards acetone. This was expected because amine groups are known to react with acetone to yield imines:



$\text{NH}_2$  groups on the NPs surface thus facilitate chemisorption of acetone on the NPs surface in addition to the physisorption on the polymer surface. This way, more acetone can be contained in the NC layer. Whether acetone is present in gas form (left part of **Equation 1**) or bound form (right part) is not expected to have an effect on the dielectric constant of the total. In **Figure 5B**, the acetone response of NCs containing  $\text{NH}_2$ -functionalized Si NPs is compared to the response of NPs with alkene chains on their surface (which are not expected to bind acetone specifically). **Figure 5B** shows that the response of the M-IDEs coated with NCs that contain  $\text{NH}_2$ -functionalized NPs does not differ significantly from M-IDEs coated with NCs that contain Si NPs with alkyl groups on

their surface. Therefore, we conclude that the enhancement of the acetone response caused by  $\text{NH}_2$ -functionalized Si NPs is due to the increased available surface area of the polymer layer and not by the specific binding of acetone.



**Figure 6.** Analyzed data of long-term stability of the sensor towards acetone (ACE) sensing after 8 weeks of storage in ambient environment. The capacitance response of the as-prepared PVPH 20 with 5 wt. % NPs sensor is also shown for comparison.

For any sensor, stability and repeatability are important. Moisture and oxygen, for example, could cause the degradation of the polymer layer when samples are stored under ambient environment.[31] In **Figure 6**, the capacitance response of the same device before and after 8 weeks of storage in ambient environment demonstrates the long-term stability of the NC sensing layer. Also shown in Figure 6 is the reproducibility of the sensor, which is an essential matter for sensing applications. This was examined by allowing the structure to undergo multiple injection-evaporation cycles of acetone as a model organic solvent with a rapid response time. The NC polymer film in our study showed good repeatability after three consecutive injection cycles, although it suffers from some irreversible damage

after its first exposure to acetone. When acetone molecules were injected, a response capacitance change was detected due to the infiltration of gas molecules into the NC film. When the acetone flow was turned off and N<sub>2</sub> was injected, the acetone molecules diffused out of the NC layer, which quickly reduced the capacitance. As can be seen in **Figure 6**, 100 s is not enough time to allow all acetone to diffuse out of the NC layer since after exposure to acetone the capacitance does not return to its initial value completely. Longer recovery times do lead to a lower capacitance, but after 8 weeks the initial capacitance is still higher than directly after preparation. This change in capacitance after the first exposure to acetone is probably caused by the removal of trapped air bubbles that were initially present in the NC layer. After acetone exposure the layer is denser, which means the dielectric constant is higher. After the first exposure cycle to acetone, the device does return to the same capacitance value after every cycle, even after 8 weeks of storage.

Despite these good results regarding repeatability and quick response-recovery characteristics, a 5 % decay of the measured response was detected after two injection-evaporation cycles. This decay can also be explained by the removal of air from the NC layer when it is exposed to acetone. When this happens, less acetone can be contained by the NC layer, which leads to a lower detected capacitance. The 8-week storage period did not affect the measured capacitance, since the height of the third peak of the fresh sample is equal to the first peak after 8 weeks of storage. The NC sensing layer has thus good long-term storage stability.

#### **4. Conclusion**

In conclusion, we have successfully developed a capacitive chemical sensor based on an M-IDE coated with a polymeric nanocomposite layer consisting of Si NPs and PVPH. Of all tested polymers, PVPH showed highest affinity towards acetone. The addition of surface-modified Si nanoparticles led to an increase in polymer surface available for adsorption, which enhanced the response of the device towards acetone. The sensing response towards acetone at room temperature proved that the turn-on and -off exposure to this analyte was reversible with good reproducibility (5 % decay) after multiple cycles of gas exposure. Furthermore, the sensing response of the NC device remained stable after 8 weeks of

storage in ambient atmosphere. This indicates reliable response and recovery characteristics of the sensor. The development of this type of sensor provides an inexpensive and easy-to-handle device to detect chemical analytes. Nonetheless, much lower concentrations of analyte should be further studied for a more detailed examination of the sensor's sensitivity. Significant work remains towards improving sensing process and selectivity together with improving nanocomposite materials of the current sensor for advanced applications.

## References

- [1] D. Zhang, A. Liu, H. Chang, B. Xia, Room-temperature high-performance acetone gas sensor based on hydrothermal synthesized SnO<sub>2</sub>-reduced graphene oxide hybrid composite, *RSC Adv*, 5(2015) 3016-22.
- [2] Y. Xiao, L. Lu, A. Zhang, Y. Zhang, L. Sun, L. Huo, et al., Highly Enhanced Acetone Sensing Performances of Porous and Single Crystalline ZnO Nanosheets: High Percentage of Exposed (100) Facets Working Together with Surface Modification with Pd Nanoparticles, *ACS Appl Mater Interfaces*, 4(2012) 3797-804.
- [3] Q. Jia, H. Ji, Y. Zhang, Y. Chen, X. Sun, Z. Jin, Rapid and selective detection of acetone using hierarchical ZnO gas sensor for hazardous odor markers application, *J Hazard Mater*, 276(2014) 262-70.
- [4] P. Wang, D. Wang, M. Zhang, Y. Zhu, Y. Xu, X. Ma, et al., ZnO nanosheets/graphene oxide nanocomposites for highly effective acetone vapor detection, *Sens Actuators B: Chem*, 230(2016) 477-84.
- [5] A. Reyes-Reyes, R.C. Horsten, H.P. Urbach, N. Bhattacharya, Study of the Exhaled Acetone in Type 1 Diabetes Using Quantum Cascade Laser Spectroscopy, *Anal Chem*, 87(2015) 507-12.
- [6] C. Deng, J. Zhang, X. Yu, W. Zhang, X. Zhang, Determination of acetone in human breath by gas chromatography-mass spectrometry and solid-phase microextraction with on-fiber derivatization, *J Chromatogr B*, 810(2004) 269-75.
- [7] W. Chuji, B.S. Anand, An acetone breath analyzer using cavity ringdown spectroscopy: an initial test with human subjects under various situations, *Meas Sci Technol*, 19(2008) 105604.
- [8] L. Wang, K. Kalyanasundaram, M. Stanacevic, P. Gouma, Nanosensor Device for Breath Acetone Detection, *Sens Lett*, 8(2010) 709-12.
- [9] M. Righettoni, A. Tricoli, S. Gass, A. Schmid, A. Amann, S.E. Pratsinis, Breath acetone monitoring by portable Si:WO<sub>3</sub> gas sensors, *Anal Chim Acta*, 738(2012) 69-75.
- [10] H. Huang, J. Zhou, S. Chen, L. Zeng, Y. Huang, A highly sensitive QCM sensor coated with Ag+-ZSM-5 film for medical diagnosis, *Sens Actuators B: Chem*, 101(2004) 316-21.
- [11] M.M. Ayad, G. El-Hefnawey, N.L. Torad, A sensor of alcohol vapours based on thin polyaniline base film and quartz crystal microbalance, *J Hazard Mater*, 168(2009) 85-8.
- [12] H.-W. Zan, C.-H. Li, C.-C. Yeh, M.-Z. Dai, H.-F. Meng, C.-C. Tsai, Room-temperature-operated sensitive hybrid gas sensor based on amorphous indium gallium zinc oxide thin-film transistors, *Appl Phys Lett*, 98(2011) 253503.
- [13] R. Ermanok, O. Assad, K. Zigelboim, B. Wang, H. Haick, Discriminative Power of Chemically Sensitive Silicon Nanowire Field Effect Transistors to Volatile Organic Compounds, *ACS Appl Mater Interfaces*, 5(2013) 11172-83.
- [14] M.C. Zaretsky, J.R. Melcher, C.M. Cooke, Moisture sensing in transformer oil using thin-film microdielectrometry, *IEEE Transactions on Electrical Insulation*, 24(1989) 1167-76.
- [15] W. Qu, W. Wlodarski, A thin-film sensing element for ozone, humidity and temperature, *Sens Actuators B: Chem*, 64(2000) 42-8.



- [16] C. Hagleitner, A. Hierlemann, D. Lange, A. Kummer, N. Kerness, O. Brand, et al., Smart single-chip gas sensor microsystem, *Nature* 414(2001) 293-6.
- [17] F. Josse, R. Lukas, R. Zhou, S. Schneider, D. Everhart, AC-impedance-based chemical sensors for organic solvent vapors, *Sens Actuators B: Chem*, 36(1996) 363-9.
- [18] R. Casalini, M. Kilitziraki, D. Wood, M.C. Petty, Sensitivity of the electrical admittance of a polysiloxane film to organic vapours, *Sens Actuators B: Chem*, 56(1999) 37-44.
- [19] A.M. Kummer, A. Hierlemann, Configurable electrodes for capacitive-type sensors and chemical sensors, *IEEE Sens J*, 6(2006) 3-10.
- [20] S. Pandey, G.K. Goswami, K.K. Nanda, Nanocomposite based flexible ultrasensitive resistive gas sensor for chemical reactions studies, *Sci Rep*, 3(2013) 2082.
- [21] Z. Wu, X. Chen, S. Zhu, Z. Zhou, Y. Yao, W. Quan, et al., Enhanced sensitivity of ammonia sensor using graphene/polyaniline nanocomposite, *Sens Actuators B: Chem*, 178(2013) 485-93.
- [22] H. Xie, Q. Yang, X. Sun, J. Yang, Y. Huang, Gas sensor arrays based on polymer-carbon black to detect organic vapors at low concentration, *Sens Actuators B: Chem*, 113(2006) 887-91.
- [23] Z. Ying, Y. Jiang, X. Du, G. Xie, J. Yu, H. Tai, Polymer coated sensor array based on quartz crystal microbalance for chemical agent analysis, *Eur Polym J*, 44(2008) 1157-64.
- [24] Y. Zhong, F. Peng, F. Bao, S. Wang, X. Ji, L. Yang, et al., Large-Scale Aqueous Synthesis of Fluorescent and Biocompatible Silicon Nanoparticles and Their Use as Highly Photostable Biological Probes, *J Am Chem Soc*, 135(2013) 8350-6.
- [25] R. Igreja, C.J. Dias, Analytical evaluation of the interdigital electrodes capacitance for a multi-layered structure, *Sens Actuators A: Phys*, 112(2004) 291-301.
- [26] C.E. Rogers, Permeation of gases and vapours in polymers, *Polymer Permeability*, Elsevier Applied Science 1985, pp. 11-73.
- [27] Y.-J. Kim, J. Kim, Y.S. Kim, J.-K. Lee, TiO<sub>2</sub>-poly(4-vinylphenol) nanocomposite dielectrics for organic thin film transistors, *Org Electron*, 14(2013) 3406-14.
- [28] W. Han, H.-S. Lee, U.K.H. Bangi, B. Yoo, H.-H.C.P.A.T.R. Park, Dielectric properties of poly(4-vinylphenol) with embedded PbO nanoparticles, *Polym Adv Technol*, 27(2016) 245-9.
- [29] F.-C. Chen, C.-W. Chu, J. He, Y. Yang, J.-L. Lin, Organic thin-film transistors with nanocomposite dielectric gate insulator, *Appl Phys Lett*, 85(2004) 3295-7.
- [30] R. Igreja, C.J. Dias, Dielectric response of interdigital chemocapacitors: The role of the sensitive layer thickness, *Sens Actuators B: Chem*, 115(2006) 69-78.
- [31] F.A. Harraz, A.A. Ismail, H. Bouzid, S.A. Al-Sayari, A. Al-Hajry, M.S. Al-Assiri, A capacitive chemical sensor based on porous silicon for detection of polar and non-polar organic solvents, *Appl Surf Sci*, 307(2014) 704-11.



## Chapter 4



### Gas Sensing Performance at Room Temperature of Nanogap Interdigitated Electrodes for the Detection of Acetone at Low Concentration

#### **Abstract**

A facile approach for fabrication of large-scale interdigitated nanogap electrodes (nanogap IDEs) with controllable gap was demonstrated with conventional micro-fabrication technology to develop chemocapacitors for gas sensing applications. In this work, interdigitated nanogap electrodes (nanogap IDEs) with gaps from 50-150 nm have been designed and processed at full wafer-scale. These nanogap IDEs were then coated with poly(4-vinyl phenol) as a sensitive layer to form gas sensors for acetone detection at low concentrations. These acetone sensors showed excellent sensing performance with dynamic range from 100,000 ppm to 10 ppm of acetone at room temperature and the observed results are compared with conventional interdigitated microelectrodes according to our previous work. Sensitivity and reproducibility of devices are discussed in detail. Our approach of fabrication of nanogap IDEs together with a simple coating method to apply the sensing layer opens up possibilities to create various nanogap devices in a cost-effective manner for gas sensing applications.

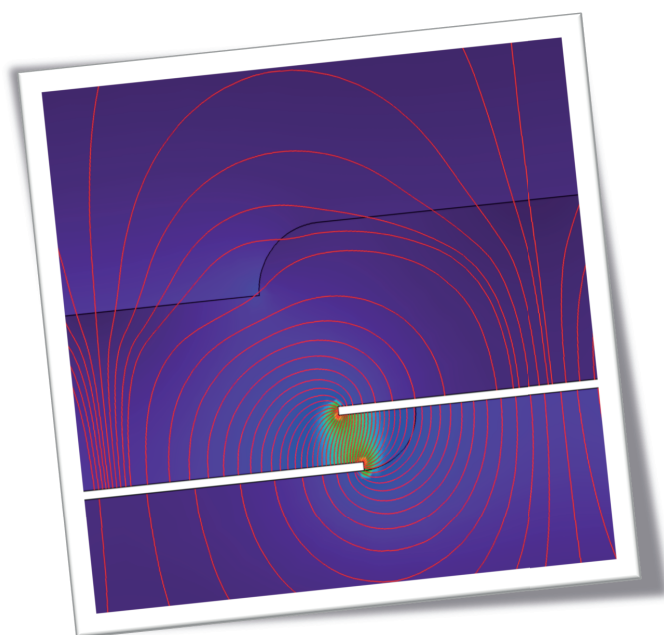
*This chapter has been submitted as:*

*"Gas Sensing Performance at Room Temperature of Nanogap Interdigitated Electrodes for the Detection of Acetone at Low Concentration", [Quyen Nguyen Minh](#), Anke Kuijk, Hien D. Tong, Franc van de Bent, Pepijn Beekman, Han Zuilhof, and Cees J.M. van Rijn, Royal Society of Chemistry Advances, **2017**.*

**Keywords**

Nanogap, Interdigitated Electrodes, VOCs, Gas sensor, Nanocomposite, Chemocapacitor, Acetone.

**Graphical Abstract**



## 1. Introduction

Nanogap devices have attracted numerous fundamental and application oriented studies because of their great potential in solving challenging problems at molecular and nano scale.[1] They have widely been employed not only for molecular electronics,[2] optical plasmonics,[3] but also in tunneling based sensors as biosensors and chemical sensors.[4,5] Their drawback preventing applications still remains: a reproducible and cost-effective fabricating process yielding stable electrical contacts. Different methods have been applied to address these issues with respect to improving fabrication processes [6–9] and/or modifying nano-electrode structures.[10–12] Nanogap devices are promising to become a new generation of devices that operate fast with a high sensitivity, consume less power, and can be applied as portable devices.

Taking into account the rapid progress of gas sensing applications, detection at low concentration is one of the greatest possibilities in using nanogap devices.[13–19] Up to now, there are not many studies on the detection of volatile organic compounds (VOCs) with nanogap devices. To investigate gas-sensing properties of nanogap devices towards VOCs for air quality control is an appealing challenge. For example, acetone, one of the most common VOCs, is widely used in the industry and laboratory for synthesis, solvent, cleaning agents, etc. It is a nontoxic agent at a low concentration, but acetone can cause harm and danger to human health when it exceeds specific threshold values, and can also affect environmental safety. A high concentration of acetone can cause to the human body several syndromes: fatigue, headache and nausea when being inhaled,[20] irritated eyes and skin or damage throat when being exposed when its concentration are above 10,000 ppm.[21,22] Not only being widely used for in-house air quality control but acetone sensors have been further exploited for medical diagnosis as well. A number of recent investigations prove that acetone, as one of the biomarkers in human breath, represents for diabetes diagnosis because a relatively high concentration can be an indication of diabetes.[23–25] Therefore, it is essential and significant to effectively detect acetone gas in different ranges of concentration.

Inspired by these promising goals in the field of sensing devices, we focused on the exploration of gas sensing properties of nanogap IDEs. There has been significant progress in realizing structures for nanogap devices, however, the manufacturing methods can be significantly simplified using a proper combination of conventional micro-fabrication techniques. We present here for the first time a new generation of nanogap IDEs featuring a 3D comb structure for the detection of acetone. As a VOC sensitive material of choice, Poly (4-vinyl phenol) (PVPH) was used as an active material to adsorb acetone vapor with a high affinity according to previous work.[26,27] The capacitive behavior of nanogap IDEs devices as a chemo-capacitor was simulated using COMSOL Multiphysics 5.2. Furthermore, we report our preliminary studies of acetone adsorption on nanogap IDEs at room temperature. As expected, the device exhibits excellent sensing performance to acetone vapor at low concentration. The detection of acetone vapor of this device ranges from 1000 down to 10 ppm. Based on characteristics of the active layer PVPH combined with the corresponding structure of nanogap IDEs, the devices' performance was also further examined under different humidity conditions.

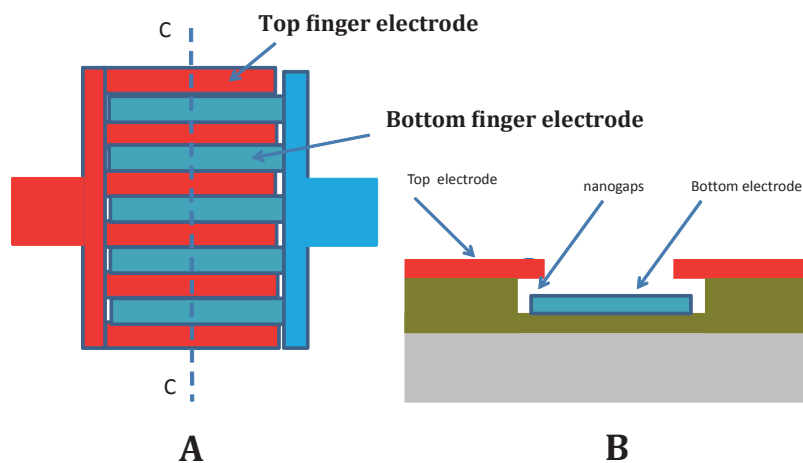
## **2. Material and methods**

### **2.1. Chemicals**

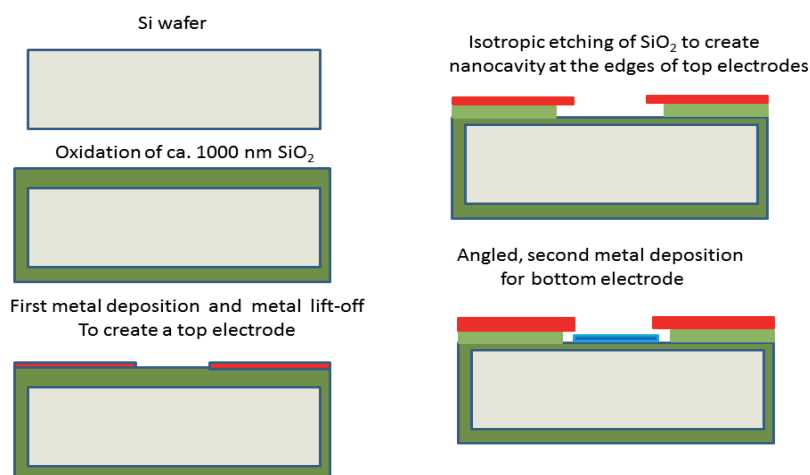
Poly (4-vinyl phenol) (PVPH)  $M_w \sim 11,000$ , and absolute ethanol (98%) were purchased from Sigma Aldrich. All reagents were used as received.

### **2.2. Fabrication of interdigitated nanogap electrodes as a chemocapacitor**

An overview and a cross section of the nanogap IDEs are shown in **Figure 1**. The nanogap IDEs has a patterned area of  $1\text{ mm} \times 1\text{ mm}$ , consisting of 250 top finger electrodes and 250 bottom finger electrodes. Each finger electrode has a width and length of  $2\text{ }\mu\text{m}$  and  $1000\text{ }\mu\text{m}$ , respectively. A distance (the gap) from top to bottom electrodes is determined by an etching depth of a sacrificial  $\text{SiO}_2$  layer, and a thickness of the bottom electrode.



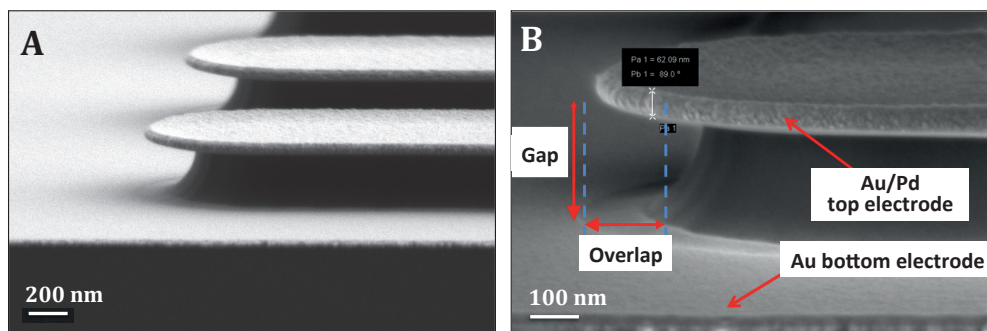
**Figure 1.** An overview of the interdigitated nanogap electrodes - (A). A cross section (over C-C) of one bottom electrode and its two adjacent top electrodes, showing the nano gaps across the finger electrodes - (B).



**Figure 2.** Fabrication process of an interdigitated nanogap electrodes (nanogap IDEs).

The process steps of the nanogap IDEs are shown in **Figure 2**, and are as follows: a 4-inch {100}-Si is coated with 1000 nm of wet-thermal silicon dioxide ( $\text{SiO}_2$ ), followed by microlithography, a metal deposition and a metal lift-off to form the top finger electrode array. The deposited metal layer is a layer of ca. 30 nm platinum. Afterwards, the  $\text{SiO}_2$  is partially and isotropically etched using buffered hydrofluoric acid (BHF; 1:7) to create a nanocavity at the edges of the top electrodes.

Next a thin-film evaporation under an angle is carried out to deposit ca. 30 nm of gold (Au) layer on to the substrate and into the nanocavity to create the second electrodes of the nanogap IDEs. **Figure 3** shows SEM images of the fabricated nanogap IDEs. It can be seen that the top and bottom electrodes are separated with a gap of ca. 250 nm, and an overlap of the top and bottom electrodes form a capacitor. Please note that to form the nanogap IDEs capacitor no nanolithography is required and only conventional micro-fabrication is applied.



**Figure 3.** An overview SEM image of several electrodes of the nanogap IDEs on a silicon chip - (A). SEM image shows top and bottom electrodes and its overlap that creates a capacitor - (B).

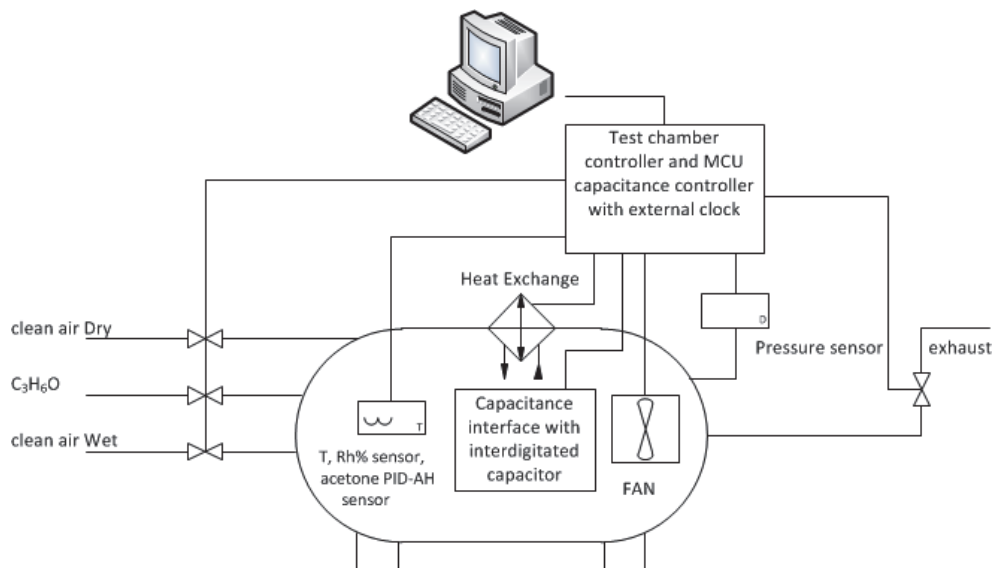


### 2.3. Polymer coating of nanogap IDEs

PVPH was dissolved in ethanol by sonication for several minutes until a clear polymer solution was obtained. nanogap IDEs as nanogap capacitors were coated with polymer by dipping them slowly into the polymer solution, with the electrodes in a vertical position, until the liquid reached the bottom of the electrodes. The chip was held in this position until the gaps between the electrodes were filled with polymer solution by capillary action. This took less than a minute and filling of the gaps could be observed by a changing reflection of light. When the gaps had been completely filled, the chip was submerged in the polymer solution completely, after which the chip was spin coated at 3000 rpm for 2 minutes to form a thin layer. Finally, the sample was annealed at 60 °C overnight.

### 2.4. Acetone gas sensing setup

An experimental Signal Measurement System (SMS) was used to characterize the behavior of the nanogap IDEs in a clean air atmosphere. The SMS is shown in **Figure 4**. The humidity, measured with a calibrated AHT-200-01 sensor (Ohmic Industries), in the volume controlled chamber (8.3 liter) is computer regulated with high speed inlet and exhaust valves running through, or by passing, a bubbler. The selected humidity sensor is a Thermal Conductivity type. This sensor is capable of measuring in an environment with volatile chemicals such as ketones. A downside of this sensor type is that it does require a temperature compensation of the output data and this task is programmed and operated by the PC controller. The temperature in the chamber is regulated with a Peltier element, a heat sink and a fan both inside and outside the SMS. Overpressure is regulated with an exhaust valve monitored and recorded with a pressure transducer. When the internal pressure exceeds ambient levels the exhaust valve will open until the pressure relaxes to ambient level.



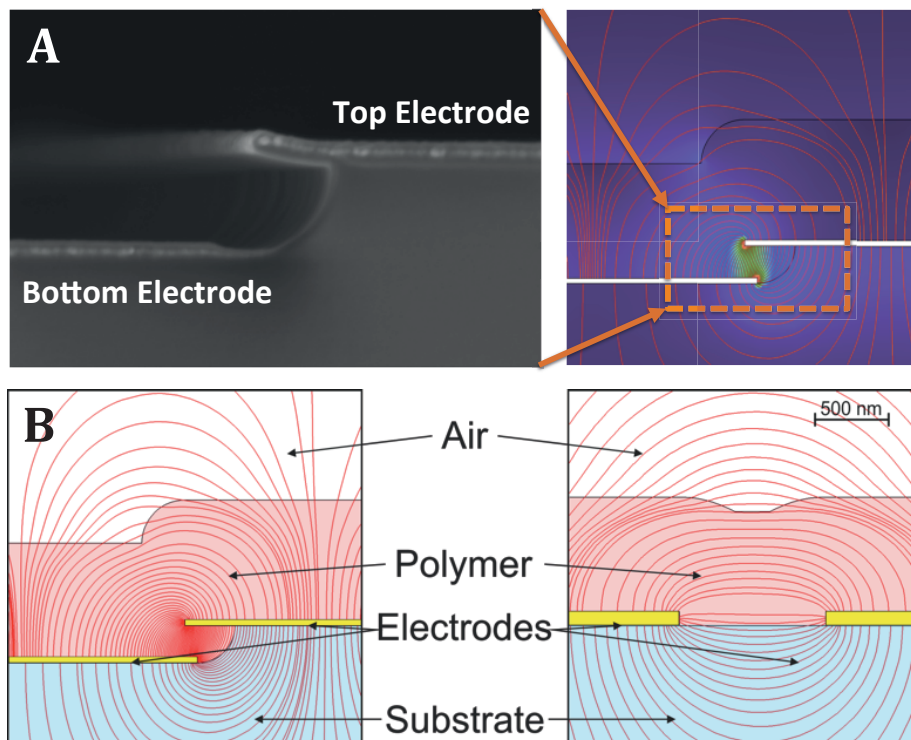
**Figure 4.** Setup of the Signal Measurement System for sensing Acetone concentrations.

A bubbler with a diluted acetone concentration also controlled by a high-speed valve was used to insert acetone. The concentration in the system was measured using a calibrated PID-AH sensor (alpha sense), capable of sensing range from 0.1 ppm to 6000 ppm of acetone. The output of this reference sensor was fed into a calibrated DMM operating under PC control. The data of this reference sensor was used in a software feedback loop of the SMS. The nanogap IDEs capacitance value was measured at roughly 2 MHz depending on the nanogap IDEs capacitance, using the Texas Instruments FCD2212. This semiconductor was placed on an experimental measurement PCB clip, directly next to the pogo pins that connect to the nanogap IDEs under test. The FCD2212 offers a 300aF resolution with 168dB dynamic range and, was interfaced to the control PC with a Micro Controller Unit (MCU) and programmed to deliver new readout values on command. The control computer executes a script file, used for setting the desired temperature, humidity and acetone concentration values in the SMS. Every line in the script file triggers a read command of all reference sensors and experimental nanogap IDEs capacitor value and, both wanted and

current values are stored in an Excel file structure for further analysis. With the script file, measurements can be designed and repeated as chosen, using the same timing and variable settings in the SMS.

### **3. Finite element analysis of nanogap IDEs as a capacitor**

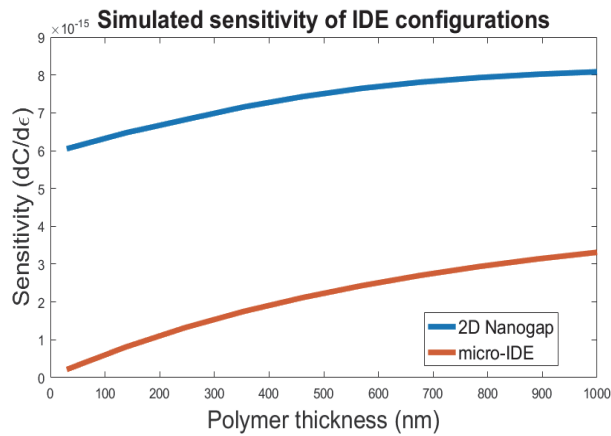
The presence of analytes in the sensing layer induces a change in the dielectric constant. This change is measured as a change in the capacitance value of the nanogap IDEs. The greater the change in capacitance relative to the total capacitance of the system, the more sensitive the sensor is. Modelling can give insight into factors maximizing signal and minimizing parasitic capacitance.[28] Analytical prediction of capacitance is often complex, because electric fields extend into substrates and different media.[29–31] Also, analytical models are usually only correct for specific geometries not relevant in this case.[32] Therefore, we used finite element analysis using COMSOL Multiphysics 5.2 (COMSOL Inc., Burlington MA, USA) to show the effect of two electrode designs: a rectangular electrode array with a micro-gap as used in previous experiments,[33] and the rectangular electrode array with a nanogap introduced in this paper. In both designs a polymer coating of 800 nm was applied. Parametric sweeps of geometrical and material parameters were performed. As the complete chip geometry requires considerable computing power to model, these simplified models were studied to gain approximations of the expected electric field and capacitance.



**Figure 5.** A cross-sectional SEM image of a nanogap (A - left) and its electric field line distributions as calculated by COMSOL (with illustrative overlay) (A - right). Capacitors are composed of two electrodes covered in a polymer film, supported by silicon nitride, in air environment. A typical nanogap capacitor (250 nm vertical spacing, 130 nm horizontal overlap, 800 nm polymer thickness) (B - left). A typical micro-IDEs (10  $\mu\text{m}$  x 0.1  $\mu\text{m}$  x length, 1  $\mu\text{m}$  spacing). The field line density is indicative of the electric field strength (B - right).

From theory, it has been known that electric fields are highest near regions of conductors with small radius of curvature as a consequence of the high local charge density.[34,35] Closer to these regions, more charge can be stored as the dielectric is more strongly polarized.[36] Therefore, it can be concluded that protruding parts of the geometry, like electrode edges, contribute most to the capacitance of the system. Furthermore, many

simplified nanogap IDEs models predict that the so called fringe capacitance is more significant when the electrodes are placed more closely together.[30,37] This implies that the sensing layer may be made be thicker to include interactions with the electric field and fluctuations of the capacitance further away from the electrodes.[25] However, this observation is only valid for electrodes for which the separation is much larger than the electrode thickness, which does not hold for the design discussed in this work. For our design, the field in between the upper and lower electrode surfaces dominates the field outside as shown in **Figure 5**. Therefore, the thickness of the polymer layer on top of the electrodes is not expected to influence the response of the sensor much.



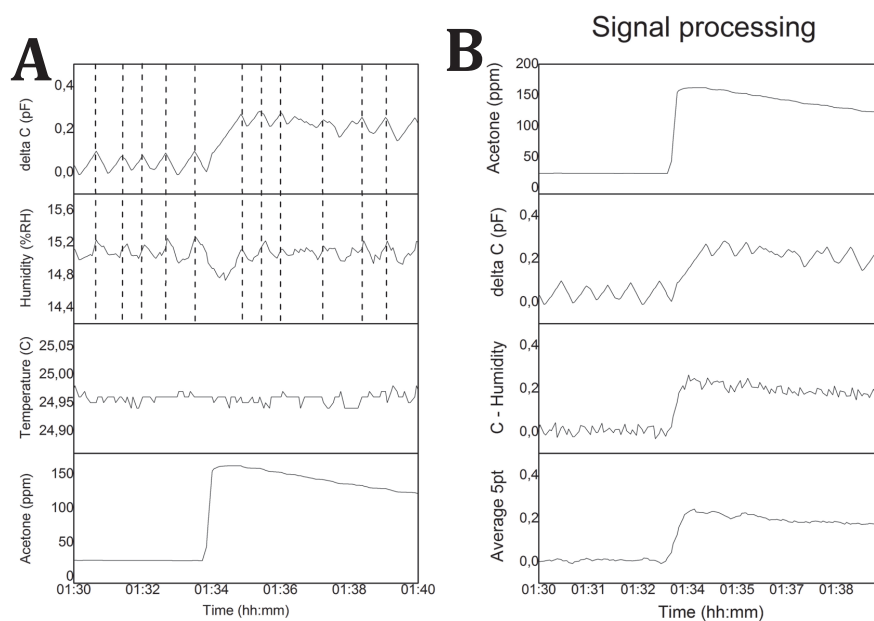
**Figure 6.** Simulated sensitivity of a typical micro IDEs and a nanogap capacitor with a planar geometry. An arbitrary change in permittivity of the polymer yields a much larger relative change in capacitance in a two dimensional geometry.

From COMSOL simulations, it became apparent that the electric field in a nanogap capacitor is much stronger than that of a typical IDEs in comparable circumstances [voltage, polymer thickness, substrate thickness].[23,24,28] The maximum electric field strength of a nanogap IDEs was calculated to be 4.47 times higher. Furthermore, the field

does not extend quite as far into the substrate in case of nanogap IDEs. This implies that the sensing layer can be thinner and therefore more responsive to changes in the environment. For the geometries discussed here, an arbitrary change in dielectric constant of the polymer yields a relative change in simulated capacitance that is 3.14 times lower for the micro-IDEs, see **Figure 6**. Compared to a planar IDEs having electrodes with similar dimensions (250 nm spacing, 2  $\mu$ m width), the field of a nanogap IDEs is 3.68 times higher and the simulated sensitivity is 1.64 times better.

## 4. Results and Discussion

### 4.1. Signal Processing

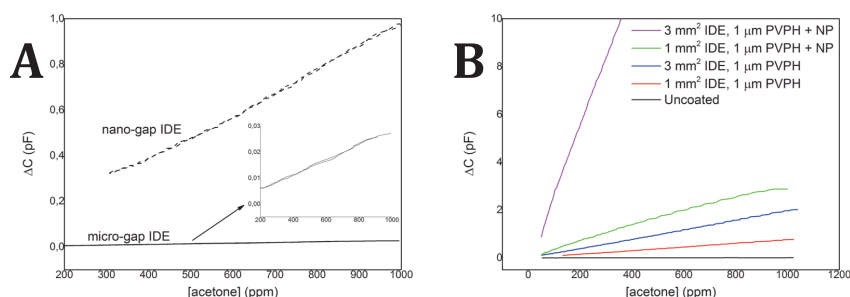


**Figure 7.** Measured signals in acetone sensing experiments: capacitance of the measured chip, humidity, temperature and acetone concentration - (A) and their signal processing - (B).

In our set-up, four variables are measured by separate sensors: the capacitance of the chip, humidity, temperature and the acetone concentration in the measurement chamber. **Figure 7A** shows some typical values during an acetone sensing experiment. The temperature of the system is kept constant within 0.05 °C and the humidity within 0.4 %RH. The humidity inside the measurement chamber decreases when acetone is introduced, due to the hygroscopic nature of this vapor, which leads to additional adjustment of the humidity level. Furthermore, there is a strong correlation between the measured capacitance of the nanogap IDEs and the humidity of the system: peaks in the humidity signal coincide with peaks in the capacitance signal. Thus, the nanogap IDEs responds to water. Measurements showed that there is in fact a linear relationship between humidity and measured capacitance at low concentrations (*see Supporting information Figure S1*), so that it is possible to correct for variations in humidity by subtracting the humidity signal from our detected capacitance (**Figure 7B**). After application of a 10 point moving average filter, the capacitance signal follows the acetone concentration in the measurement concentration very well.

#### 4.2. Sensitivity

In previous work, we presented an acetone sensor that consists of a micro-gap interdigitated electrodes (IDEs) coated with poly (4-vinyl phenol) (PVPH).[33] **Figure 8A** shows the improvement in acetone sensitivity achieved by the new nanogap design. In this figure both chips were coated with a 2 µm thick PVPH layer. The acetone sensitivity increased from 0.028 fF/ppm for the micro-gap chip to 0.97 fF/ppm for the nanogap chip, a 35-fold increase. **Figure 8B** shows that the sensitivity could be increased further by enlarging the size of the nanogap IDEs. Here, the increase in sensitivity scales linearly with the surface area on which the chip was prepared. Furthermore, it has been shown that the addition of nanoparticles to the PVPH layer improves the sensitivity of the nanogap IDEs massively.[33]

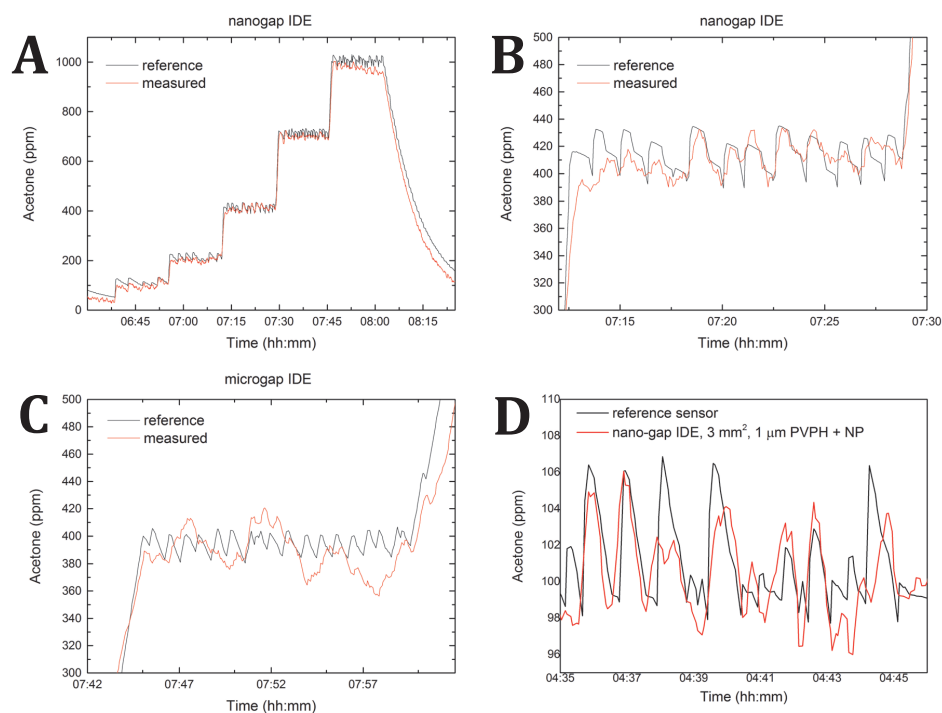


**Figure 8.** Sensitivity towards acetone of several nanogap IDEs in comparison with micro-gap IDEs. Here, the change in capacitance ( $\Delta C$ ) that was measured with presence of acetone, is plotted as a function of acetone concentration. Difference between a micro-gap IDEs and nanogap IDEs coated with 2  $\mu$ m PVPH. The inset shows the micro-gap signals in detail – (A). Nanogap IDEs on surfaces of 1 mm<sup>2</sup> and 3 mm<sup>2</sup> coated with 1  $\mu$ m PVPH with and without nanoparticles – (B).

#### 4.3. Detection Limit

To determine the detection limit of the nanogap IDEs, we applied a step-function with different levels of acetone concentration (**Figure 9A**). For high concentrations that are depicted in this graph, the measured signal follows the reference signal very well. However, to determine the detection limit of the nanogap IDEs, we need to measure at much lower acetone concentrations. Unfortunately, our set-up did not allow us to go below 100 ppm. To obtain information about the nanogap IDE's response towards smaller concentrations, we analyzed the small fluctuations in acetone concentration that appear at each step as a result of the system keeping the concentration at a certain level.



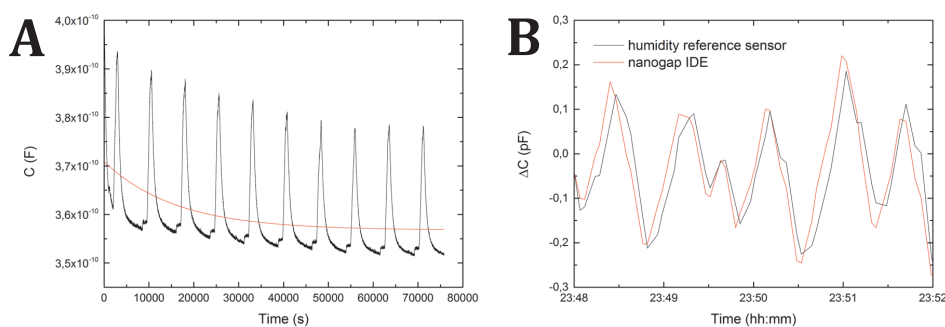


**Figure 9.** Details of measured nanogap IDEs chips and reference sensor responses to acetone. Step-function showing the response of a nanogap IDEs coated with 1  $\mu\text{m}$  PVPH towards different acetone levels - (A). Detail of (A) showing the acetone response in the 100 ppm step regime - (B). Response of comparable micro-gap IDEs chip coated with 2  $\mu\text{m}$  PVPH towards a 400 ppm step response - (C). Smallest detected peaks of 6 ppm detected by a 3 mm<sup>2</sup> nanogap IDEs chip coated with 1  $\mu\text{m}$  PVPH containing nanoparticles - (D).

**Figure 9B** shows the response of a typical nanogap IDEs to a 100 ppm steps. The measured signal follows even small steps (about 30 ppm in this case) well and stays within 20 ppm from the reference signal. For comparison, **Figure 9C** shows the response of a micro-gap IDEs towards similar step heights. It is clear that the response does not follow the small step responses detected by the reference sensor, while it stays within 50 ppm

from the reference signal. So, even though the much higher responses towards acetone of the nanogap IDEs was accompanied by a higher level of noise, the nanogap IDEs did respond better to smaller levels in acetone concentration. The smallest changes in acetone concentrations that were detected this way, were 6 ppm peaks, obtained by a 3 mm<sup>2</sup> nanogap IDEs coated with a 1 µm PVPH layer containing nanoparticles (**Figure 9D**).

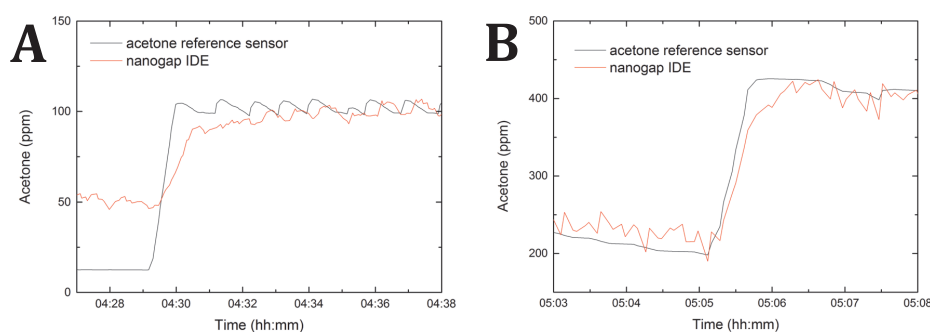
#### 4.4. Sensor properties: Stability, Response, Recovery and Durability



**Figure 10.** Stabilization of a 3 mm<sup>2</sup> nanogap-IDEs coated with 1 µm of PVPH containing nanoparticles. In black the response of the nanogap IDEs to subsequently a 100 ppm and 1000 ppm acetone peak, in red the fitted exponential with a decay time of 5 hours (A). Overlay of signals from the reference humidity sensor (black) and a nanogap IDEs (red) while no acetone is present (B). Here, the nanogap nanogap IDEs respond faster to small humidity peaks.

After fabrication the coated nanogap IDEs are stored in ambient air. Consequently, they are exposed to water vapor. When acetone response is measured, the samples are in an environment of 15 %RH, much lower than ambient air. **Figure 10A** shows that the decay time of the capacitance signal due to adaptation to the humidity level is approximately 5 to 6 hours. This time is needed to remove all water from the polymer layer. While it takes a

long time to remove all water from the polymer layer (due to hydrogen bonds within the polymer chains), the chip responds fast to the small humidity changes that are caused by the system adjusting its humidity level (**Figure 10B**). In fact, the chip responds even faster than our reference humidity sensor. The response time towards acetone was determined by looking in detail to 100 ppm and 200 ppm acetone steps (presented in **Figure 11**). For a nanogap IDEs capacitor coated with PVPH without nanoparticles, the response of the nanogap IDEs occurs at the same time as that of the reference sensor. The response time is about 1 minute in this case, as can be seen in **Figure 11B**. When nanoparticles are present in the PVPH layer, we find a different behavior. **Figure 11A** shows that the response of the sensor has a delay of about 20 seconds with respect to the reference sensor. This is clearest when looking at the small peaks between 04:32 and 04:34. The response time to 100 ppm acetone is about 4 minutes.

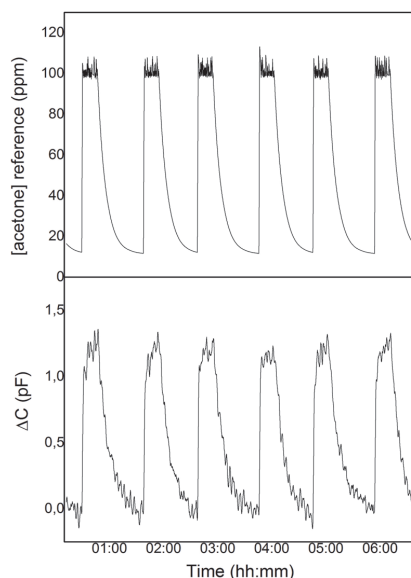


**Figure 11.** Response time of nanogap-IDEs coated with 1 µm PVPH with (A) and without nanoparticles (B).

Here, the nanogap-IDEs coated with PVPH containing nanoparticles responded with a delay and a longer response time than nanogap IDEs coated with PVPH only. As mentioned before, the nanogap IDEs containing nanoparticles are also more sensitive towards acetone and the lowest detection limit was reached using this type of coating. At present it is not

clear how the nanoparticles improve the sensitivity of the IDEs, and why the improved sensitivity goes together with a delay in response towards acetone, and a longer response time than when no nanoparticles are used.

Repeatability of the response of our nanogap IDEs towards a 1000 ppm signal was already shown in Figure 10. The decaying baseline, visible in Figure A, can be subtracted from these data, to prove that the response is equally high for every peak. **Figure 12** shows the results for repeated 100 ppm acetone peaks. We find a response of 1.2 pF for every 100 ppm peak.



**Figure 12.** Repeated 100 ppm acetone peaks detected by a reference sensor (top) and nanogap IDEs (bottom).

## 5. Conclusions

In summary, we have designed micro and nano IDEs capacitor structures featuring up to a 35 times improved sensitivity compared to microgap IDEs based on our previous work. Sensitivity could be further enhanced by increasing the area on which the nanogap IDEs structure was fabricated. The best performing nanogap IDEs, coated with PVPH containing nanoparticles, had a response time of several minutes. This type of nanogap IDEs could detect changes in acetone concentration down to 6 ppm. The sensor could be used multiple times, as proven by long term repeatability studies. (A detection limit of acetone as low as 6 ppm at room temperature has been demonstrated using these PVPH nanogap sensors.) Since the desired material is homogeneously coated in between the nano gaps, a robust electric field connection between these nano gaps can be assured to easily detect a very small amount of analyte. Our approach can also create addressable high-density nanogap electrodes in large scale by conventional micro-fabrication process. By simply changing the active layers into specific advanced materials such as non-conductive polymers or nano-composite, a new generation of nanogap devices is promising to detect a large range of analytes.

## References

- [1] V.P. Menon, C.R. Martin, Fabrication and Evaluation of Nanoelectrode Ensembles, *Anal. Chem.* 67 (1995) 1920–1928.
- [2] I. V Sapkov, E.S. Soldatov, Narrowing of nanogap for purpose of molecular single-electronics, in: 2013: p. 870000–870000–6.
- [3] D.R. Ward, F. Huser, F. Pauly, J.C. Cuevas, D. Natelson, Optical rectification and field enhancement in a plasmonic nanogap, *Nat Nano.* 5 (2010) 732–736.
- [4] S.-K. Kim, J.-Y. Son, Epitaxial ZnO thin films for the application of Ethanol gas sensor: Thickness and Al-doping effects, *Electrochem. Solid-State Lett.* 12 (2009) J17–J19.
- [5] M. Löhdorf, U. Schlecht, T.M.A. Gronewold, A. Malavé, M. Tewes, Microfabricated high-performance microwave impedance biosensors for detection of aptamer-protein interactions, *Appl. Phys. Lett.* 87 (2005) 1–3.
- [6] M.A. Reed, C. Zhou, C.J. Muller, T.P. Burgin, J.M. Tour, Conductance of a Molecular Junction, *Science* (80-. ). 278 (1997) 252 LP-254.
- [7] H. Park, J. Park, A.K.L. Lim, E.H. Anderson, A.P. Alivisatos, P.L. McEuen, Nanomechanical oscillations in a single-C60 transistor, *Nature.* 407 (2000) 57–60.
- [8] K. Liu, P. Avouris, J. Bucchignano, R. Martel, S. Sun, J. Michl, Simple fabrication scheme for sub-10 nm electrode gaps using electron-beam lithography, *Appl. Phys. Lett.* 80 (2002) 865–867.
- [9] H. Zhang, S.-W. Chung, C.A. Mirkin, Fabrication of Sub-50-nm Solid-State Nanostructures on the Basis of Dip-Pen Nanolithography, *Nano Lett.* 3 (2003) 43–45.
- [10] A.C. Whalley, M.L. Steigerwald, X. Guo, C. Nuckolls, Reversible Switching in Molecular Electronic Devices, *J. Am. Chem. Soc.* 129 (2007) 12590–12591.
- [11] X. Guo, A. Whalley, J.E. Klare, L. Huang, S. O'Brien, M. Steigerwald, C. Nuckolls, Single-Molecule Devices as Scaffolding for Multicomponent Nanostructure Assembly, *Nano Lett.* 7 (2007) 1119–1122.
- [12] C.P.R. Dockendorf, D. Poulikakos, G. Hwang, B.J. Nelson, C.P. Grigoropoulos, Maskless writing of a flexible nanoscale transistor with Au-contacted carbon nanotube electrodes, *Appl. Phys. Lett.* 91 (2007) 243118.
- [13] J. Tamaki, A. Miyaji, J. Niimi, Y. Nakataya, S. Konishi, Nano-gap Effects in Semiconductor Gas Sensors, *IEEE Trans. Sensors Micromachines.* 126 (2006) 573–577.
- [14] T. Chang, H. Jung, B. Jang, J. Lee, J.-S. Noh, W. Lee, Nanogaps controlled by liquid nitrogen freezing and the effects on hydrogen gas sensor performance, *Sensors Actuators A Phys.* 192 (2013) 140–144.
- [15] S. Mubeen, B. Yoo, N. V Myung, Fabrication of nanoelectrodes and nanojunction hydrogen sensor, *Appl. Phys. Lett.* 93 (2008) 133111.
- [16] B. Jang, K.Y. Lee, J.-S. Noh, W. Lee, Nanogap-based electrical hydrogen sensors fabricated from Pd-PMMA hybrid thin films, *Sensors Actuators B Chem.* 193 (2014) 530–535.
- [17] E. Menumorov, B.A. Marks, D.A. Dikin, F.X. Lee, R.D. Winslow, S. Guru, D. Sil, E. Borguet, P.

Hutapea, R.A. Hughes, S. Neretina, Sensing Hydrogen Gas from Atmospheric Pressure to a Hundred Parts per Million with Nanogaps Fabricated Using a Single-Step Bending Deformation, *ACS Sensors*. 1 (2016) 73–80.

- [18] F. Favier, Nanogaps for hydrogen sensing, *2012 IEEE Sensors*. (2012) 1–4.
- [19] E. Lee, J. Lee, J.-S. Noh, W. Kim, T. Lee, S. Maeng, W. Lee, Pd–Ni hydrogen sponge for highly sensitive nanogap-based hydrogen sensors, *Int. J. Hydrogen Energy*. 37 (2012) 14702–14706.
- [20] C. Shi, H. Qin, L. Li, Y. Chen, L. Ju, J. Hu, CO<sub>2</sub> sensing characteristics and mechanism for LaCoO<sub>3</sub> predicted by density function theory, *Appl. Surf. Sci.* 327 (2015) 168–173.
- [21] K. Muthukrishnan, M. Vanaraja, S. Boomadevi, R.K. Karn, V. Singh, P.K. Singh, K. Pandiyan, Studies on acetone sensing characteristics of ZnO thin film prepared by sol–gel dip coating, *J. Alloys Compd.* 673 (2016) 138–143.
- [22] F.S. Dias, L.G. Tartuci, H. de F. Gorgulho, W.S. Machado, Characterization of a carbon xerogel-based sensor for detection of acetone, ethanol, and methanol vapors, *Sensors Actuators B Chem.* 231 (2016) 440–449.
- [23] M. Kahali Moghaddam, A. Breede, A. Chaloupka, A. Bödecker, C. Habben, E.-M. Meyer, C. Brauner, W. Lang, Design, fabrication and embedding of microscale interdigital sensors for real-time cure monitoring during composite manufacturing, *Sensors Actuators A Phys.* 243 (2016) 123–133.
- [24] O. Laczka, E. Baldrich, F.X. Muñoz, F.J. del Campo, Detection of *Escherichia coli* and *Salmonella typhimurium* Using Interdigitated Microelectrode Capacitive Immunosensors: The Importance of Transducer Geometry, *Anal. Chem.* 80 (2008) 7239–7247.
- [25] H. Omran, K.N. Salama, Design and fabrication of capacitive interdigitated electrodes for smart gas sensors, *2015 IEEE 3rd Int. Conf. Smart Instrumentation, Meas. Appl.* (n.d.).
- [26] H. Xie, Q. Yang, X. Sun, J. Yang, Y. Huang, Gas sensor arrays based on polymer-carbon black to detect organic vapors at low concentration, *Sensors Actuators B Chem.* 113 (2006) 887–891.
- [27] Z. Ying, Y. Jiang, X. Du, G. Xie, J. Yu, H. Tai, Polymer coated sensor array based on quartz crystal microbalance for chemical agent analysis, *Eur. Polym. J.* 44 (2008) 1157–1164.
- [28] P. Oikonomou, G.P. Patsis, A. Botsialas, K. Manoli, D. Goustouridis, N.A. Pantazis, A. Kavadias, E. Valamontes, T. Ganetsos, M. Sanopoulou, I. Raptis, Performance simulation, realization and evaluation of capacitive sensor arrays for the real time detection of volatile organic compounds, *Microelectron. Eng.* 88 (2011) 2359–2363.
- [29] R. Igreja, C.J. Dias, Analytical evaluation of the interdigital electrodes capacitance for a multi-layered structure, *Sensors Actuators, A Phys.* 112 (2004) 291–301.
- [30] H. Hammer, Analytical model for comb-capacitance fringe fields, *J. Microelectromechanical Syst.* 19 (2010) 175–182.
- [31] S. Gevorgian, E. Carlsson, S. Rudner, L.-D. Wernlund, X. Wang, U. Helmersson, Modelling of thin-film HTS/ferroelectric interdigital capacitors, 1998.
- [32] R. Igreja, C.J. Dias, Extension to the analytical model of the interdigital electrodes capacitance for a multi-layered structure, *Sensors Actuators A Phys.* 172 (2011) 392–399.

- [33] Q. Nguyen Minh, A. Kuijk, S.P. Pujari, F. van de Bent, J. Baggerman, H.D. Tong, H. Zuilhof, C.J.M. van Rijn, Preparation and gas sensing properties of nanocomposite polymers on micro-Interdigitated electrodes for detection of volatile organic compounds at room temperature, *Sensors Actuators B Chem.* 252 (2017) 1098–1104.
- [34] N.G. Green, A. Ramos, H. Morgan, Numerical solution of the dielectrophoretic and travelling wave forces for interdigitated electrode arrays using the finite element method, *J. Electrostat.* 56 (2002) 235–254.
- [35] H.-W. Jung, Y.W. Chang, G. Lee, S. Cho, M.-J. Kang, J.-C. Pyun, A capacitive biosensor based on an interdigitated electrode with nanoislands, *Anal. Chim. Acta.* 844 (2014) 27–34.
- [36] R.B. Bird, *The Feynman lectures on physics*, Richard P. Feynman, Robert B. Leighton, and Matthew Sands, Addison-Wesley, Reading, Mass, Volume I, II (1964); Volume III (1965), *AIChE J.* 10 (1964) 794.
- [37] H. Jayatilleka, W.D. Sacher, J.K.S. Poon, Analytical Model and Fringing-Field Parasitics of Carrier-Depletion Silicon-on-Insulator Optical Modulation Diodes, *IEEE Photonics J.* 5 (2013) 2200211.



## Chapter 5



### Improving Detection Limit in Capacitive Sensors

#### **Abstract**

Accuracy in capacitive sensing is determined not only by the sensitivity of the capacitive sensing element but also by the physical measurement method used in the experiment. In this study, a highly sensitive measurement setup for capacitive sensing is presented and we show that the detection limit can be improved when a nanogap capacitive sensor is brought into close proximity with a custom-built capacitance interface at room temperature. We tested and compared the sensing response of various capacitive interdigitated electrodes (IDEs) structures, a micro IDE versus a nanogap IDE, using poly (4-vinyl phenol) as an acetone sensitive polymer layer according to our previous work. The nanogap IDEs exhibit an increase of the signal output by a factor of 12 compared to micro IDEs, while the percentage of change remained equal (0.2 % at 1000 ppm acetone). Furthermore, the developed setup was utilized for humidity sensing by using graphene oxide (GO) coated on nanogap IDEs as the sensing element. A thin GO layer on nanogap IDEs has been used as an example to investigate the sensing response of IDEs to humidity changes with sub-femto farad resolutions. It is shown that the GO layer responds with 1.1 pF capacitance change when the relative humidity is changed by 2 %. The observed results prove that the signal-to-noise ratio is significantly enhanced when an IDE with a larger total initial capacitance is employed. It is concluded that the detection limit of the system has been significantly improved when using a nanostructure design for IDEs as a capacitive gas sensor.

*This chapter has been published as:*

*"Improving the limits of detection in capacitive sensors systems."* Franc J.F. van der Bent, [Quyen Nguyen Minh](#), Hien D. Tong, and Cees J.M. van Rijn. *Measurement Science and Technology*, **2017**.

## 1. Introduction

Capacitive sensors have been often used for humidity detection [1] and sensing organic chemical vapours.[2,3] Semiconductor companies have developed several techniques for accurately measuring capacitance changes to control electrical circuits, for example, in the electronic tablet industry and also in the field of contactless capacitive level sensing. There are now state-of-the-art signal processing front-end semiconductor chips that are able to measure in the fF range. However, a major disadvantage with most of these signal interfaces is that they do not have the capability to accurately record fF changes of a bare nF to pF capacitance, which is defined as the overall value of the capacitor including parasitic capacitances. The change of the overall capacitance, or  $\Delta C$ , is defined as the changing capacitance fraction. And for various capacitive sensing applications at very low concentrations, especially in the medical field, the  $\Delta C$  induced by the presence of targeted analytes is a very small (fF) value. Thus, development of a capacitive sensing system able to accurately record a very small capacitance change is the desirable target and main aim of this work.

Capacitive sensing is based on a change of the dielectric permittivity due to the presence of the targeted analyte within the dielectric layer.[4,5,6] The capacitive change caused by the analyte usually can be detected in a broad range, for example, 0.483 pF/ %RH [5] with respect to humidity changes, or 45 pF/ $\mu$ L with chloroform[6] and they are always relative to the bare IDE capacitance. The conventional 3D-geometry capacitor constructed by two conducting plates with a dielectric layer in between has not been of interest in capacitive sensing at low concentration of analyte for two reasons. Firstly, the dielectric materials needed for the detection of analyte must be deposited between two plates, which requires a complicated process, especially when the distance between the plates is at nanoscale. Secondly, the diffusion of analytes into the dielectric layer between the plates can only occur from their sidewalls, which results in a significant slow adsorption and diffusion before equilibrium is reached. Therefore a two-

dimensional structure designed by interdigitated electrodes (IDEs) on a silicon or glass platform is widely employed as a capacitor with co-planar electrodes. Detailed calculations for the determination of bare IDEs capacitance have been presented elsewhere.[4,7,8] Nevertheless, optimisation by enlarging the capacitance within the boundary of the detection area on the IDEs using nanostructure may greatly improve the bare IDE capacitance.

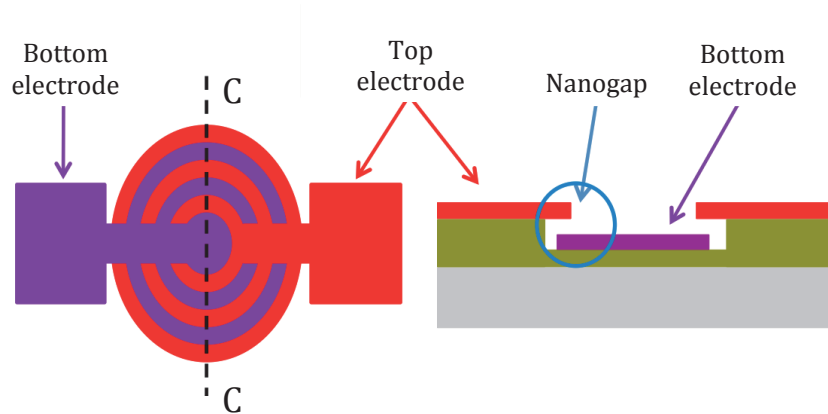
We utilized several strategies to increase the limit of detection in capacitive sensing. We first propose a facile approach to fabricate a nanogap interdigitated capacitor (so-called nanogap IDEs) that has a relatively large capacitance for being used as capacitive sensing element. When the bare capacitance of the used sensing element is increased,  $\Delta C$  also increases and resulting in a larger signal. With this enlargement, the signal-to-noise ratio (S/N) is improved with respect to signal power levels and to the noise added by the measurement system. However,  $\Delta C$  needs to be a factor higher than the parasitic contribution so that it can be measureable. Thus, a second approach to improve the sensitivity of the measurement unit is to minimize parasitic capacitances of the measurement setup. Special attention is paid to optimize cabling thermal and mechanical stability of the measurement setup itself. These components could introduce large changes in parasitic capacitance values. The third approach to enhance the sensitivity is the improvement of the measurement's resolution caused by using proper electronics interfaces, which will be described in detail.

## **2. Materials and Methods**

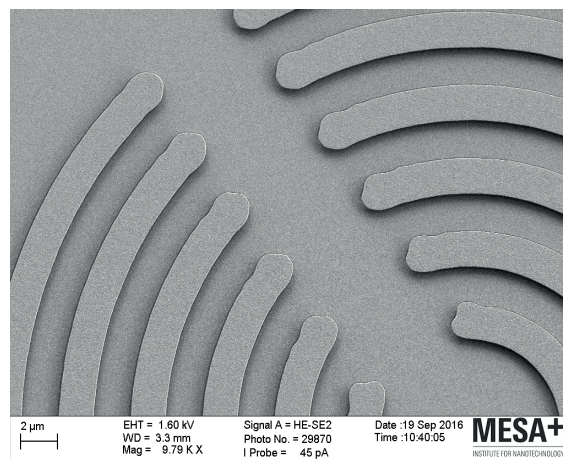
### **2.1. Fabrication of Nanogap IDEs**

An overview and a cross section of the nanogap interdigitated capacitor are shown in **Figure 1** and its SEM image of ring structure electrodes in **Figure 2**. Here, the capacitor has a patterned area of 0.25 mm × 0.25 mm, consisting of 60 top finger electrodes and 60 bottom finger electrodes. Each finger electrode has its width and pitch of 2  $\mu\text{m}$  and 4  $\mu\text{m}$ , respectively. A distance (the gap) from top to bottom

electrodes is determined by an etching depth of the sacrificial  $\text{SiO}_2$  layer and the thickness of bottom electrodes. (See Chapter 4, section 2.2)



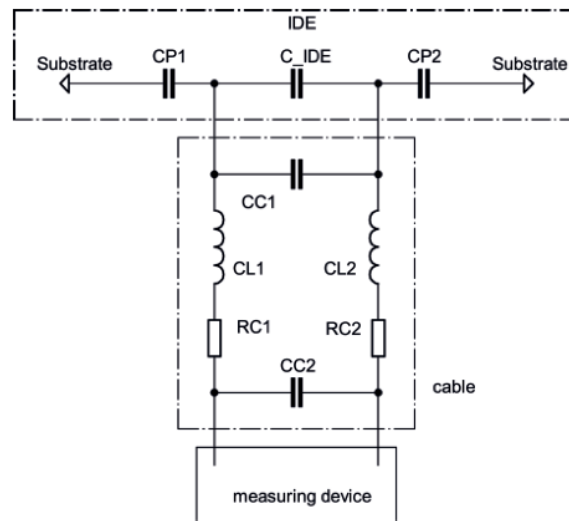
**Figure 1.** A top-view image of the nanogap-IDEs (left side) and a cross-sectional image (over C-C) of one bottom electrode and its two adjacent top electrodes, showing the nanogap capacitor (right side).



**Figure 2.** An overview SEM image of ring structure electrodes of the nanogap IDEs capacitor on a silicon platform.

## 2.2. Experimental Setup

As designed, the nanogap IDEs have a gap at nano-scale, yielding a relatively high capacitance, and therefore provides thus a high front-end gain. For instance, if the  $\Delta C$  can be brought into the 10 to 100 pF range, the cable interference will be negligible. On the other hand, if the  $\Delta C$  is within the range of 10-1000 fF, changes in parasitic cable capacitance can be problematic. In our work, acetone measurements were performed with a 160 pF bare nanoscale IDE capacitance. Also, nanogap IDEs with a bare capacitance of 30-50 pF were fabricated and coated with graphene oxide for humidity measurements.[9, 10]



**Figure 3.** Simplified schematic of resistance, capacitance and inductance circuit components during measurements.

**Figure 3** shows a simplified model of the structure connected to a measurement device using a cable. The IDE capacitor is formed by the  $C_{IDE}$ , and both parasitic capacitors  $CP1$  and  $CP2$  have a capacitance towards the substrate. The cable needed

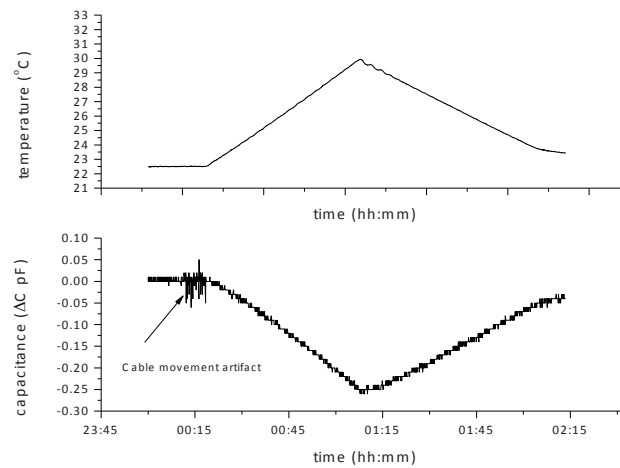
to connect the IDEs to the measuring device consists of a network of resistors, inductors and capacitors. [11] This cabling connection is a fundamental limitation of the  $\Delta C$  measurement due to temperature variations,[12] as shown in the experimental setup. Reducing the cable length to zero can herewith increase the limits of detection and lead to development of a custom-built capacitance interface.

Since the parasitic capacitances of series CP1 and CP2 are stable over time, they can be added as a constant to the bare value of IDEs capacitance. Thus, the total bare IDE capacitance, presented in Figure 1, is equivalent to a circuit consisting of:

$$C_{\text{total}} = C_{\text{IDEs}} + ((CP1 * CP2) / (CP1 + CP2)) + C_{\text{cable}}$$

### 2.3. Parasitic Capacitance of Cabling

When a capacitive experiment is in progress, the capacitance of connection cables can easily fluctuate up to 100 fF when the cable is moved (see **Figure 4**), this is consistent with many other findings.[12,13] When the cable is stable during the measurement, other fluctuations may occur, e.g., the temperature of the measured ambient.



**Figure 4.** Temperature dependence of one meter RG58.

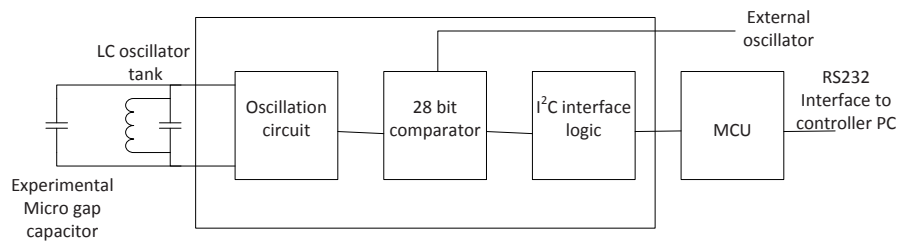
In Figure 4, the capacitance change of a standard, 1 meter RG58 with 50  $\Omega$  cable towards a temperature change of 8  $^{\circ}\text{C}$  measured with a calibrated HP4192A impedance analyser after a warm-up period of 1 hour at 100 kHz. The added capacitance to the sensor from this type of cable is approximately 100 pF/m,[11] and was measured together with the measurement clamp and BNC connector at 126 pF. The limit of detection of the measurement device is then determined by the parasitic noise of the cable as a result of mechanical stress, and the response of the cabling due to temperature fluctuations in the surrounding environment. The ground noise with the resolution of the HP4192A, derived from the data in Figure 4, is determined at approximately 20 fF. The sensitivity to temperature changes is calculated to be about 31.25 fF/ $^{\circ}\text{C}$  for one meter of cabling, defining the maximum resolution of the single-ended measurement. Therefore, we propose another method to improve the detection limit in order to overcome these above-mentioned fundamental limitations in the coming section.

The response to temperature changes caused by the resonance circuit components is considered in the system although it is quite small due to the stability properties of the measurement system. If the temperature-dependence of a sensor is to be recorded, a compensation method is then needed. Further improvements of this system may involve a differential measurement approach. In this case a second sensor may be added to the front end that is passivated for sensing analytes but responds to humidity and/or temperature changes at the same level as the active sensor itself. By subtracting both signals using digital signal processing, variations caused by temperature or humidity can be minimized.

## **2.4. Improving the detection limit**

**Figure 5** shows the flowchart of the capacitance readout interface, which was designed to overcome the issue with cable interference (See Appendix D for detailed information on this interface). The heart of the interface is the FDC-2212

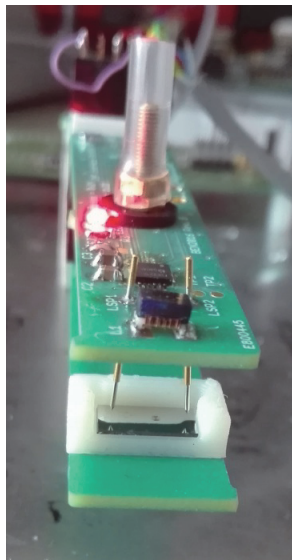
semiconductor from Texas Instruments [14] with a 168 dB dynamic range comparator resulting in a resolution of 0.3 fF/bit. This semiconductor is capable of handling capacitors up to 250 nF; therefore it is suitable for measurements of nanostructure IDEs with a large range capacitance (20 - 200 pF).



**Figure 5.** Capacitance interface flowchart.

A custom printed circuit board was designed to interconnect the circuits and herewith stabilise the parasitic capacitance to a steady value. The double-sided metalized printed circuit board is made of standard FR4 material with gold plated to form the electrical contacts. The collected data and their settings are managed by an ARM7 MCU that interfaces to the IDEs using the I2C protocol. The controller PC in Figure 5 collects the data from the MCU using the RS232 protocol through an USB cable. The FDC2212 is configured to handle an external crystal oscillator of 33 MHz/1ppm that was placed outside the chamber to minimize the temperature variations of the reference.



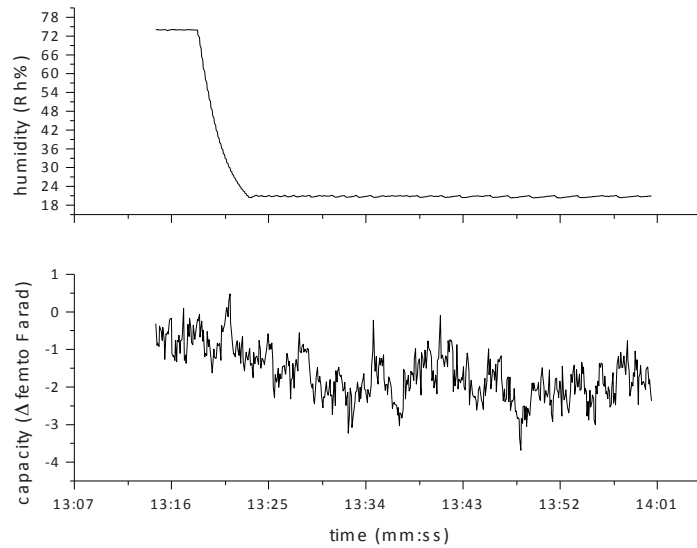


**Figure 6.** Capacitance interface, front view with nanogap IDEs and pogo pins.

In order to verify the response of the system to humidity changes, the capacitance interface was placed in the signal measurement system without the nanogap IDEs (**Figure 6**). As shown in **Figure 7**, the humidity changes between 20 and 75 %RH according to a pattern of the pre-defined script when the temperature is set at  $25 \pm 0.06$  °C. The data collected by the computer controller was then analysed using Microsoft Excel and  $\Delta C$  was calculated and plotted as in Figure 4. The data shows a maximum variation of 3 fF, this will be set as the ground noise of the system. After determining the ground noise of the system (Figure 7), the nanogap IDE is connected in a parallel circuit to the oscillation tank as shown in Figure 5. At this time the tank frequency is at higher value compared to other research at 10 kHz.[15] The capacitor used to stabilise the tank has a value of 33 pF incorporated with an added parallel parasitic capacitance (23 pF) caused by the printed circuit board routing and the pogo pins while the inductor of the tank is a high-frequency inductor (18  $\mu$ H). The frequency of the tank is then determined by equation (1):

$$F_{res} = \frac{1}{2 * \pi * \sqrt{(L * C)}} \quad (1)$$

Where L is the inductance in Henry, C is the capacitance in Farads and  $F_{res}$  is the tank resonance frequency in Hz. At 18  $\mu$ H and 56 pF, the tank's resonance frequency is 5 MHz. When a nanogap IDE (for example, with GO layer) is placed in the tank circuit, the capacitance increases, thereby decrement of the resonance frequency of the tank occurs.



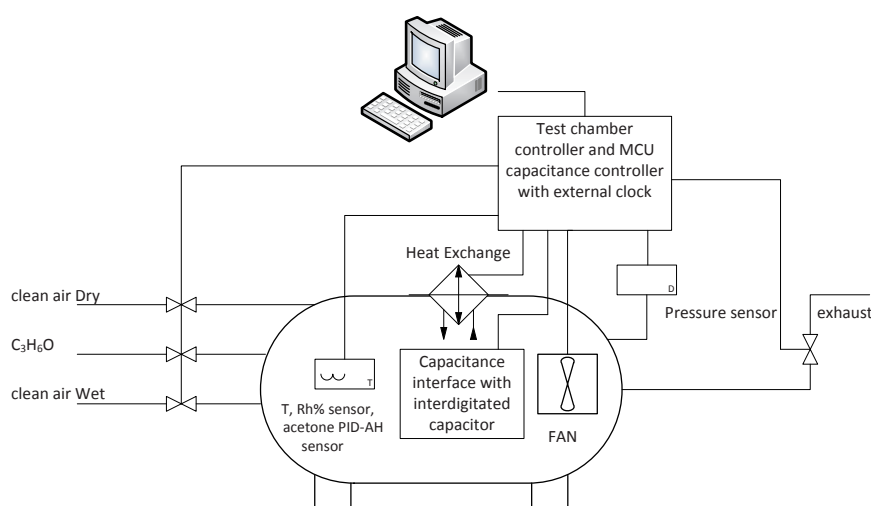
**Figure 7.** Capacitance interface response to humidity change of 50 %RH with an open circuit without IDES, resulting in a 3 fF noise level.

### 3. Results and Discussion

#### 3.1. PVPH Micro and Nanogap IDEs

In this experiment, a highly selective polymer layer with a relative low dielectric change is used on both a micro and nanogap IDE to improve the device's detection

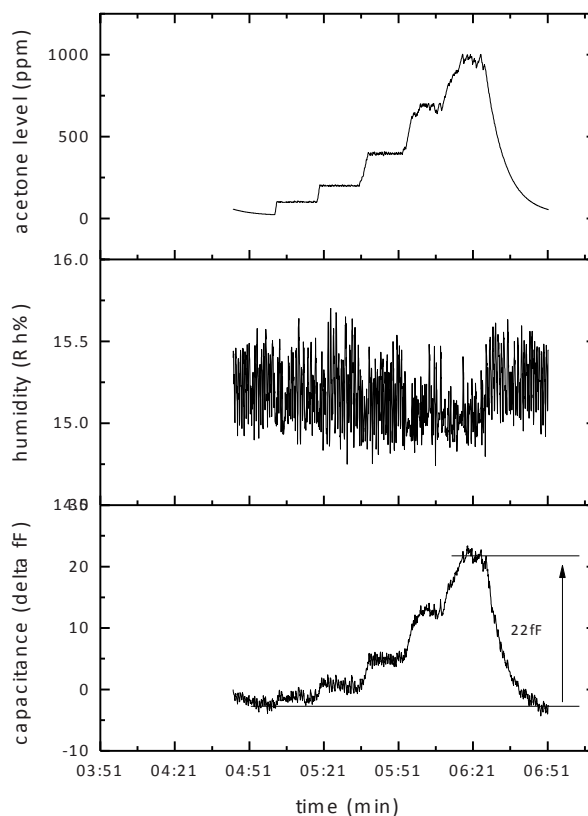
limit with respect to capacitance change. In order to control the amount of acetone vapour in the measurement system, the standard system was then upgraded to enable these tests. An acetone inlet, which is controlled by a high-speed valve, indicated in **Figure 8**, was used from a calibrated gas cylinder with an acetone concentration of 1000 ppm. The vapour concentration in the system was measured using a calibrated PID-AH sensor as a reference sensor from Alphasense® with detection range of acetone is of 0-1000 ppm. The output of this sensor was fed into a calibrated DMM to be digitated by the control PC. The data from this reference sensor was used in a software feedback loop of the signal measurement system. The script file, necessary for setting values in the system, was enhanced with a line describing the desired concentration of acetone in ppb.



**Figure 8.** Setup of the measurement system for acetone.

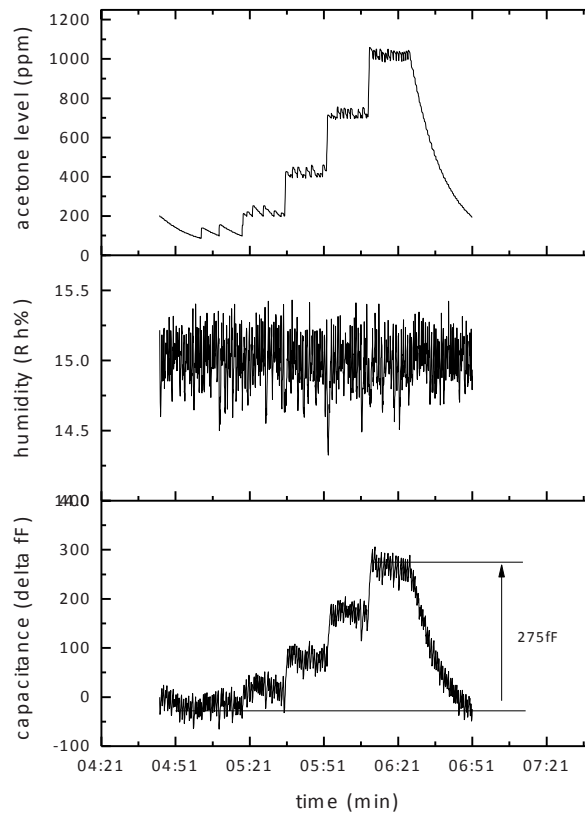
Two identical micro IDEs were prepared with a PVPH polymer layer in order to perform measurement of acetone detection at concentrations of up to 1000 ppm. Together with these micro IDEs, a total bare IDE capacitance of 8.1 pF was measured as reference signal. **Figure 9** shows the sensing response of micro IDEs to

an acetone input in increments of 100-200-400-700-1000 ppm over a total time interval of 2 hours. Here, we observed a response according to the acetone inputs and another response to fluctuations in the humidity set at 15.2 %RH since the polymer is also sensitive to humidity changes. The temperature was kept stable at  $25 \pm 0.1$  °C during all measurements. The peak value of these micro IDEs at 1000 ppm acetone is 22 fF while the response to humidity changes of 0.5 %RH does not exceed 2.5 fF.



**Figure 9.** Response of the 8 pF micro IDEs with 10 % PVPH polymer to acetone input.

To improve the dynamic range of the measurement, or sensor output, the same experiment was conducted using a nanogap IDE. Because of the increased density of the electrodes, the capacitance increased to 135 pF while PVPH is used as a dielectric sensing layer. The same script pattern used for the experiment as in Figure 9 was also executed at the same humidity and temperature.



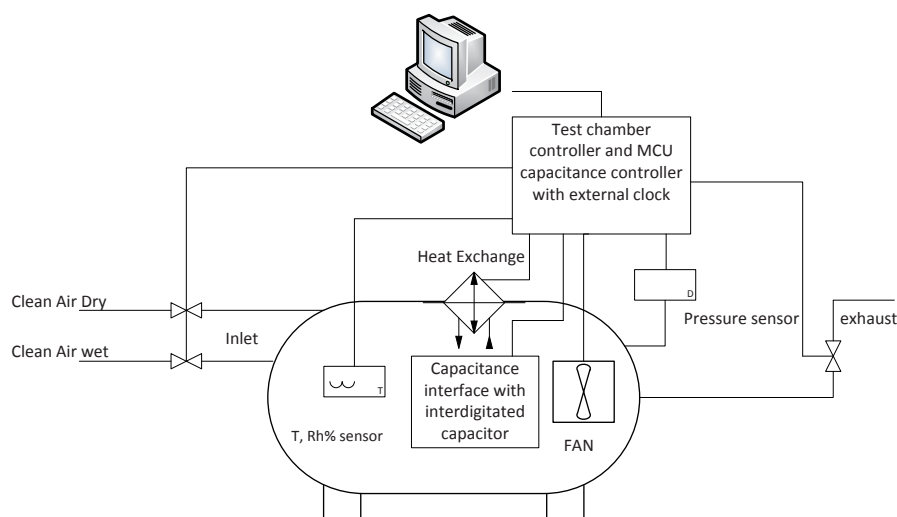
**Figure 10.** Response of a 135 pF nanogap IDE coated with 10 % PVPH polymer to acetone inputs.

**Figure 10** shows the response of the nanogap IDE to variations of acetone vapour. Although the response of this sensor to acetone inputs and observed fluctuation in humidity change is similar to those when measuring micro IDEs, the signal amplitude increased by a factor of 12 compared to that in the case of using micro IDEs. The value of  $\Delta C$  is 275 fF at 1000 ppm acetone while the dynamic range of the capacitance interface was maintained. Both IDE types (micro and nano structure) showed a 0.2 % change of the capacitance in response to 1000 ppm of acetone. The micro IDEs gave a significant response in  $\Delta C$  with value of 22 fF (on a 8 pF bare capacitance) while the nanogap IDEs showed a response in  $\Delta C$  with value of 275 fF (on a 135 pF bare capacitance) to 1000 ppm acetone.

### 3.2. Graphene Oxide IDEs (36 pF capacitance)

Recent developments in advanced semiconducting technology have brought up many great possibilities to measure capacitance changes in the femto-farad range. Some of them have shown the sensing response of graphene oxide and is based on the change of the dielectric properties of the sensing layer as it ad/absorbs water vapour, the non-linear behaviour corresponds with current findings,[15-17] although the central frequency of 3.1 MHz used in these experiments is higher by a factor of 300 than that reported by Bi *et al.* in 2013, see also **Figure 13**. An experimental setup was constructed to study sensing behaviours of the nanogap IDE in a clean air atmosphere. The measurement system is shown in **Figure 11**. Measured with a calibrated thermal conductive AHT-200-01 humidity sensor from Ohmic Industries, the humidity in an 8.3-litter chamber is controlled by a PC with high-speed inlets and exhaust valves by passing a bubbler. This sensor can survive in an environment with volatile chemicals such as ketones and alcohols. The humidity sensor was chosen to withstand in an acetone environment, as used in the previous experiment, and without deterioration over time. The detection principle of most commercially available humidity sensors is based on their polymeric sensing layer. This type of sensor is available in factory-calibrated versions with

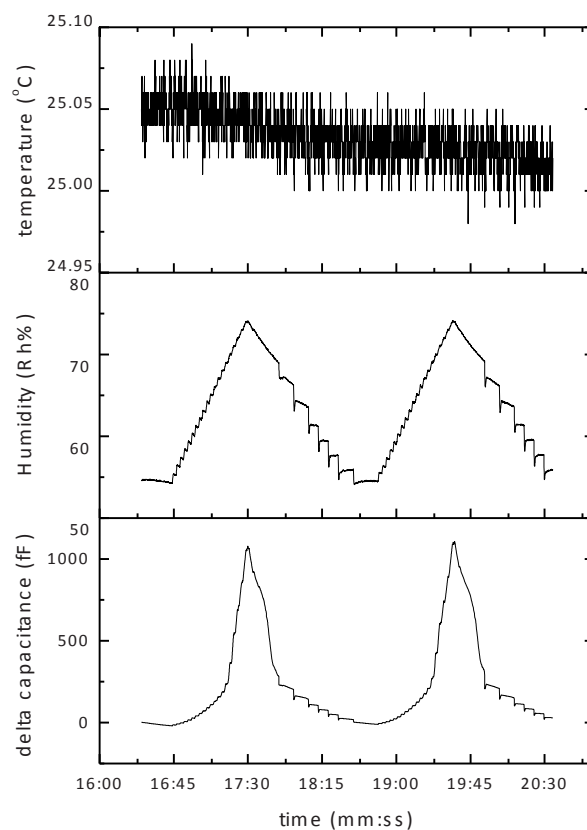
good precision ( $> 0.5\% \text{RH}$ ) and is equipped with a digital interface for easy readout. A drawback of this sensor type is that it requires temperature compensation of the output data. The temperature in the chamber in this set up is regulated with a Peltier element, a heat sink and a fan. Overpressure is also controlled with an exhaust valve regulated by a pressure transducer. When the internal pressure exceeds ambient levels the exhaust valve opens until the pressure reaches ambient conditions.



**Figure 11.** Setup of the signal measurement system for graphene oxide.

GO was deposited on the sensing area of the IDEs by drop casting (20 mg of GO was dissolved in 20 ml purified water and stirred for 3 hours at  $25\text{ }^{\circ}\text{C}$ ). Three layers of GO were deposited subsequently and each layer was dried in vacuum at  $50\text{ }^{\circ}\text{C}$  for 60 minutes. The bare IDE capacitance of a nanogap IDEs was  $36\text{ pF}$  with  $>20\text{ M}\Omega$  resistance measured with a calibrated Keithley 2000 DMM. After depositing the GO layer, the resistance was measured again at  $2.15\text{ M}\Omega$ . The prepared experimental nanogap IDEs were placed in the capacitance interface that connects to the tank

circuit using two 0.8 mm spear tip pogo pins, as shown in Figure 6. After the nanogap IDE is loaded into the interface, the oscillator tank frequency is determined by the inductor and a parallel circuit of the capacitor placed on the capacitance interface, the nanogap sensor used GO as dielectric environment.



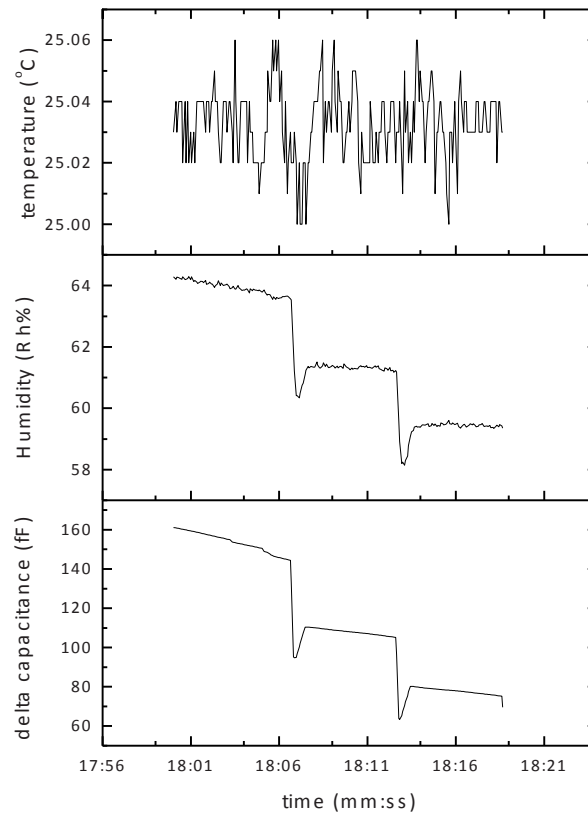
**Figure 12.** Humidity and temperature response of the GO prepared nanogap sensor.

After GO was deposited on the nanogap sensor the capacitance increased to 90 pF measured in air at 25 °C with an ambient relative humidity of 53 %RH. The value of



the nanogap IDEs capacitance was measured with a calibrated Agilent 4262A LRC meter at 10 kHz. The resonance frequency is determined by the parallel combined capacitance of the interface (56 pF) and GO IDEs (90 pF) and is approximately 3.1 MHz. This was verified by measurement with a Tektronix TDS2002 sensor. After the IDEs and capacitance interface were placed into the chamber, a triangular humidity change from 55 to 74 %RH was programmed (**Figure 12**, middle graph) while the signal measurement system temperature was kept at  $25 \pm 0.06$ . Figure 12, bottom graph shows the sensing response of the nanogap IDEs with GO layer in fF to humidity change. A total measured span of approximately 1100 fF is then observed. The observed resolution of the interface is given in Figure 10, showing a detail of Figure 12 starting at 18:00.

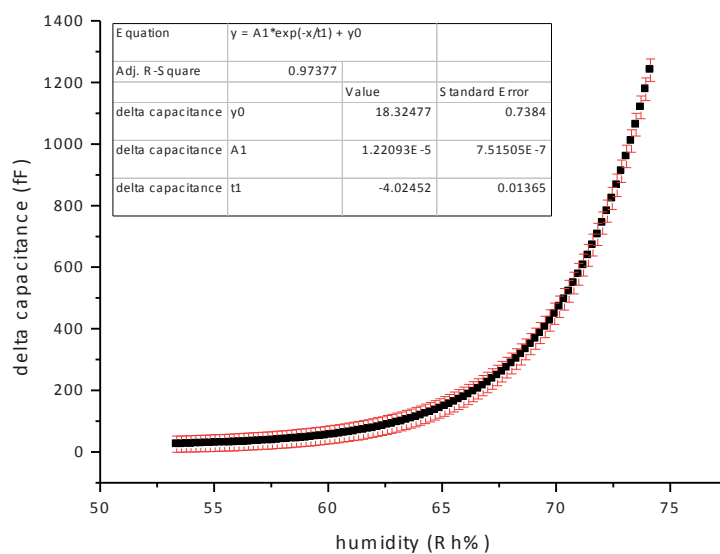
As shown in **Figure 13**, the response of the GO to humidity as a dielectric material is non-linear. This effect was further explored by a nine-fold repetition of the above-described experiment. The results from these measurements are shown in **Figure 14**, where the measured humidity of the reference plotted versus  $\Delta C$ . Figure 14 also presents the data, which is fitted to an exponential function including error bars, indicating a 0.97 standard deviation.



**Figure 13.** High-resolution detail of the measured capacitance (shown previously in Figure 12).

The GO measurement shows sensing responses of the coating material of 1.2 pF within the proposed humidity change. When the dielectric change of the sensing layer becomes smaller and the signal-to-noise ratio becomes insignificant, the detection limit of the measured capacitance interface will also reach the limit of the hardware. To summarise, the data in this experiment showed a bare IDE

capacitance between 3 pF and 10 nF with pF resolution and these measurements were performed with a comparable capacitance, while the limit of detection presented here is smaller by a factor of 1000, in the fF range. Reproducibility of all measurements is assured. Furthermore, the limit of detection has improved, enabling the use of comparatively small detection areas. The response time of the GO sample is in the same range as the reference humidity sensor. A change of 100 fF is observed as a result of a humidity change in 3 %RH. The response of the nanogap sensors is exponential and reproducibility of measurement excels also at both low and high regions. Calibration of the sensor is possible when using exponential fitting with a standard deviation of 0.97.



**Figure 14.** Fitted exponential behaviour of the graphene oxide layer with error bars.

#### 4. Conclusions

When the features of IDEs are reduced from micro to nano scale, the bare IDE capacitance increases and so does  $\Delta C$ . Thus, a larger dynamic range of the capacitance measurement device can be applied; therefore, the signal-to-noise ratio can be drastically improved. Furthermore, to minimize the change of parasitic capacitance of cabling due to temperature changes and other cabling system connections, the measurement is suggested to be carried out as close to the IDE as possible. The detection limit in capacitive IDE sensors at room temperature depends on the thermal and mechanical stability of the cabling and the resolution of the measurement system. Sensing measurements can be conducted at femto farad level with high resolution (0.3 fF) while reproducibility is maintained. Using this method, the ground noise was measured at 3 fF with 0.3 fF resolutions, with a 100 pF IDE capacitance comprising the GO sensing layer. When the IDE feature size is reduced to nanoscale, the device's capacitance and corresponding signal amplitude are significantly enhanced. The improved capacitance measurement system in combination with nanostructure of the high-density IDEs resulted in a 12-fold improvement of the detection limit.

## References

- [1] M.C. Zaretsky, J.R. Melcher, C.M. Cooke, Moisture sensing in transformer oil using thin film microdielectrometry, *Electrical Insulation*, 1988, Conference Record of the 1988 IEEE International Symposium on 1988, pp. 12-7.
- [2] C. Hagleitner, A. Hierlemann, D. Lange, A. Kummer, N. Kerness, O. Brand, et al., Smart single-chip gas sensor microsystem, *Nature*, 414(2001) 293-6.
- [3] R. Zhou, A. Hierlemann, U. Weimar, W. Göpel, Gravimetric, dielectric and calorimetric methods for the detection of organic solvent vapours using poly(ether urethane) coatings, *Sensors and Actuators B: Chemical*, 34(1996) 356-60.
- [4] R. Igreja, C.J. Dias, Analytical evaluation of the interdigital electrodes capacitance for a multi-layered structure, *Sensors and Actuators A: Physical*, 112(2004) 291-301.
- [5] Y. Kim, B. Jung, H. Lee, H. Kim, K. Lee, H. Park, Capacitive humidity sensor design based on anodic aluminum oxide, *Sensors and Actuators B: Chemical*, 141(2009) 441-6.
- [6] F.A. Harraz, A.A. Ismail, H. Bouzid, S.A. Al-Sayari, A. Al-Hajry, M.S. Al-Assiri, A capacitive chemical sensor based on porous silicon for detection of polar and non-polar organic solvents, *Applied Surface Science*, 307(2014) 704-11.
- [7] G.D. Alley, Interdigital Capacitors and Their Application to Lumped-Element Microwave Integrated Circuits, *IEEE Transactions on Microwave Theory and Techniques*, 18(1970) 1028-33.
- [8] J.L. Hobdell, Optimization of Interdigital Capacitors, *IEEE Transactions on Microwave Theory and Techniques*, 27(1979) 788-91.
- [9] J. Wang, J. Jiu, M. Nogi, T. Sugahara, S. Nagao, H. Koga, et al., A highly sensitive and flexible pressure sensor with electrodes and elastomeric interlayer containing silver nanowires, *Nanoscale*, 7(2015) 2926-32.
- [10] J.F. van der Bent, E. Puik, H.D. Tong, C.J.M. van Rijn, Temperature balanced hydrogen sensor system with coupled palladium nanowires, *Sensors and Actuators A: Physical*, 226(2015) 98-106.
- [11] P. Horowitz, W. Hill, *The art of electronics*, [England]: Cambridge University Press; 2015.
- [12] S.X. Yang, W.Q. Yang, A portable stray-immune capacitance meter, *Review of Scientific Instruments*, 73(2002) 1958-61.
- [13] H. Scharfetter, P. Hartinger, H. Hinghofer-Szalkay, H. Hutten, A model of artefacts produced by stray capacitance during whole body or segmental bioimpedance spectroscopy, *Physiological Measurement*, 19(1998) 247.
- [14] Texas\_instruments, FDC2x1x EMI-Resistant 28-Bit, 12-Bit Capacitance-to-Digital Converter for Proximity and Level Sensing Applications, 2015, p. 60.
- [15] H. Bi, K. Yin, X. Xie, J. Ji, S. Wan, L. Sun, et al., Ultrahigh humidity sensitivity of graphene oxide, *Scientific Reports*, 3(2013) 2714.

- [16] B. Collignon, P. Hoang, S. Picaud, J. Rayez, Ab initio study of the water adsorption on hydroxylated graphite surfaces, *Chemical physics letters*, 406(2005) 430-5.
- [17] Y. Yao, X. Chen, H. Guo, Z. Wu, X. Li, Humidity sensing behaviors of graphene oxide-silicon bi-layer flexible structure, *Sensors and Actuators B: Chemical*, 161(2012) 1053-8.

## Chapter 6

### General Discussion



This chapter gives a brief overview of the most striking achievements as presented in this thesis. In particular, acetone sensors based on Si NW-FET and IDE structures will be discussed. Their sensing materials, sensing performance in different conditions and stability of devices will be reviewed for various approaches in real-life applications. Furthermore, we will focus on some preparation methods and highlight the results obtained for specific sensing behaviors to achieve targeted acetone level detected below ppm level, for instance, the optimal design of nanogap IDEs. Remaining questions, additional ideas, and recommendations will also be addressed for further research.

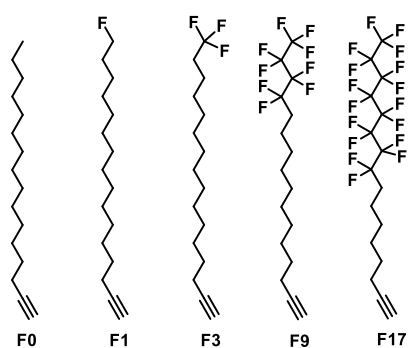
## 1. Remarks and future work

Here we discuss in more detail the possible areas of applications as well as approaches of use for gas sensors and their classification across requirements of VOCs detection at sub-ppm level. It is essential to produce gas sensors at a high quality including good sensitivity, high selectivity toward typical gases, and reproducibility with a fast response (e.g. within a minute) and long-term storage.

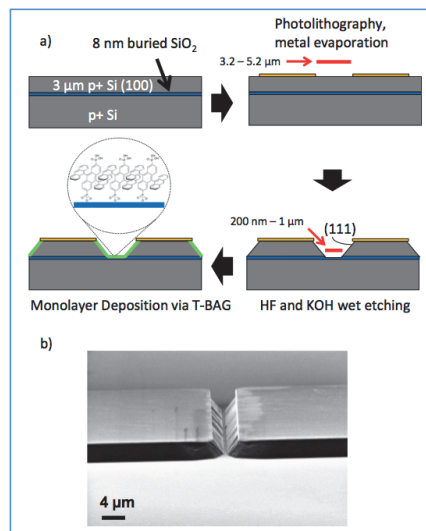
As presented previously in Chapter 2, we have succeeded in the formation of stable fluorinated monolayers on Si NWs, which enhanced sensing properties of FET devices towards VOCs detection with 2-octanone as a primary target. Fluorinated monolayers could be formed chemically stable and with a high density; also, their predicted physical structures were discussed. As a single channel in FET system, Si NWs can be effectively functionalized. Hydrosilylation of 1-alkynes was used to yield highly uniform fluorinated alkyne-derived Si-C≡C linked monolayers on all facets of the persistently oxide-free NWs. The obtained monolayers on Si NWs display superhydrophobic behavior, a high stability under both acidic and basic conditions and under extreme condition (UV irradiation, 254 nm). The monolayer coating provides excellent electrical passivation and displays significant potential in the use of single-channel FETs. Furthermore, this type of fluorinated monolayers can be altered when using different number of fluorine atoms with same carbon chain C16 (**Figure 1**). This results in monolayers on Si NWs with different surface energy. This means that the interaction between monolayers and analytes can be addressed in a specific manner with respect to detecting volatile compounds. Simply, to sense an analyte, we can choose the most effective monolayer based on its number of fluorine atoms. This approach also creates potential in the detection of many other types of VOCs based on their polarity of functional groups such as alcohols, ketones, aldehydes and acids. Surface functionalization with fluorinated monolayers could also be further applied in different structures, for example, a nanogap organic field-effect transistor (OFET). Pfaehler *et al.* [1] has proposed planar highly doped silicon nanogap electrode devices, functionalized with organic monolayers using tethering by aggregation and growth (T-BAG) method (**Figure 2**). With a nanogap structure and using the above-mentioned



fluorinated monolayers, the sensing performance of FETs could be enhanced since the conductivity of the modified nanogap is greatly improved. Therefore, we are confident that if a different coating with low-surface energy were used, similar results would be obtained with their structures as well. The application of these functional monolayers with high density and same chain length is greatly useful and enhances sensitivity of biosensors and/or gas sensors.



**Figure 1.** Fluoro-hydro alkynes employed in monolayer formation.[2]

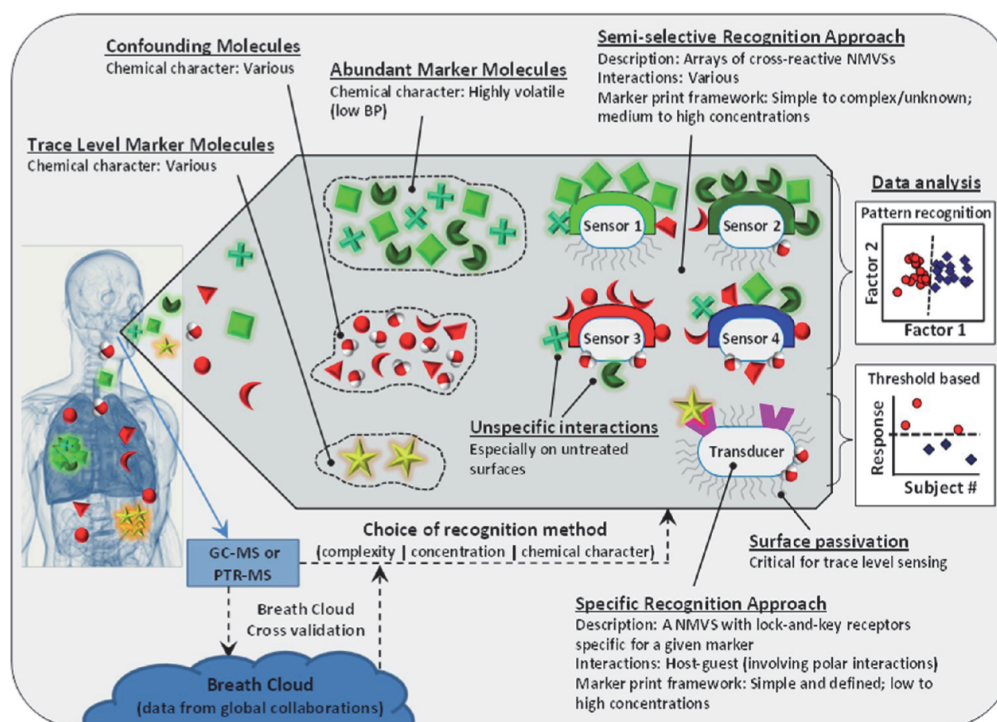


**Figure 2.** Schematic of a fabrication process of nanogap electrodes using as OFET. Here, a typical spacing between two metal pads is 3-5  $\mu\text{m}$ . Subsequent anisotropic etching resulted in nanogap structures with triangular-shaped cross-section, and a monolayer is grown in the gap via the T-BAG process – (A). SEM image of a finished nanogap structure (at an angle of 80°) – (B).[1]

The efficiency of electrical detection of bio-molecular interactions in nanogap or single channel of FET would drastically increase. When the proof of principle was achieved, together with pattern recognition structured with arrays of sensor units, these (bio-)/gas sensors with organic surface modification are promising candidates for a new generation of devices using e-nose concept for determining the corresponding biomarkers in human exhalation for medical diagnosis (**Figure 3**).

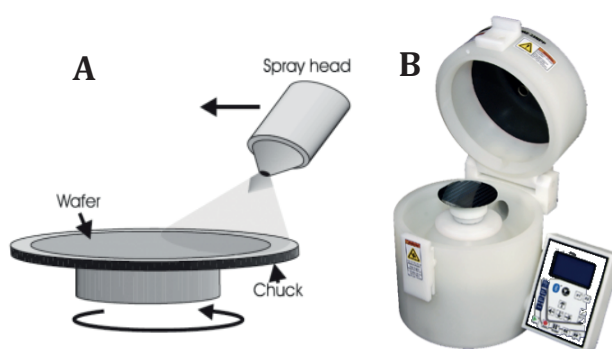
Possessing an easy-to-handle and quick response device to detect chemical analytes is essential for air quality monitoring in laboratories and industrial process, etc. to save lives and protect human health. As described in Chapter 3, of all tested polymers for sensing materials, PVPH showed highest affinity towards acetone. A conventional method, spin coating, is a low-cost and scalable industrial fabrication to be used. Using this method, a

capacitive chemical sensor based on an M-IDE coated with a polymeric nanocomposite layer consisting of Si NPs and PVPH was successfully achieved. However, the sensitivity of this device could be further improved by using a different thin layer preparation method: spray coating, presented in **Figure 4**. This method shows excellent homogeneity of coated polymer layers on a surface, especially, with micro IDE on glass substrates, the thickness of PVPH layer could be well controlled. This resulted in an active layer that enhanced the adsorption as well as desorption of analyte (acetone). This could generate a faster response and higher sensitivity of gas sensors.



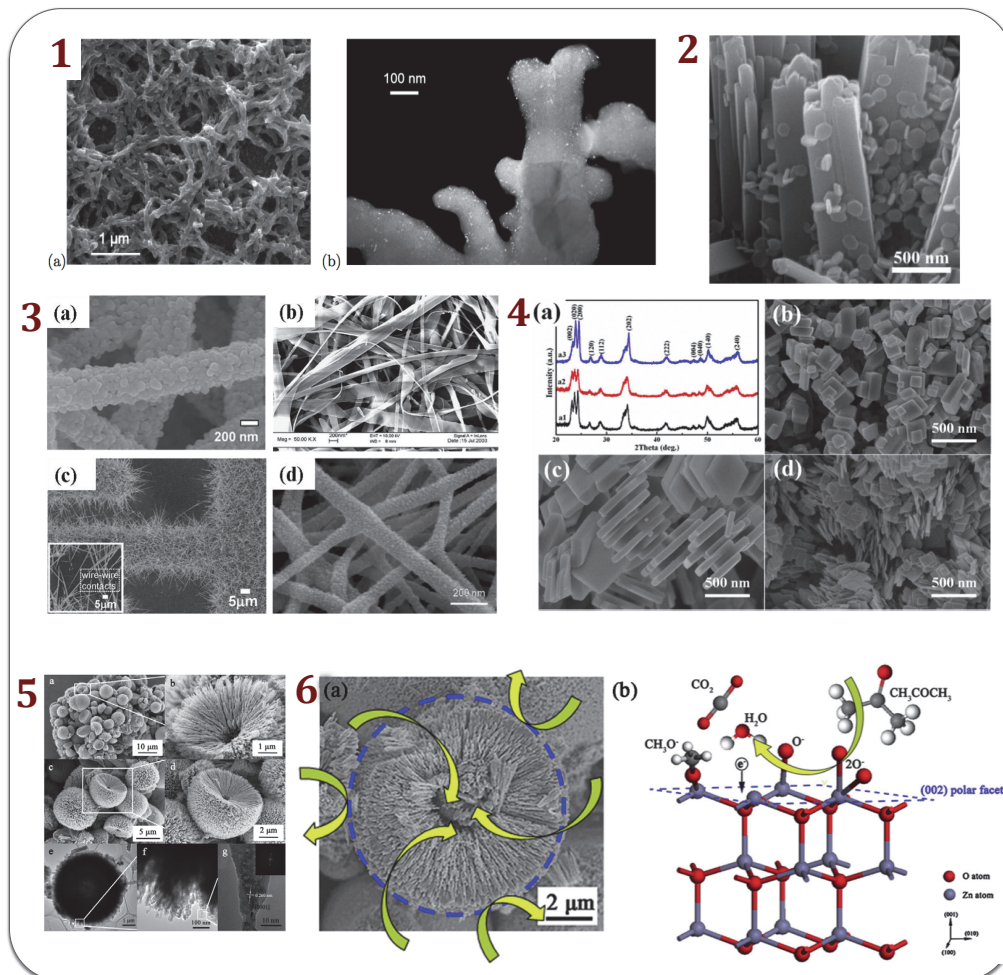
**Figure 3.** Schematic representation of the links between the different frameworks of breath marker-prints and the appropriate sensing approach (specific vs cross-reactive approach).[3]

As shown in this study, the addition of surface-modified Si nanoparticles led to an increase in polymer surface available for adsorption, which amplifies the response of the device towards acetone. The sensing response towards acetone at room temperature proved that the turn-on and -off exposure to this analyte was reversible with good reproducibility after multiple cycles of gas exposure. Moreover, the sensing response of the NC device remains stable during long-term storage in ambient atmosphere.



**Figure 4.** Spray coating can be applied for depositing polymer layer at larger scale for mass production of device during manufacturing process.

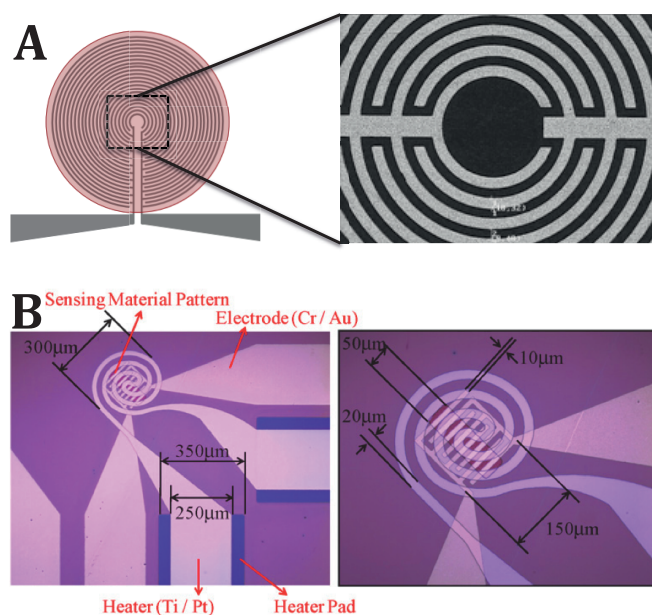
Nonetheless, detection of much lower concentrations of analyte should be further investigated for a more detailed examination of the sensor's sensitivity. Significant work regarding to the improvement of nanocomposite materials in gas sensors is required for advanced applications. The use of different types of nanostructures for acetone and other VOCs gas sensing is presented in **Figure 5**. Based on properties of nanostructure of both device's configuration and sensing materials, gas chemocapacitors could achieve excellent sensing performance towards numerous of analytes. However, to preserve the unique characteristics of chemocapacitive sensors, there are two requirements: these sensing materials need to be designed in such a way that the devices operate at room temperature, and there should be no dependency on external stimulus for sensor's response/recovery.



**Figure 5.** A variety of nanomaterials have been applied as sensing materials for the detection of acetone and other VOCs. Several examples are given: 1. a) SEM image of a PANi-TiO<sub>2</sub> nanocomposite after electropolymerization. b) TEM micrograph of PANi-TiO<sub>2</sub> in dark-field. TiO<sub>2</sub> nanoparticles are visible as white spot; 2 SEM image of NiO-decorated TiO<sub>2</sub> nanorods.[4]; 3 SEM images of (A) SnO<sub>2</sub> nanofibers produced by electrospinning.[5] (B) SnO<sub>2</sub> nanoribbons synthesized by direct oxidization. [6] (C) On-chip fabrication of SnO<sub>2</sub> nanowires grown on Au deposited Pt interdigitated electrodes by thermal evaporation.[7] (D) SnO<sub>2</sub>-ZnO hybrid nanofiber by electrospinning.[8]; 4 - SEM images of WO<sub>3</sub> cuboid for

acetone sensing.[9]; 5 - SEM images; of hierarchical ZnO spheres prepared; 6 - illustration of acetone sensing mechanism on ZnO spheres and (002) polar facets of hierachical ZnO sensor.[10]

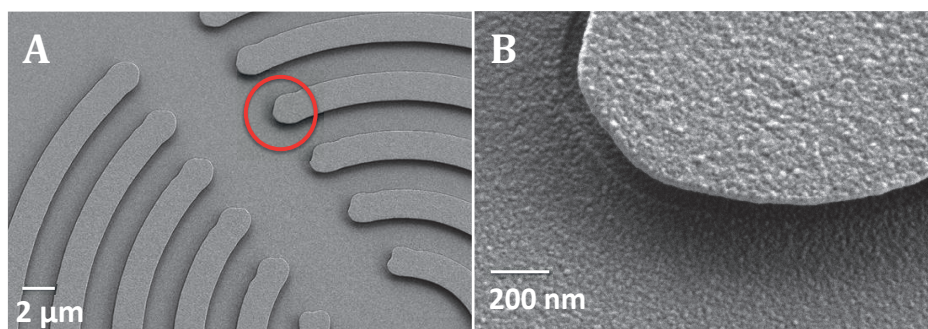
In Chapter 4, we have designed an nanogap IDE structure with an improvement of sensitivity by a factor of 35 compared to micro IDEs designs based on our previous work. However, the sensitivity of sensing device could be further enhanced by increasing the sensing area of the nanogap IDEs with a ring structure. Also, the ring structure for nanogap IDEs is believed to have an advantage in coating sensing materials in circular motions since using dip coating or drop coating methods, the circular structure on the surface of coating areas tends to be evenly covered because of the wettability between polymer solutions and the coating surface (**Figure 6-7**).



**Figure 6.** Another optimal design of nanogap IDEs with ring structure could amplify the total capacity of the device – (A). Ring structure was also widely used as heater elements in other types of gas sensors – (B). [11]

128





**Figure 7.** A design of nanogap IDEs with ring structure has been proposed (chapter 5) and was used to develop capacitive gas sensors for acetone – (A). A high-resolution SEM image shows a gap in nano scale (indicated by a red circle) – (B).

Since the desired material is homogeneously coated in between the nano gaps, high local electric field between these nano gaps can be assured to easily detect a very small amount of acetone, which shows the excellence of nano devices. This method can address high-density nanogap IDEs also in wafer scale by conventional micro-fabrication process. Yet again, by simply changing the active layers into specific advanced materials such as non-conductive polymers or nanocomposite, this generation of nanogap devices is promising to detect a large range of any desired analyte. Furthermore, this type of device has great potential to further evolve using electrochemical methods by using different electroplating solutions for further applications.

Moreover, IDE geometry plays an important role since its capacitance and corresponding signal amplitude increased drastically when scaled down. The sensing area of nanogap IDEs has been increased which leads to the improvement of bare capacitance of the device compared to micro IDEs. Therefore, a larger dynamic range of the capacitance measurement device can be performed and the signal-to-noise ratio has been enhanced. At room temperature, the detection limit of nanogap capacitive sensors depends heavily on the thermal and mechanical stability of cabling connection that causes the change of

parasitic capacitance and the resolution of the measurement is thereby interfered (chapter 5). The combination of the improved capacitance measurement system and using nanoscale configuration could further improve detection limit of devices at sub-ppm level.

## 2. Applications

Detecting acetone concentration is important to human safety and health protection. Especially, it is necessary to inspect toxic and inflammable gases and/or other volatile poisonous chemical leakages for environmental monitoring in industries, warehouses and laboratories. Several examples of acetone gas sensors and other types of gas are given in **Figure 8**. Either as a type of compact alarm detector or as a sensor node integrated with a PCB to be embedded into a gas chamber or gas systems.



**Figure 8.** Gas sensors system, some examples in industries and laboratories.

In human breath, acetone has been found to be an indicator for diabetes mellitus. At high blood glucose levels the liver will break down fatty acids and will also deaminate amino acids. In this altered metabolism state, called ketoacidosis, the ketones acetoacetic acid and

130



$\beta$ -hydroxybutyrate are being produced. Ketoacidosis can be smelled on a person's breath. This is due to acetone, a direct by-product of the spontaneous decomposition of acetoacetic acid. Current detection of diabetes based on breath analysis attracts a lot of interest because of its non-invasive property. It contributes to an improvement of quality of life for patients. **Figure 9** shows several examples of breath analysers that are commercially available for the detection of alcohols and some have incorporated version with wireless sensor nodes. The study on acetone sensors using FET devices as well as chemocapacitors promise a new generation of portable devices for prognosis and diagnosis of diseases such as diabetes, lung cancer and gastro-intestinal, etc. that are non-invasive and patient friendly.



**Figure 9.** Examples of gas sensor as portable breath analyzer for disease diagnosis. [12,13]

### 3. Conclusions

The research described in this thesis encompasses the development of acetone gas sensors and their sensing properties for gas detection at low concentration. Many studies on acetone sensors have been carried out in this research focusing on sensing materials, structures, sensitivity and selectivity, stability of the device in different conditions, reproducibility, optimization of measuring systems, etc. The main goal of this research is to

detect a 0.5 – 2 ppm level of acetone mainly for the detection of acetone in human breath which is a biomarker applicable to diabetes diagnosis. On one hand, we have successfully reached ~ 0.5 ppm using nanowire system (Si NW FET device) to detect 2-octanone. We proposed another type of acetone sensors with micro and nanogap structure (IDEs) using a chemocapacitive-sensing mechanism. Promising results have been achieved and acetone is detected at 1000 ppm and below 10 ppm with and without presence of humidity. This promises to bring progress in the scientific world and also enables a wide range of sensors in sensor technology that is of interest for a variety of indoor and outdoor uses as well as in medical applications to improve the quality of life.

## References

- [1] S. Pfahler, K. Keim, R. Csiki, Q.H. Nguyen, K.C. Liao, M. Stutzmann, J. Schwartz, A. Cattani-Scholz, M. Tornow, A nanogap electrode platform for organic monolayer-film devices, 2016 IEEE 16th Int. Conf. Nanotechnol. (2016) 842–844.
- [2] S.P. Pujari, E. Spruijt, M.A. Cohen Stuart, C.J.M. van Rijn, J.M.J. Paulusse, H. Zuilhof, Ultralow Adhesion and Friction of Fluoro-Hydro Alkyne-Derived Self-Assembled Monolayers on H-Terminated Si(111), *Langmuir*. 28 (2012) 17690–17700.
- [3] G. Konvalina, H. Haick, Sensors for Breath Testing: From Nanomaterials to Comprehensive Disease Detection, *Acc. Chem. Res.* 47 (2014) 66–76.
- [4] G.-J. Sun, H. Kheel, S. Park, S. Lee, S. Eon Park, C. Lee, Synthesis of TiO<sub>2</sub> nanorods decorated with NiO nanoparticles and their acetone sensing properties, *Ceram. Int.* 42 (2016) 1063–1069.
- [5] K.-Y. Dong, J.-K. Choi, I.-S. Hwang, J.-W. Lee, B.H. Kang, D.-J. Ham, J.-H. Lee, B.-K. Ju, Enhanced H<sub>2</sub>S sensing characteristics of Pt doped SnO<sub>2</sub> nanofibers sensors with micro heater, *Sensors Actuators B Chem.* 157 (2011) 154–161.
- [6] X. Kong, Y. Li, High sensitivity of CuO modified SnO<sub>2</sub> nanoribbons to H<sub>2</sub>S at room temperature, *Sensors Actuators B Chem.* 105 (2005) 449–453.
- [7] L.V. Thong, N.D. Hoa, D.T.T. Le, D.T. Viet, P.D. Tam, A.-T. Le, N. Van Hieu, On-chip fabrication of SnO<sub>2</sub>-nanowire gas sensor: The effect of growth time on sensor performance, *Sensors Actuators B Chem.* 146 (2010) 361–367.
- [8] J.-A. Park, J. Moon, S.-J. Lee, S.H. Kim, H.Y. Chu, T. Zyung, SnO<sub>2</sub>-ZnO hybrid nanofibers-based highly sensitive nitrogen dioxides sensor, *Sensors Actuators B Chem.* 145 (2010) 592–595.
- [9] M. Yin, L. Yu, S. Liu, Synthesis of thickness-controlled cuboid WO<sub>3</sub> nanosheets and their exposed facets-dependent acetone sensing properties, *J. Alloys Compd.* 696 (2017) 490–497.
- [10] Q. Jia, H. Ji, Y. Zhang, Y. Chen, X. Sun, Z. Jin, Rapid and selective detection of acetone using hierarchical ZnO gas sensor for hazardous odor markers application, *J. Hazard. Mater.* 276 (2014) 262–270.
- [11] K.Y. Dong, J.K. Choi, I.S. Hwang, J.W. Lee, B.H. Kang, D.J. Ham, J.H. Lee, B.K. Ju, Enhanced H<sub>2</sub>S sensing characteristics of Pt doped SnO<sub>2</sub> nanofibers sensors with micro heater, *Sensors Actuators, B Chem.* 157 (2011) 154–161.
- [12] M.K. Nakhleh, H. Amal, R. Jerjes, Y.Y. Broza, M. Aboud, A. Gharra, H. Ivgi, S. Khatib, S. Badarneh, L. Har-Shai, L. Glass-Marmor, I. Lejbkiewicz, A. Miller, S. Badarny, R. Winer, J. Finberg, S. Cohen-Kaminsky, F. Perros, D. Montani, B. Girerd, G. Garcia, G. Simonneau, F. Nakhoul, S. Baram, R. Salim, M. Hakim, M. Gruber, O. Ronen, T. Marshak, I. Doweck, O. Nativ, Z. Bahouth, D. Shi, W. Zhang, Q. Hua, Y. Pan, L. Tao, H. Liu, A. Karban, E. Koifman, T. Rainis, R. Skapars, A. Sivins, G. Ancans, I. Liepniece-Karele, I. Kikuste, I. Lasina, I. Tolmanis, D. Johnson, S.Z. Millstone, J. Fulton, J.W. Wells, L.H. Wilf, M. Humbert, M. Leja, N. Peled, H. Haick, Diagnosis and Classification of 17 Diseases from 1404 Subjects via Pattern Analysis of Exhaled Molecules, *ACS Nano*. 11 (2017) 112–125.
- [13] I. Nardi-Agmon, M. Abud-Hawa, O. Liran, N. Gai-Mor, M. Ilouze, A. Onn, J. Bar, D. Shlomi, H. Haick, N. Peled, Exhaled Breath Analysis for Monitoring Response to Treatment in Advanced

Lung Cancer, J. Thorac. Oncol. 11 (2017) 827–837.

# Appendix

## A. Fluorinated-Alkyne derived Monolayers on Oxide-Free Silicon Nanowires via One-step Hydrosilylation

### 1. Chemicals

Hexadec-1-yne (**F0**), 16-fluorohexadec-1-yne (**F1**), 16,16,16-trifluorohexadec-1-yne (**F3**), and 13,13,14,14,15,15,16,16,16-nonafluoro-hexadec-1-yne (**F9**) were synthesized following a known procedure.[1] The details of the synthesis of 9,9,10,10,11,11,12,12,13,13,14,14,15,15,16,16,16-heptadecafluoro-hexadec-1-yne (**F17**) are described in the *Supporting Information, Section S1*. In brief, compound **F17** was obtained via a four-step reaction (see for details *Supporting Information Scheme S1*). The radical chain addition of heptadecafluoro-1-iodooctane to 5-hexene-1-ol using sodium dithionite ( $\text{Na}_2\text{S}_2\text{O}_4$ ) (in acetonitrile and water, RT, 4 h) yielded heptadecafluoro-5-iodotetradecan-1-ol, and was followed by the reduction of the iodide using lithium aluminium hydride ( $\text{LiAlH}_4$ ) (in dry ether, 0 °C, 24 h) to give heptadecafluorotetradecan-1-ol. Next, the alcohol was brominated using hydrobromic acid (HBr) (in presence of sulfuric acid, 100 °C, 18 h) to yield 14-bromo-heptadecafluorotetradecane. Finally, a nucleophilic substitution with lithium acetylide (in dimethyl sulfoxide, 0 °C, after which tetrahydrofuran was added, 50 °C, 4 h), resulted in heptadecafluorohexadec-1-yne (**F17**). The critical difference with a previous route<sup>35</sup> was that this one is environmentally friendly, required less harsh conditions, and most importantly this method provided as improvement that no internal alkene was obtained as a side product. In the end, this route resulted in a typical yield of 45% of the final desired alkyne, which was used in a purity of 99.98%.

Acetone (Sigma Aldrich, semiconductor grade VLSI PUNARAL Honeywell 17617), ethanol (EtOH, Sigma Aldrich), and dichloromethane (DCM, Sigma Aldrich) were used for cleaning before modification, Milli-Q water (resistivity 18.3 M $\Omega$  × cm) was used for rinsing Si NWs

samples after the etching process. Ethylene glycol (EG), dimethylformamide (DMF), and n-hexadecane (C16, 99%) were obtained from Sigma Aldrich and used as received to determine the critical surface tension in contact angle measurements. Hydrogen peroxide (Sigma Aldrich, 50%) and sulfuric acid (Sigma Aldrich, 96%) were used to make piranha solution (3:1 v/v) during pre-treatment to remove carbon contamination from the nanowire surfaces. HF (Sigma Aldrich, 49% in water) and NH<sub>4</sub>F (Riedel-de Haën, 40 %, semiconductor grade VLSI PURANAL Honeywell 17600) were used as etchants. Carbon tetrachloride (CCl<sub>4</sub>) (Sigma Aldrich, > 99.5%) and potassium bromide (KBr) (Sigma Aldrich, > 99.5%) were used as received.

## 2. Synthesis of Heptadecafluorohexadec-1-yne (F17)

### 2.1. 7,7,8,8,9,9,10,10,11,11,12,12,13,13,14,14,14-heptadecafluoro-5-iodotetradecan-1-ol (1a)

A mixture of 6.00 g of heptadecafluoro-1-iodooctane (11.00 mmol), 0.92 g 5-hexen-1-ol (9.16 mmol), 1.60 g of sodium dithionite (9.16 mmol) and 0.770 g of sodium bicarbonate (9.16 mmol) in 30 mL of acetonitrile and 10 mL of water was stirred at room temperature for 4 hours. Afterwards the mixture was diluted with 100 mL of water and extracted three times with 30 mL of ethyl acetate. The organic layers were combined and washed with brine (30 mL), dried over sodium sulfate and filtered. The filtrate was concentrated under reduced pressure yielding 4.72 g of the product (6.60 mmol, 72%). <sup>1</sup>H-NMR (400 MHz, CDCl<sub>3</sub>, δ(ppm)): 1.39-1.70 (m, 5H), 1.88 (m, 2H), 2.87 (m, 2H), 3.69 (t, J= 6Hz, 2H), 3.43 (m, 1H).

### 2.2. 7,7,8,8,9,9,10,10,11,11,12,12,13,13,14,14,14-heptadecafluorotetradecan-1-ol (1b)

An amount of 8.12 g (10.88 mmol) of **1a** was dissolved in 40 mL of dry diethyl ether. The mixture was cooled to 0 °C and 6.5 mL of a lithium aluminium hydride solution (4.0 M in diethyl ether) was added drop wise. The mixture was stirred overnight, after which the

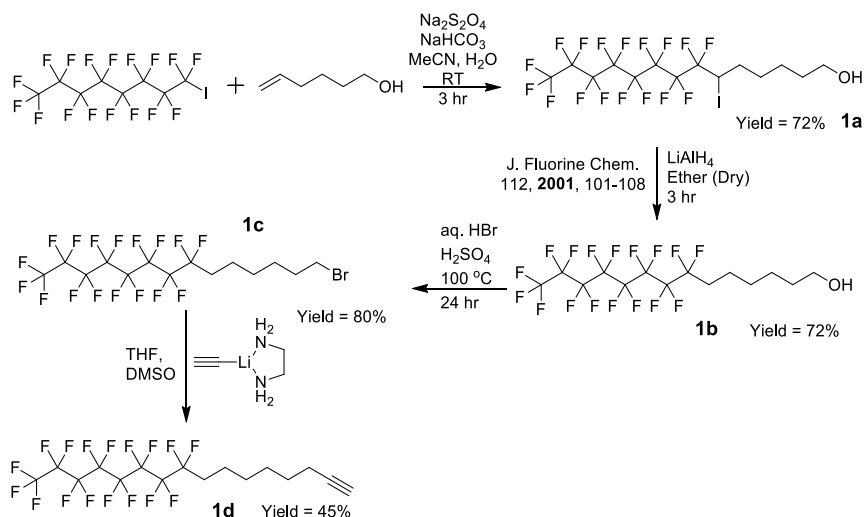
reaction was quenched by adding water. The resulting suspension was filtered and the filtrate was concentrated under reduced pressure yielding the crude product, which was recrystallized in toluene. Yield: 4.10 g (7.88 mmol, 72%). <sup>1</sup>H-NMR(400 MHz, CDCl<sub>3</sub>, δ(ppm)): 1.27 (t, J= 5.2 Hz, 1H) 1.40-1.43 (m, 4H), 1.58-1.68 (m, 4H), 2.01 (h, J= 8Hz, 2H), 3.58 (q, J= 6.4Hz, 2H).

2.3. 14-bromo-1,1,1,2,2,3,3,4,4,5,5,6,6,7,7,8,8-heptadecafluorotetradecane (1c)

An amount of 2.5 g (5.3 mmol) of **1b** was dissolved in 25 mL of hydrobromic acid. To this mixture, 2.5 mL of sulphuric acid was added. The mixture was stirred at 100 °C for 18 hrs. Afterwards, 100 mL of water was added and the mixture was extracted three times with heptane. The organic layers were combined and washed 2 times with a saturated sodium bicarbonate solution and 2 times with brine. The organic layer was separated, dried with sodium sulphate and filtered. The filtrate was concentrated under reduced pressure. The product was isolated via column chromatography using heptane as eluent. Yield: 2.50 g (4.28 mmol, 80%). <sup>1</sup>H-NMR (400 MHz, CDCl<sub>3</sub>, δ(ppm)): 1.37-1.51 (m, 4H), 1.63 (q, J= 8 Hz, 2H) 1.88 (q, J= 8Hz, 2H), 2.08 (h, J= 8Hz, 2H), 3.41 (q, J= 6.4 Hz, 2H).

2.4. 9,9,10,10,11,11,12,12,13,13,14,14,15,15,16,16,16-heptadecafluorohexadec-1-yne (1d)

A solution of 1.18 g (12.85 mmol) of lithium acetylide in 6 mL in dimethyl sulfoxide was prepared in a dry and argon purged three-necked flask. The mixture was cooled to 0 °C, after which a solution of **1c** (5.00 g (8.57 mmol)) in 15 mL tetrahydrofuran was added drop wise. After the addition, the mixture was heated to 50 °C and stirred for 4 hrs. After cooling to room temperature, an amount of 100 mL of water was added to quench the excess of lithium acetylide. The aqueous mixture was extracted 3 times with 50 mL n-heptane. The organic layers were combined and washed with brine (3 x 50 mL) and dried over sodium sulfate. After filtration and concentration under reduced pressure, the product was obtained via column chromatography using n-heptane as eluent in a yield of 2.00 g (3.7 mmol, 45%). <sup>1</sup>H-NMR(400 MHz, CDCl<sub>3</sub>, δ(ppm)): 1.39-1.65 (m, 8H), 1.95 (t, J= 2.4Hz, 1H), 2.07 (h, J= 8Hz, 2H), 2.01 (m, 2H).



**Scheme S1.** Synthetic routes for Heptadecafluorohexadec-1-yne (**F17**)

### 3. H-terminated Si NWs

#### 3.1. Preparation of H-terminated Si NWs

**Si NWs Formation.** Si NWs were prepared onto Si(111) wafers by chemical vapor deposition of  $\text{SiH}_4$  and  $\text{B}_2\text{H}_6$  (B/Si atom ratio 1:20000) as precursor gases and gold as a catalyst; the details of the Si NWs synthesis and properties have been published elsewhere.<sup>[2]</sup>

**Surface Cleaning and Pre-treatment of Si NWs (Scheme 1).** After the growth of the Si NWs, organic contaminants have to be removed from their surface. To this aim, Si (111) wafers with Si NWs grown onto them were cut into  $5\text{ mm} \times 5\text{ mm}$  pieces, subsequently rinsed with Milli-Q water, ethanol, acetone and DCM, and then dried under a stream of argon (Ar). This was followed by a treatment with piranha solution (CAUTION: extremely corrosive!; 50% aq.  $\text{H}_2\text{O}_2$  : 98%  $\text{H}_2\text{SO}_4$  (1:3 v/v) for 15 min) to remove all organic contaminants. Samples were then rinsed with excess amounts of Milli-Q water and dried

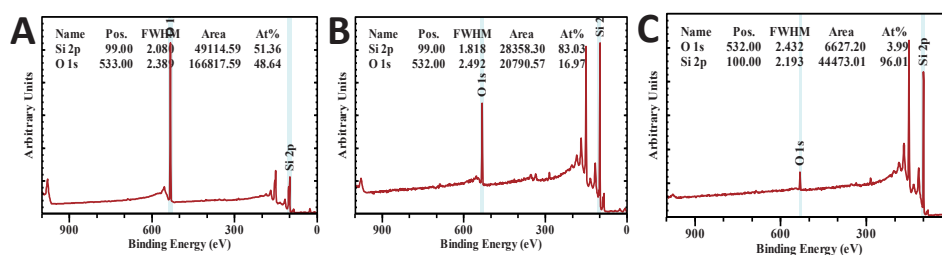


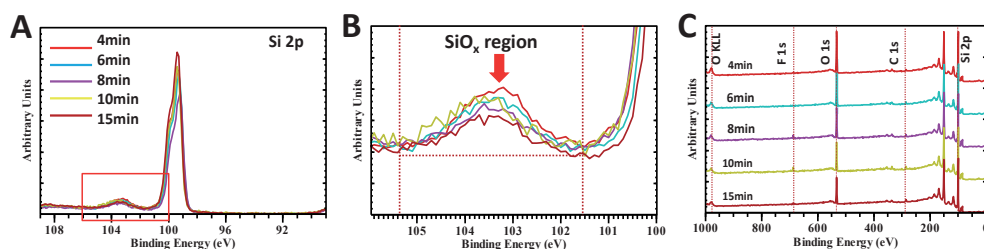
under Ar. Finally, the samples were treated by either an ambient air or oxygen plasma to remove any final traces of carbon contamination. The HF or  $\text{NH}_4\text{F}$  etching process was started directly after this. The effects of these treatments were studied and compared by wide-range XPS survey scans (See Table S1). Before any covalent surface modification, the small C1s peak attributed to native hydrocarbon contamination was always observed, and is unavoidable in ambient atmosphere. Evidently, plasma treatment helps to minimize this carbon contamination to the lowest level (typically  $\sim 1\%$ ), but, of course, at the price of significant oxidation of the Si NWs. Upon plasma cleaning the intensity of the oxygen peak increased from 44.4% (native oxide from untreated samples) to 50.8%. Piranha cleaning without plasma yielded less surface oxidation (46.1%), but was also less effective in reducing the carbon contamination (down to  $\sim 2.4\%$ ).

**Anisotropic Etching of Si NWs to form Si-H Species.** To remove any oxides that are present at the Si NWs surface, a series of possible etching procedures was tested. To this aim, samples were immersed in etching solution for a specified time, which was followed by thorough washing with excess water (Milli-Q) and drying under a stream of Ar for about 10 s. During the etching process, the samples were occasionally swirled to remove gas bubbles that were trapped between the Si NWs on the surface. This process was executed at room temperature, 25 °C (RT) in a  $\text{N}_2$  environment glovebox with less than 0.1%  $\text{O}_2$ . All solvents were bubbled by an Ar stream for at least 15 min in order to reduce oxygen concentration. Etching studies with freshly prepared etchants were executed with 40%  $\text{NH}_4\text{F}$  and 2.5% HF solutions, using different time intervals (typically minutes with  $\text{NH}_4\text{F}$  and seconds with HF) to optimize the removal of the silicon oxide layer ( $\text{SiO}_x$ ) and produce hydrogen-terminated (H-terminated) Si NWs while minimizing the damage by dissolution of the Si NWs during the etching process.

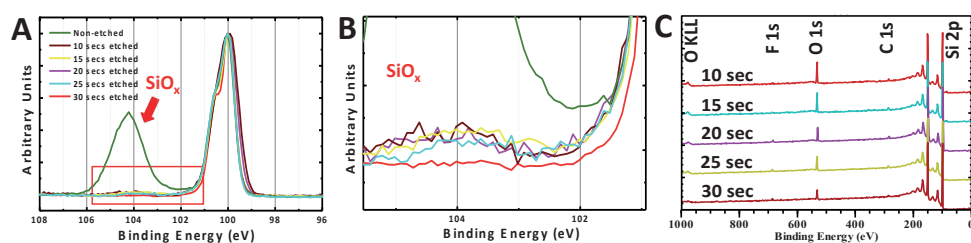
**Table S1.** Surface treatment before etching step and modification

Si NWs	C 1s	O 1s	F 1s	Si 2p
Surface treatment	285.0 eV	531.0 eV	686.0 eV	99.0 – 100.0 eV
	[% SiO <sub>x</sub> ]			
1. Air plasma 5 min	1.1	49.7	0.7	24.2 [24.3]
2. O <sub>2</sub> plasma 5 min	1.2	50.8	1.8	22.0 [24.2]
3. Air plasma 5 min and piranha 10 min	0.7	50.6	0.3	23.9 [24.5]
4. Piranha 10 min	2.4	46.1	<0.2	27.4 [22.9]

**Figure S1.** XPS survey scan of Si NWs samples on Si substrate with native oxide SiO<sub>x</sub> (A), and after etching process by immersing in NH<sub>4</sub>F (15 min) (B); by HF (30 sec) (C) to create hydrogen termination onto Si NWs surfaces.

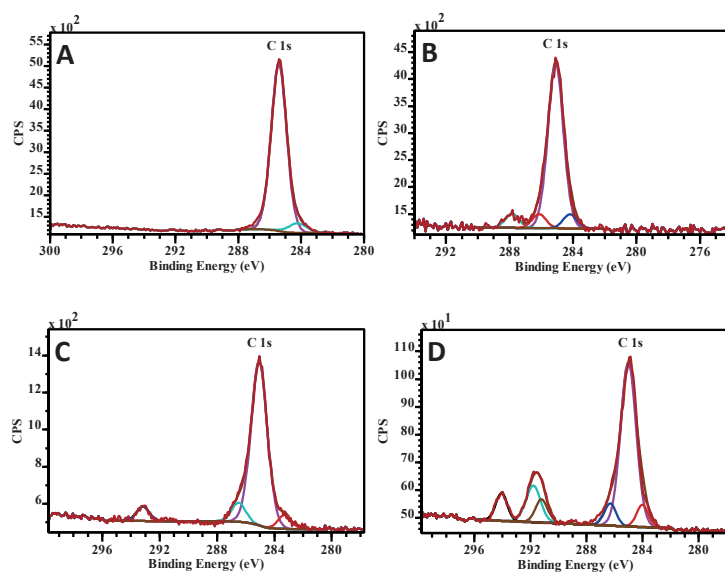


**Figure S2.** Normalized XPS spectra of Si NWs surface etched by  $\text{NH}_4\text{F}$ .



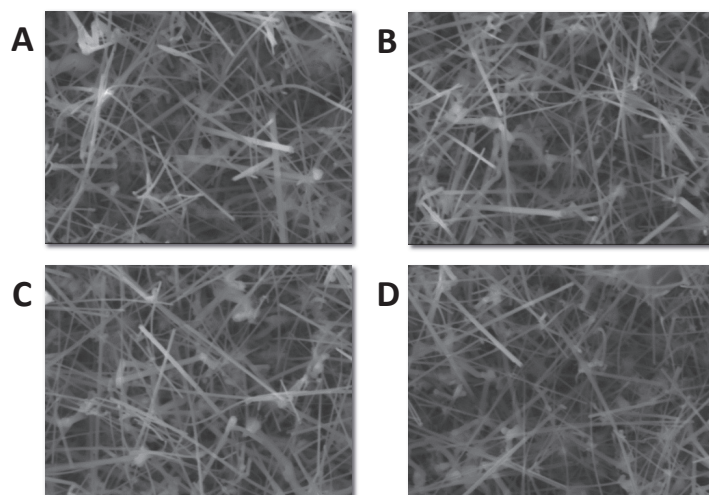
**Figure S3.** Normalized XPS spectra of Si NWs surface etched by  $\text{HF}$ .

4. C1s XPS narrow scan of fluorinated alkyne derived monolayers on oxide-free Si NWs



**Figure S4.** XPS narrow scan C 1s region of freshly prepared fluoro-hydro derived monolayers on Si NWs **F0**-(A), **F1**-(B), **F3**-(C), **F9**-(D).

## 5. Surface morphology of Si NWs “forest” by SEM



**Figure S5.** SEM images of Si NWs are shown before (A) and after modification: **F1**-(B), **F3**-(C), **F9**-(D). No change has been observed between samples before and after modification

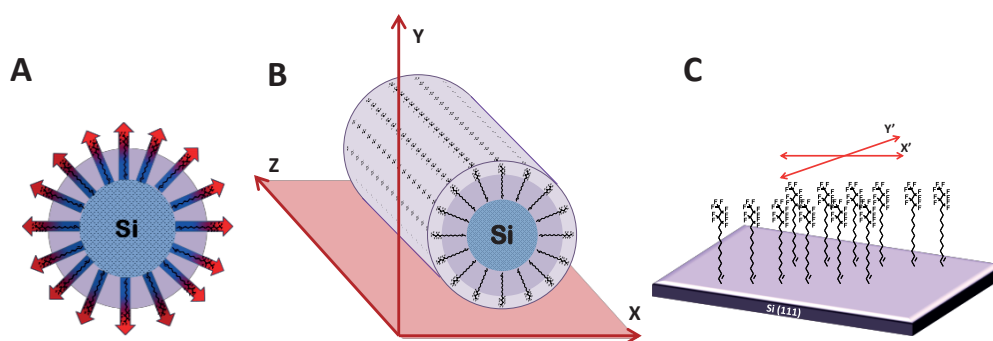
## 6. Wettability

**Equation S1.**  $[W_A = \gamma_L(1 + \cos\theta_a)]$  .....eq.(1)

**Table S4.** Static contact angle ( $\theta$ ) measurement of modified and non-modified SiNWs with different liquid surface tension ( $\gamma_L$ ) in  $\text{mN}\cdot\text{m}^{-1}$ : n-Hexadecane, DMF, EG and water. Symbol (-) indicates SCA below  $10^\circ$ .

Liquid surface tension $\gamma_L$ ( $\text{mN}\cdot\text{m}^{-1}$ )	n-Hexadecane 27.5	DMF 36.8	EG 47.7	Water 72.8
F17	-	$112 \pm 2$	$149 \pm 1$	$168 \pm 2$
F9	-	$78 \pm 2$	$149 \pm 1$	$169 \pm 2$
F3	-	-	$141 \pm 1$	$170 \pm 2$
F1	-	-	$120 \pm 2$	$169 \pm 1$
F0	-	-	$141 \pm 1$	$163 \pm 2$
SiO <sub>x</sub>	-	-	$11 \pm 2$	-
Si-H	-	-	-	-

#### 7. Fluorinated alkyne derived monolayers by FT-IR



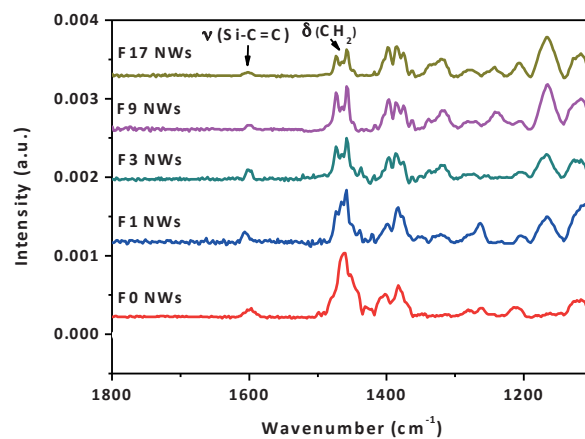
**Figure S6.** Multiple oriented-growth orientation (A); Monolayer on single Si NWs (B) and 2D lateral electronegative interaction of fluorine atoms between molecules on planar Si surface (C).

**Table S2.** C-H region of modified Si NWs with fluorinated alkyne derived monolayers

	<b>F0</b>	<b>F1</b>	<b>F3</b>	<b>F9</b>	<b>F17</b>
<b>-CH<sub>3</sub></b>	2956.2	2958.6	2959.7	2960.8	-
<b>-CH<sub>2</sub>(U<sub>s</sub>)</b>	2920.1	2922.2	2922.5	2922.6	2923.4
<b>-CH<sub>2</sub>(U<sub>a</sub>)</b>	2850.8	2851.2	2852.1	2852.8	2854.1

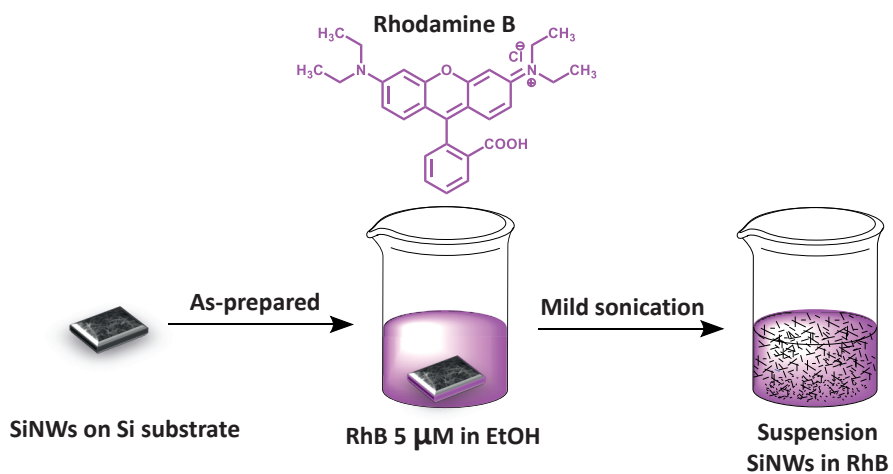
**Table S3.** Energy shift of C-F signal (CF<sub>3</sub> group) in C 1s narrow scan between F<sub>x</sub>-planar Si and F<sub>x</sub>-Si NWs

<b>Modified Si NWs</b>	<b>C-F signal (CF<sub>3</sub> group)</b>			<b>C-F signal (CF<sub>2</sub> group)</b>		
	<b>NWs</b>	<b>Planar Si</b>	<b>Energy shift (Δ)</b>	<b>NWs</b>	<b>Planar Si</b>	<b>Energy shift (Δ)</b>
<b>F17</b>	294.4	293.7	0.7	292.2	291.5	0.7
<b>F9</b>	294.3	293.8	0.5	292.1	291.6	0.5
<b>F3</b>	293.4	293.1	0.3	-	-	-



**Figure S7.** Infrared spectra of fluorinated alkyne-derived monolayers (**F0**, **F1**, **F3**, **F9**, **F17**) on Si NWs surfaces region 1100 – 1800  $\text{cm}^{-1}$  by transmittance measurements of Si NWs in KBr pallets prepared from suspensions of modified Si NWs.

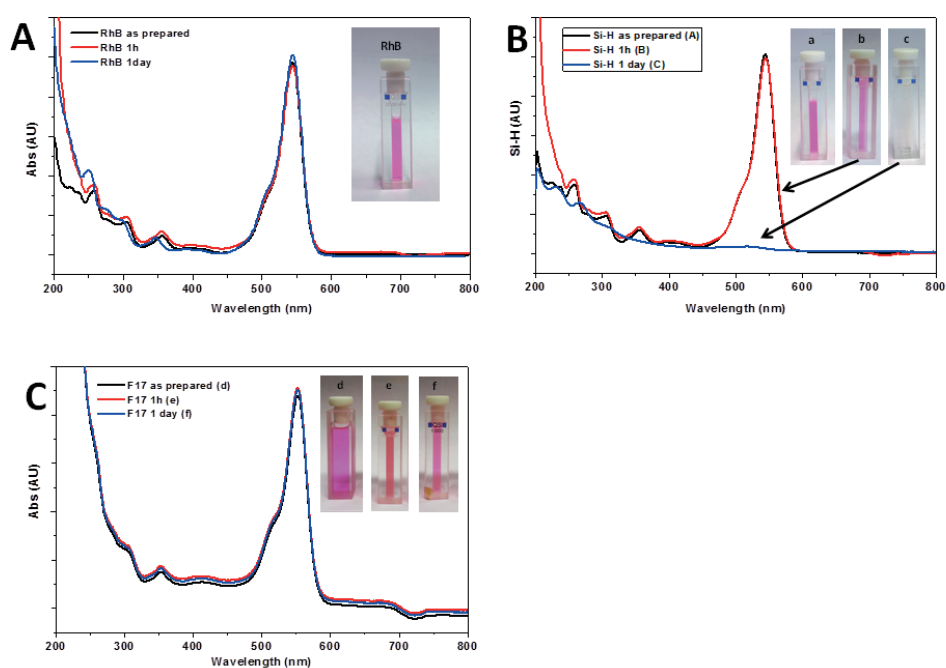
#### 8. Stability of fluorinated alkyne derived monolayers on Si NWs by UV-VIS



**Scheme S2.** Preparation of Si NWs suspensions in RhB (using EtOH as solvent)



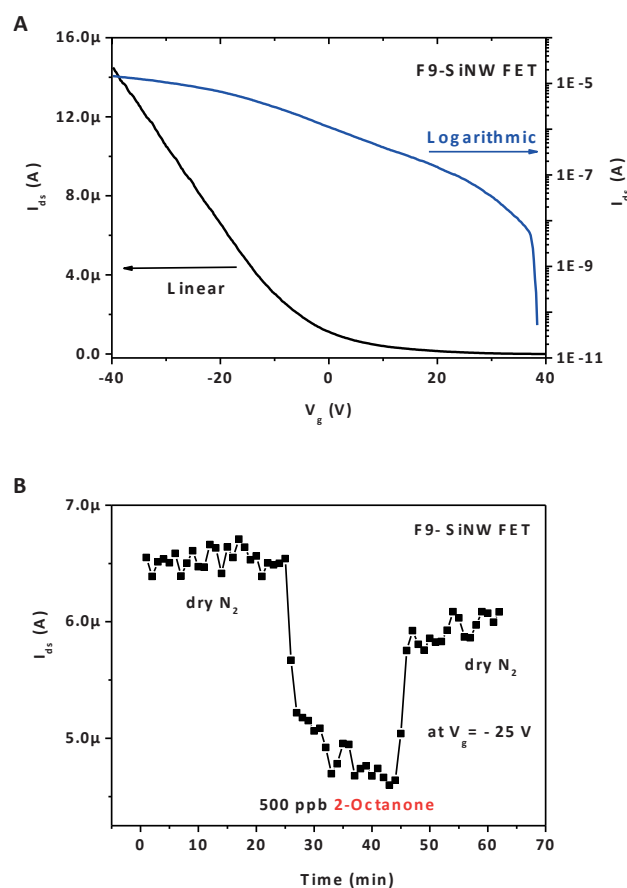
Quartz vessels (SUPRASIL, HELMA Analytics) with the transmission band ranging from 200 nm to 2500 nm were used for every UV measurement are same as they had been used for UV exposure. The intensity of UV irradiation was determined by using an UV lamp with a power of 8 Waats which was placed to create direct exposure with a distance between lamp and all samples is 1 cm.



**Figure S8.** UV-VIS spectra of (A)- pure RhB, (B)- **Si-H** NWs and (C)-**F17-Si** NWs in RhB at conc. of 5  $\mu\text{M}$  in absolute ethanol as in fresh-prepared (black), after 1 hour (red) and 1 day (blue) irradiating with UV at 254 nm, lamp power 8 Watts.

## 9. Surface modified Si NWs-based Field Effect Transistors (FETs)

Surface modified Si NWs were dispersed into ethanol by ultra-sonication. These Si NWs suspensions were spray coated on Si with a 300 nm oxide layer to form an aligned array. The source/drain electrodes (Ti/Au, 30 nm/100 nm) were prepared using photolithography and e-beam evaporation. The width of metal electrodes and distance between two electrodes was 3  $\mu\text{m}$ . A Keithley 2636A source-meter was employed to test the electrical properties of the surface modified Si NWs FETs. The source/drain current  $I_{\text{ds}}$  was measured at constant source/drain voltage ( $V_{\text{ds}} = 2 \text{ V}$ ) while scanning gate voltage ( $V_{\text{g}}$ ) from 40 V to  $-40 \text{ V}$  with  $-0.2 \text{ V}$  step.



**Figure S9.** Linear (black line) and logarithmic (blue line) scale  $I_{ds}$ - $V_g$  plot of **F9**-modified Si NWs FETs (A) and time-dependent  $I_{ds}$  response of **F9** modified Si NWs FETs at  $V_g = -25$  V exposure towards 2-octanone at 500 ppb to reference air (dry  $N_2$ ) (B).

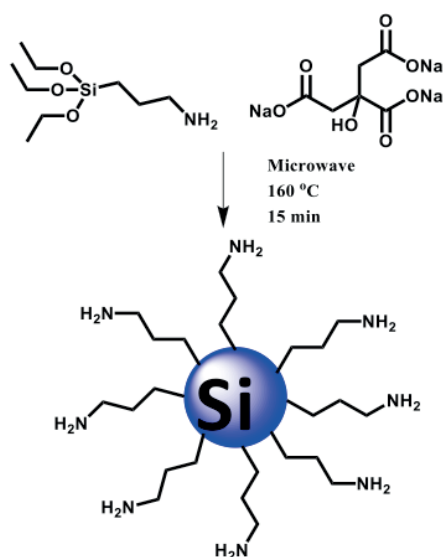
## References

- [1] S.P. Pujari, E. Spruijt, M.A. Cohen Stuart, C.J.M. van Rijn, J.M.J. Paulusse, H. Zuilhof, Ultralow Adhesion and Friction of Fluoro-Hydro Alkyne-Derived Self-Assembled Monolayers on H-Terminated Si(111), *Langmuir*, 28 (2012) 17690-17700.
- [2] T. Stelzner, G. Andrä, E. Wendler, W. Wesch, R. Scholz, U. Gösele, S. Christiansen, Growth of silicon nanowires by chemical vapour deposition on gold implanted silicon substrates, *Nanotechnology*, 17 (2006) 2895.

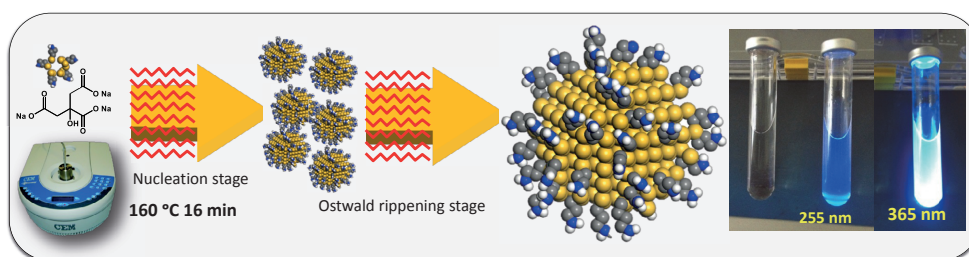
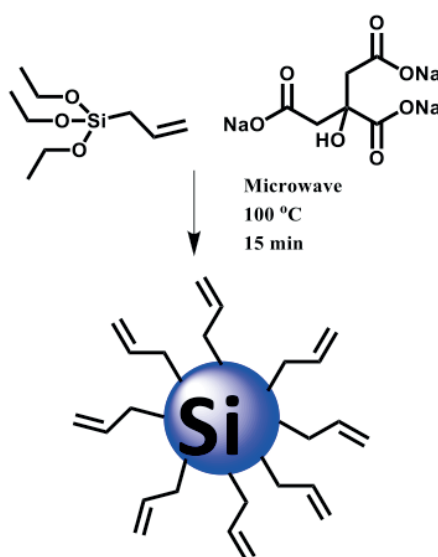
## B. Preparation and Gas Sensing Properties of Nanocomposite Polymers on Micro-Interdigitated Electrodes for Detection of Volatile Organic Compounds at Room Temperature

### 1. Preparation of nanoparticles.

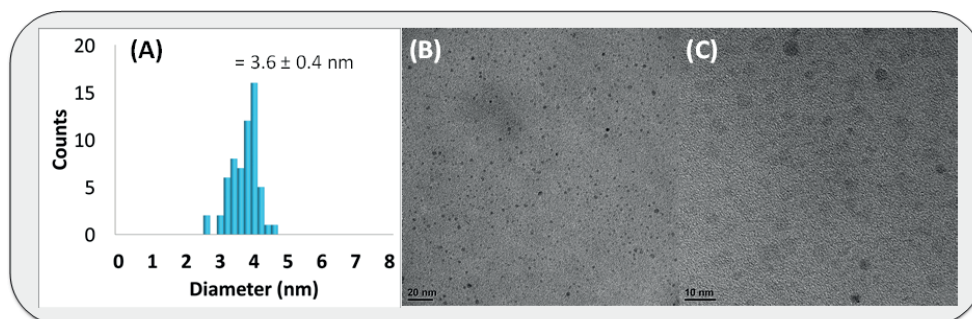
#### (A) Si NPs -NH<sub>2</sub>



#### (B) Si NPs -alkene

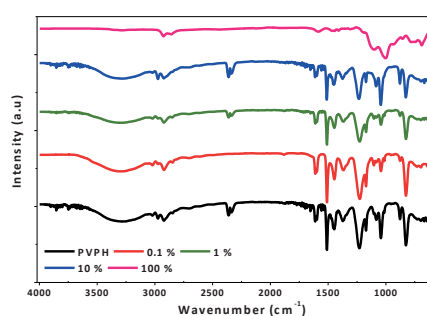


**Figure S1.** Schematic Illustration of Bottom-up One-Pot Synthesis of amine terminated SiNPs. After synthesis photos were taken with irradiation with a hand-held UV lamp.

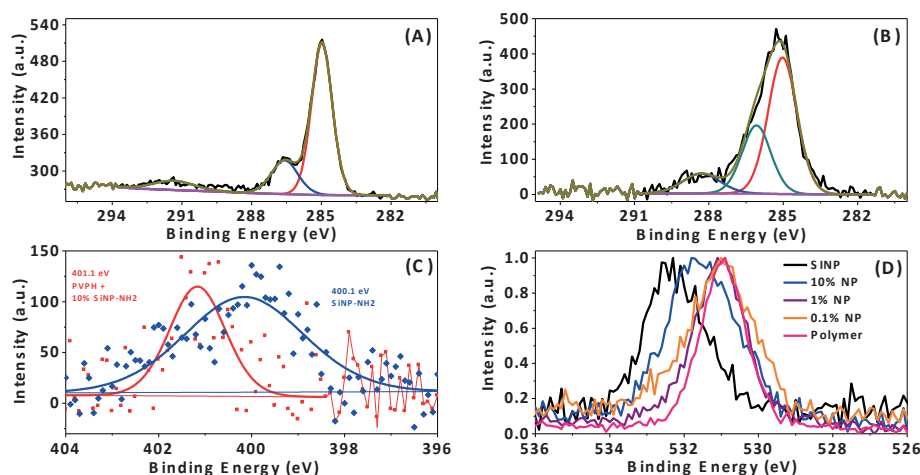


**Figure S2.** The DLS (dynamic light scattering) size distribution, TEM (transmission electron microscopy) overview image (B), and enlarged TEM image (C) of amine terminated Si NPs.

## 2. Characterization

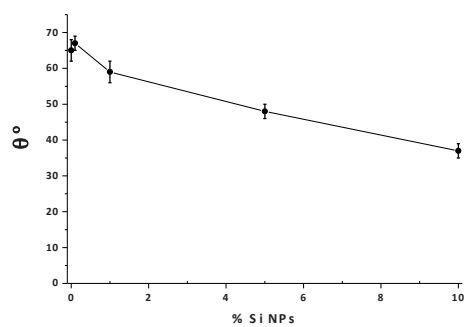


**Figure S3.** The partial FT-IR spectra of the pristine PVPH (black curve) and PVPH NPs nanocomposite with the concentration of SiNPs: 0.1 % (red curve), 1 % (green curve), 10 % (blue curve) and 100 % (pink curve).

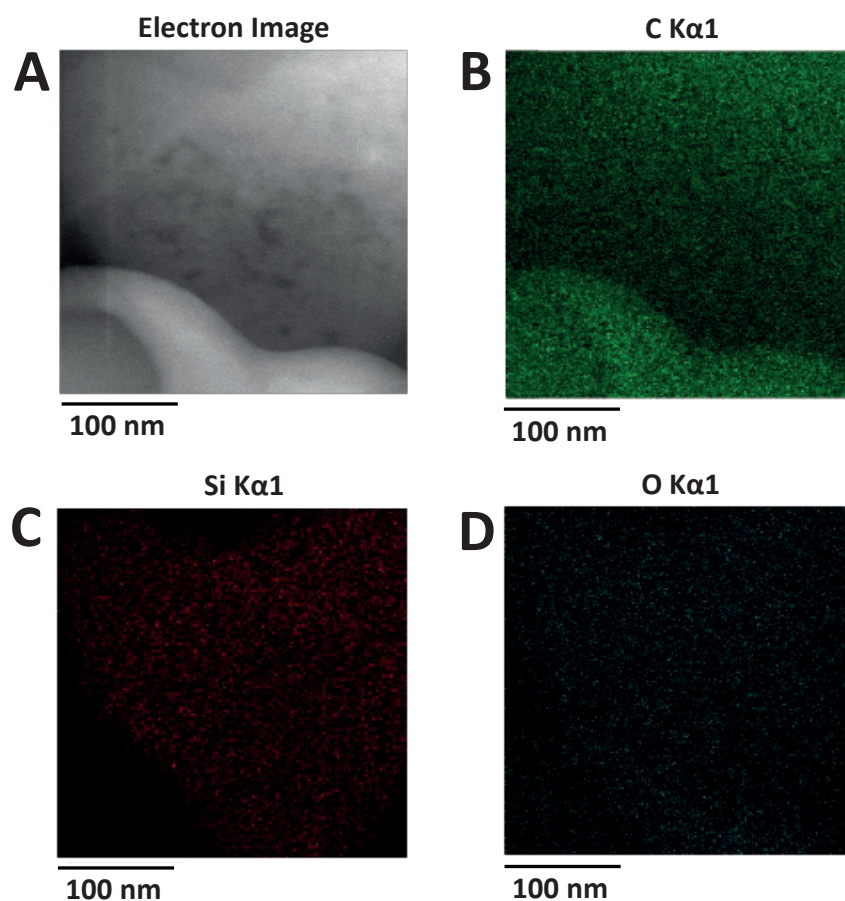


**Figure S4.** XPS spectra of C1s of pure SiNPs-NH<sub>2</sub> (A), C1s spectra of 10% SiNPs-NH<sub>2</sub> in PVPH (B), N1s spectra of pure SiNPs-NH<sub>2</sub> (C) and 10% SiNPs-NH<sub>2</sub> in PVPH and O1s spectra (pure SiNPs-NH<sub>2</sub>, 10 % SiNPs, 1 % SiNPs, 0.1 % SiNPs and pure PVPH) (D).

To check the polymer coating of the M-IDE chip, we measured the static contact angle (SCA). Using a 20 wt. % solution of PVPH in ethanol for spin coating, we obtained an SCA of 65° (See **Figure S5**), which corresponds well with the values reported in literature (between 56° and 72°).[1-4] When NPs are added in significant amounts (> 1%) to the polymer layer, the SCA starts to decrease. This decrease can be explained by the hydrophilic -NH<sub>2</sub> functional groups on the NPs surface which increase the hydrophilicity of the PVPH layer.



**Figure S5.** Water static contact angle ( $\theta$ ) of a glass surface coated with pure PVPH and PVPH – Si NPs nanocomposite in EtOH at different concentration (wt. %).



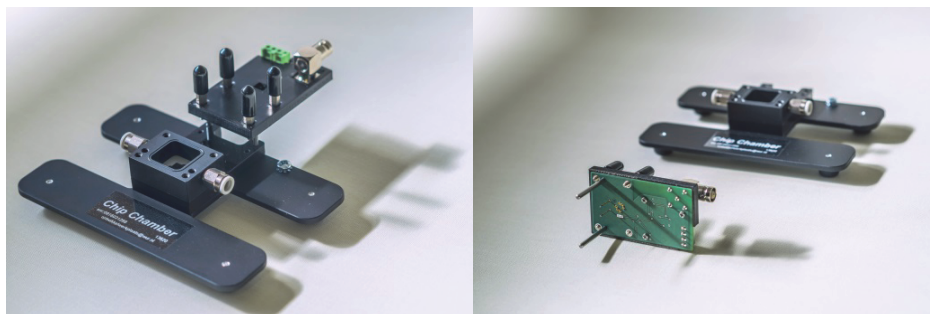
**Figure S6.** Regional SEM image of PVPH - Si NPs in EtOH (A) and its elementary scanning EDS images for: carbon region in light-green area (B), silicon region in red area (C) and oxygen in dark-olive area (D). As shown, carbon (B) and silicon (C) are partially present in the scanning area while oxygen is spreading widely all over the place since it takes part in the composition of PVPH as well as Si NPs.

Elementary scanning EDS images also support our characteristic studies of the nanocomposite. **Figure S6** shows a zoom-in area of the PVPH – Si NPs system with the silicon region in red (Figure S6C) showing that Si NPs are present in the nanocomposite as



confirmation to what has been observed via TEM technique. Furthermore, the presence of NPs in the polymer was confirmed by FT-IR and XPS measurements (supporting information Figure S3 and S4 respectively). XPS measurements also show a shifting O1s and N1s binding energy peak for PVPH with different amounts of SiNPs-NH<sub>2</sub>, which indicates interaction between the NPs and the polymer.

### 3. Gas measurement



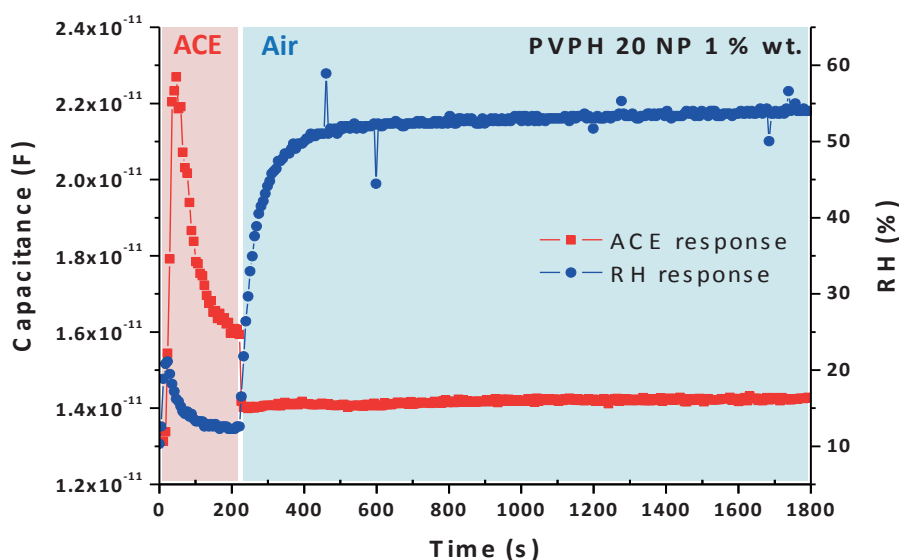
**Figure S7.** Gas chamber for sensing measurement

Individual experiments were also carried out by exposing target gas vapour onto the front sensing layer of the sensor. In all experiments, the capacitance response was measured as the change of the real capacitance value of sensor with respect to the reference value at the point when target gas presents. The capacitance first reached its maximum value when the sensing layer is “completely wetted” with the analyte. Then, capacitance remained almost same value so-called “saturated state” when no more gas molecule could be captured in the sensing layer that caused the increase in capacitance signal.

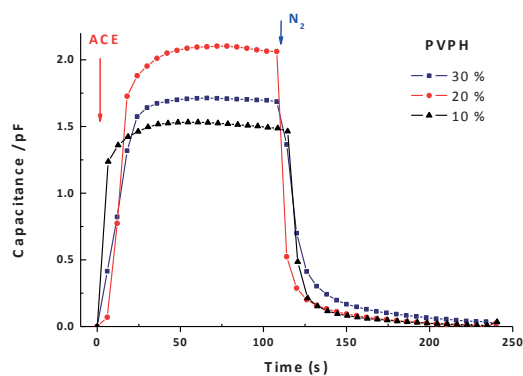
To acquire comprehension of sensing behaviour, the sensor was examined in turn-on and –off mode of gas exposure. Prior to gas injection (turn-on mode), the sensor was allowed to stabilize for about few seconds at dry state. Afterwards, the sensor was exposed to target gas for 120 seconds to reach the maximum capacitance value and saturated state It has

155

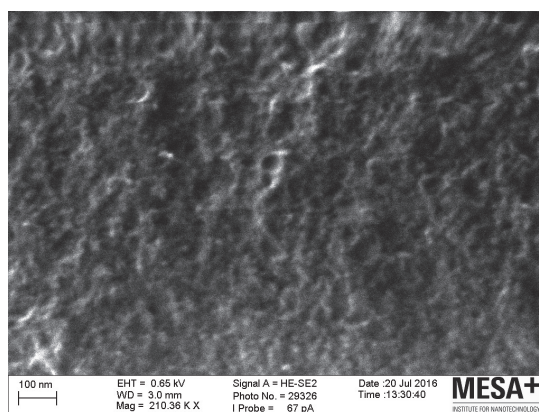
been observed that after gas exposure (turn-off mode), the evaporation of analyte from the sensing layer of the device takes place, giving a rapid return of the capacitance to its original value, correspondent with dry state of the sensor (see more detail in Figure S8). The reversible responses to original value suggest that the recovery feature of the sensor is comparable with other types of chemocapacitive sensor. [5, 6]



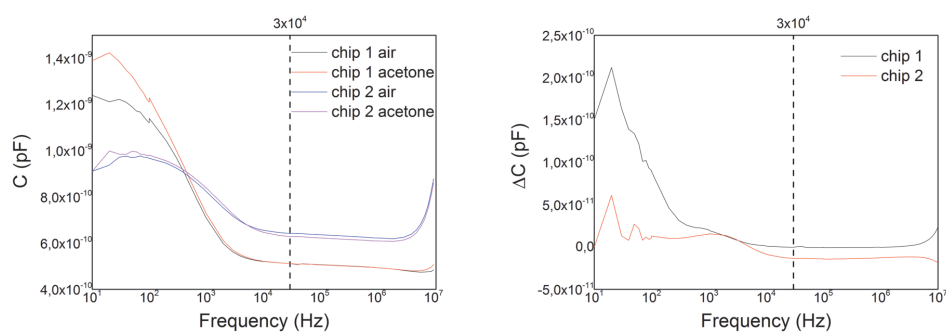
**Figure S8.** Capacitive response of sensor to acetone (ACE) in red and humidity level in blue line (measured by separate humidity sensor). After 200 sec of exposure, the acetone stream was turned off and the M-IDE responses to humidity in ambient environment. As can be noticed, at this level, humidity does not affect the adsorption of ACE into the polymeric layer since the capacitive signal drops while humidity level increases.



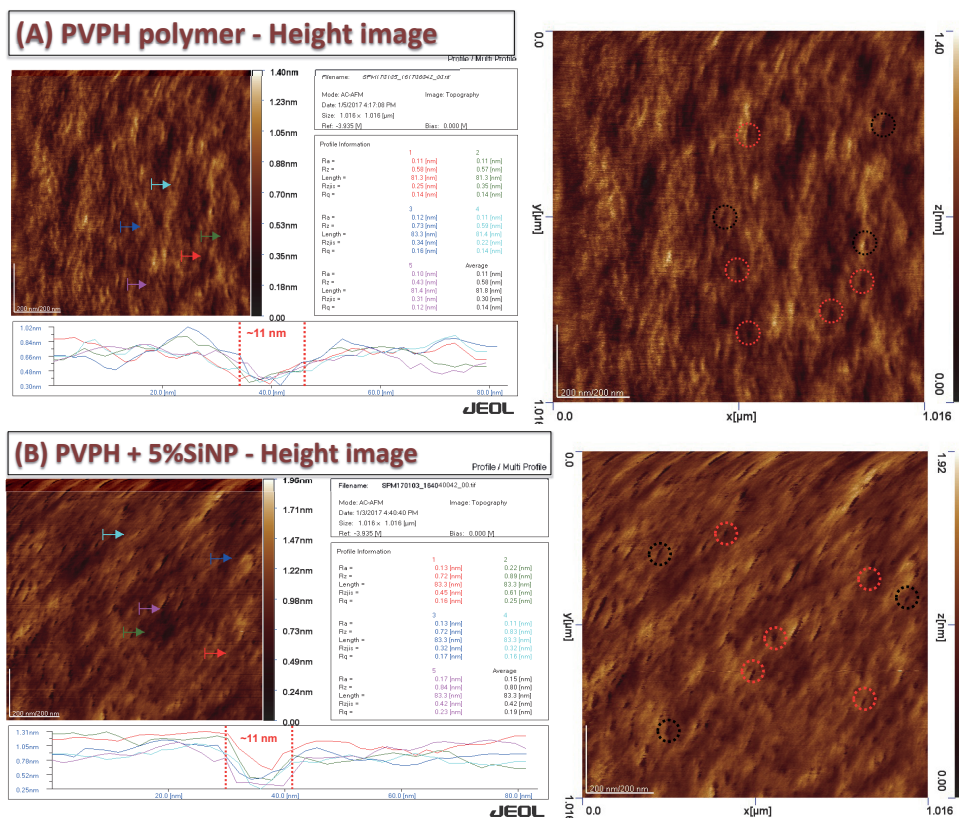
**Figure S9.** Adsorption and evaporation behaviour corresponding with an acetone injection of PVPH layer with different concentrations.



**Figure S10.** Morphology of PVPH 20 blended with 1 % NPs polymer layer by SEM image with 100 nm scale.



**Figure S11.** Capacitance of two chips measured with and without acetone present. A stable region is found between 10 kHz and 1 MHz. For our measurements we chose 30 kHz, which is indicated by the dashed line.



**Figure S12.** AFM topographical analysis of nano-porous surfaces: (A) PVPH polymer and (B) PVPH + 5% SiNPs roughness parameters. Height profile shown in left side for the same circled spots shown in right side images.

#### 4. Calculation of surface increase by NPs

Our IDE has a sensitive surface area of 300 (length fingers) times (124 x (10 + 6)) (number of fingers x (width fingers + gap width) = 595200  $\mu\text{m}^2$  or 0.6  $\text{mm}^2$ .

Assuming the polymer layer is 3  $\mu\text{m}$  thick (resulting thickness for a 20 wt. % PVPH solution), the volume of the layer is 0.002  $\text{mm}^3$ .

Using the density ( $\rho$ ) of silicon (2.3 g/ml) and that of PVPH (1.16 g/ml) we can calculate the volume fraction of the NPs in the final polymer layer from the wt. % they take in the initial dispersion:

$$\text{vol. \% NP} = \frac{\text{wt. \% NP}}{\left(\frac{\text{wt. \% PVPH}}{\rho_{\text{PVPH}}} + \frac{\text{wt. \% NP}}{\rho_{\text{NP}}}\right) \rho_{\text{NP}}}$$

Since we know the volume of the layer ( $V_{\text{layer}}$ ) and the radius ( $r$ ) of the NPs, we can first calculate the number of nanoparticles ( $N_{\text{NP}}$ ) in the polymer layer and from that the total surface area of these nanoparticles ( $A_{\text{NP}}$ ):

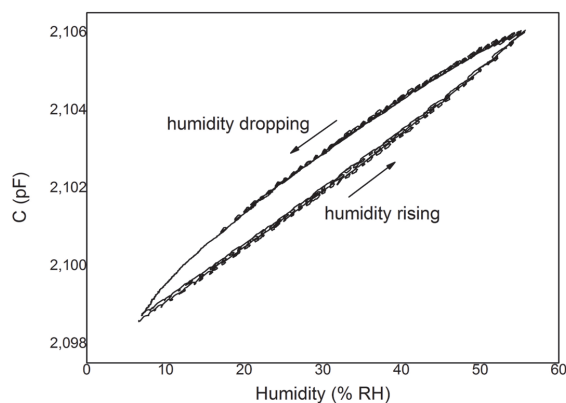
$$N_{\text{NP}} = \frac{V_{\text{layer}} \times \text{vol. \% NP}}{\frac{4}{3} \pi r^3} \quad A_{\text{NP}} = N_{\text{NP}} \times 4 \pi r^2 = \frac{3 V_{\text{layer}} \times \text{vol. \% NP}}{r}$$

## References

- [1] J. Park, J.-H. Bae, W.-H. Kim, M.-H. Kim, C.-M. Keum, S.-D. Lee, J.S. Choi, Effects of Interfacial Charge Depletion in Organic Thin-Film Transistors with Polymeric Dielectrics on Electrical Stability, *Materials*, 3 (2010) 3614.
- [2] M.E. Roberts, N. Queraltó, S.C.B. Mannsfeld, B.N. Reinecke, W. Knoll, Z. Bao, Cross-Linked Polymer Gate Dielectric Films for Low-Voltage Organic Transistors, *Chemistry of Materials*, 21 (2009) 2292-2299.
- [3] H. Kim, J.-H. Bae, S.-D. Lee, G. Horowitz, An effective method to minimize the leakage current in organic thin-film transistors by using blends of various molecular weights, *Organic Electronics*, 13 (2012) 1255-1260.
- [4] C.-S. Liao, J.-S. Wu, C.-F. Wang, F.-C. Chang, Modification of Polymer Substrates with Low Surface Free Energy Material by Low-Temperature Cured Polybenzoxazine, *Macromol. Rapid Commun.*, 29 (2008) 52-56.
- [5] S.V. Patel, T.E. Mlsna, B. Fruhberger, E. Klaassen, S. Cemalovic, D.R. Baselt, Chemicapacitive microsensors for volatile organic compound detection, *Sensors and Actuators B: Chemical*, 96 (2003) 541-553.
- [6] T.E. Mlsna, S. Cemalovic, M. Warburton, S.T. Hobson, D.A. Mlsna, S.V. Patel, Chemicapacitive microsensors for chemical warfare agent and toxic industrial chemical detection, *Sensors and Actuators B: Chemical*, 116 (2006) 192-201.

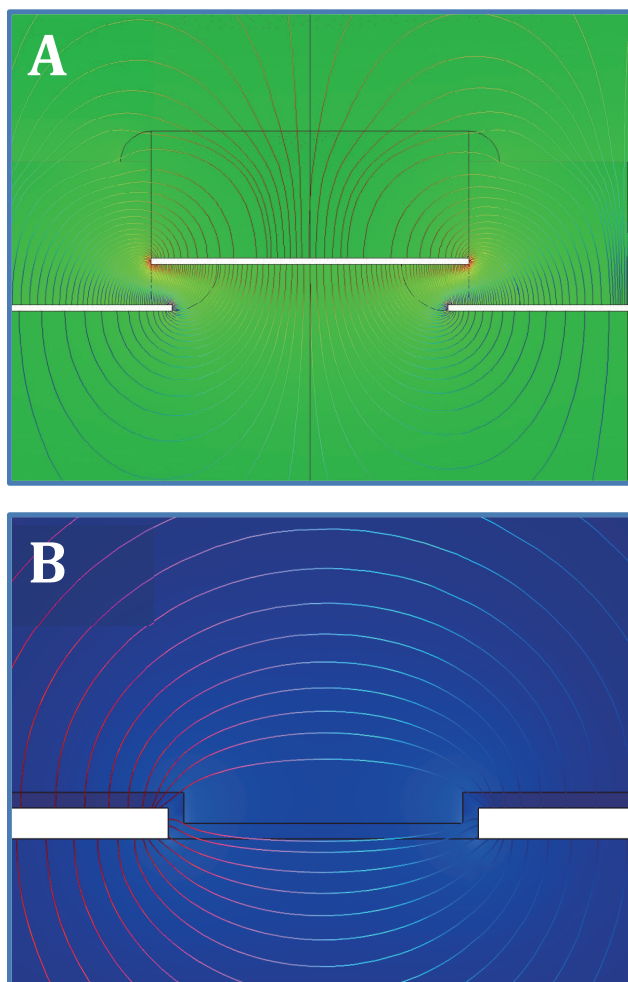
### C. Excellent Gas Sensing Performance at Room Temperature of Nanogap Interdigitated Electrodes for the Detection of Acetone at Low Concentration

The response of the sensor towards water (humidity) was measured by consecutive up and down ramps of humidity. Here, one ramp from 5 to 55 %RH was done in 30 minutes. **Figure S1** shows two curves going up in humidity and two going down. The figure clearly shows some hysteresis. For increasing humidity, the capacitance shows a linear increase with humidity. The slope of the curve was fitted to 0.15 fF/%RH, with an  $r^2$  of 0.999. When decreasing humidity, the capacitance also decreased, but slower than expected based on the upward curve.

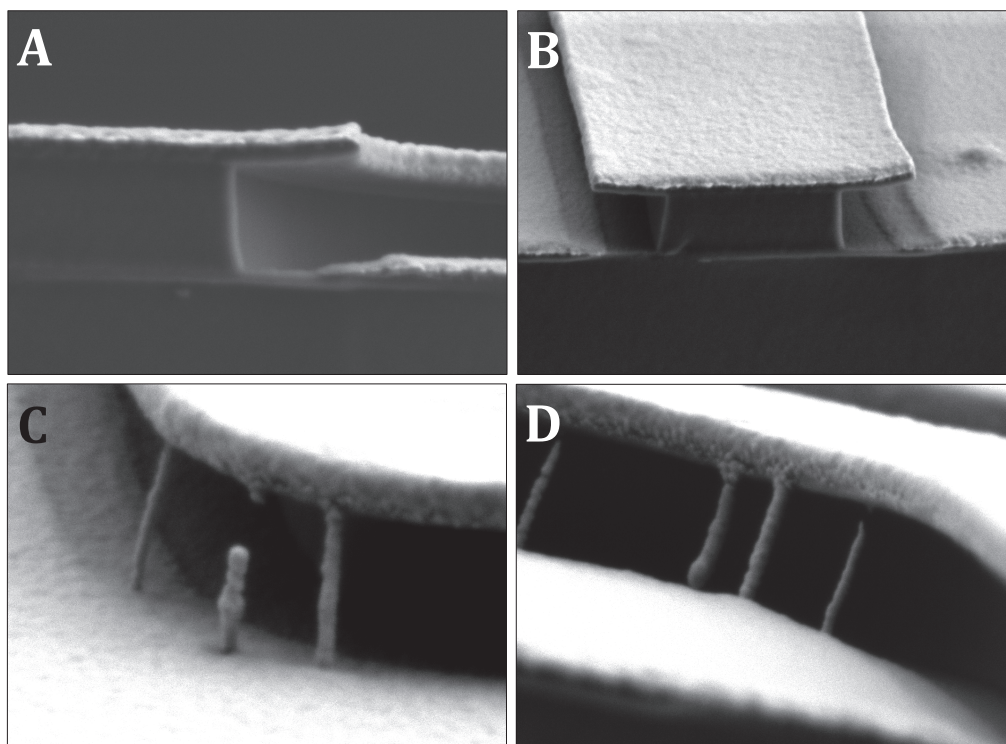


**Figure S1.** Capacitance as a function of humidity for a nanogap sensor coated with PVPH. Two upward and two downward curves are displayed.





**Figure S2:** Electric field intensity (color map), electric field lines and potential (color map on lines) composed of two electrodes (white) covered in a polymer film, supported by silicon nitride, in air environment. Left: a typical nanogap capacitor (250nm vertical spacing, 130nm horizontal overlap, 800nm polymer thickness). Right: a typical micro-IDE ( $10\text{ }\mu\text{m} \times 0.1\text{ }\mu\text{m} \times \text{length}$ ,  $1\text{ }\mu\text{m}$  spacing). The color maps have the same scale: the maximum field intensity inside the nanogap is a factor of  $\sim 3$  higher and the volume is much larger.



**Figure S3:** SEM images of cross-section at a pair of electrodes shown nanogap: Side view – (A) and top view at an angle of 60 degree – (B). Close-up SEM images of several defects during nanogap IDEs fabrication process that leads to capacitive short-circuits of the devices, thus production yield decreases at larger scale.

## D. Improving the Limits of Detection in capacitive sensors systems

### Measurement Results of the Capacitance Interface

A series of software acceptance test was designed in order to test the capacitance interface. These tests consisted of:

- Determining the resolution of the sensor (goal  $\leq 10$  fF)
- Determining the speed of the conversion (goal  $\geq 4$  samples per second)
- Determining the noise floor of the sensor (goal  $< 10$  fF)
- Determining the linearity of the converter (goal: to be able to linearize the output)

In order to measure this data, test software was developed to obtain a stream of data. This RS232 output data was logged and fed to Excel for further analysis. The output data of the register of channel A0 is represented in a 28 bit word. This data can be used to calculate the added capacitance or capacitance change. Figure 3 shows the tank circuit of the FDC, consisting of a known capacitance (C) together with the parasitic capacitance of the PCB and inductance (L). Together these components will resonate at certain frequency given by:

$$F_{res} = \frac{1}{2\pi\sqrt{L*C}} \quad (1)$$

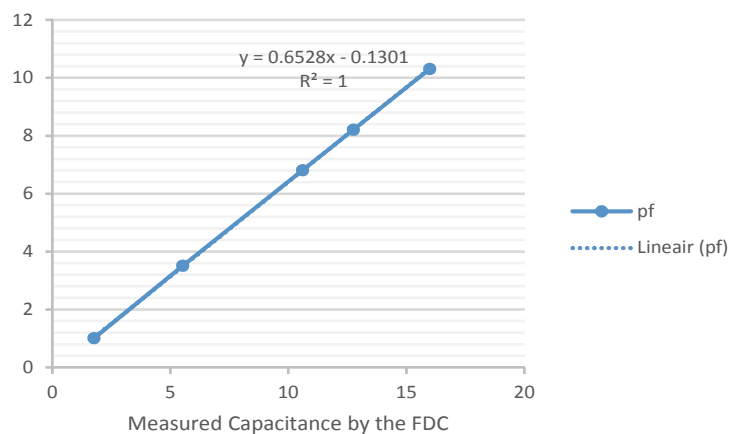
Where L is the inductance and C is the combined capacitance. The datasheet suggests an operating frequency between 10 kHz and 10 MHz and used an inductor of 18  $\mu$ H and a capacitance of 33 pF with additional 20 pF as a result of PCB wiring, resulting in a resonating frequency of 5.15 MHz. After initialization of the FDC this frequency was verified using an oscilloscope, keeping in mind that the probe adds capacitance and therefore influences the tank frequency. The 40 MHz internal master clock was used for comparison of the result of the output buffer. The output register of channel A0 can now be used to verify this.

$$F_{sensorA0} = \frac{f_{reference} * DATA\_REGA0}{2^{28}} \quad (2)$$

Where  $f_{reference}$  is the internal oscillator frequency of 40MHz and  $DATA\_REGA0$  is the value from the output register. This value provides the current frequency of the tank. This frequency can be used to calculate the additional capacitance of the tank when Equation (1) is rewritten to:

$$C_{sensor} = \frac{1}{L * (2 * \pi * F_{sensorA0})^2} - C \quad (3)$$

Where  $L$  is the inductance,  $F_{sensorA0}$  is the calculated value of Equation 2 and  $C$  is the calculated combined bare IDE capacitance. When a delta value of the capacitance is required, first the  $L$  and combined  $C$  are measured, and this value is subtracted from any new measurement. Note that because a delta capacitance ( $\Delta C$ ) value is used, the capacitance variance can also be negative.

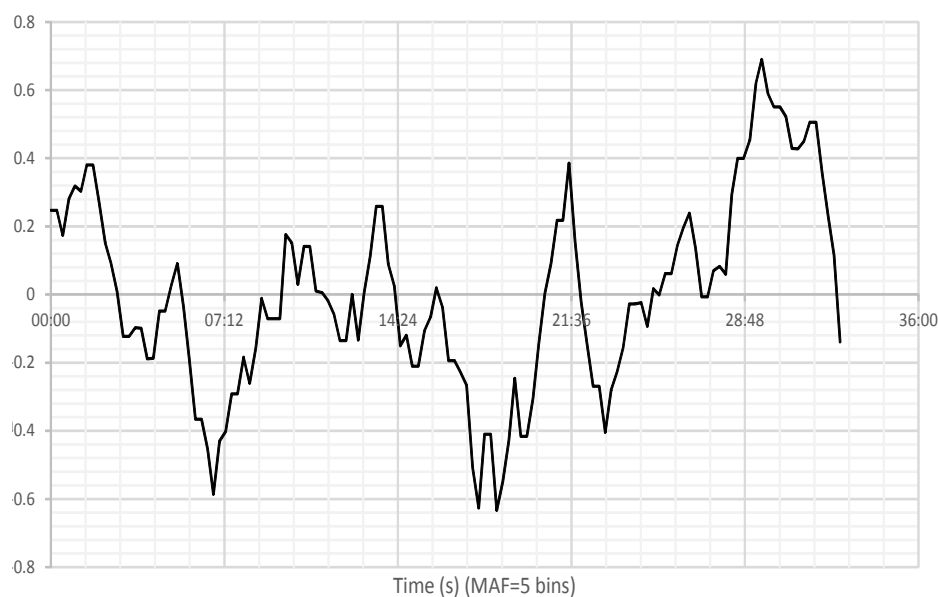


**Figure S1.** Linearization graph of the FDC2212 against the Hameg H8018

The interface is used to measure acetone concentrations, meaning that the absolute capacitance is not an issue but the linearity is and must therefore be measured. This was done by adding a known capacitance to the LC tank and calculating the results. Five capacitors were selected in the range of 1 to 10 pF and measured with a Hameg H8018 LRC meter. The output data of the FDC was fed through a five-tab moving average filter (MAF) 166

to smooth the output. Figure S1 shows the result of these measurements plotting the Hameg results against the FDC.

Here we observe that the standard deviation is equal to one, suggesting that the system does not need linearization. After this, the code was modified to constantly output values on the terminal with a frequency of 4 Hz while logging the data for further analysis. The data shows that the interval frequency of 4 Hz, well within the minimum conversion speed of 26 ms per sample, is stable. The FDC can handle faster speeds, up to 100 samples per second (Sps) at the cost of resolution. The FDC is set to maximum resolution in this application and kept at this setting for the rest of the measurements. Then, the FDC2212 was placed in open space and samples were collected over a period of 30 seconds. This data was modified using the method described above in order to obtain a value for  $\Delta C$ . This data was plotted in Figure S2 to estimate the noise figure in open space.



**Figure S2.** Noise figure of the FDC 2212 in femto farads

It was observed that during this interval the  $\Delta C$  was a little under 1.3 fF, a factor 7.5 better than the minimum goal of 10 fF. The smallest resolution step at the highest tank frequency (48 MHz) is 0.3 fF. This minimum resolution would improve with a lower LC oscillator value.

This concludes the measurements on the capacitance interface. At this time this noise figure and its resolution and noise floor are acceptable and this configuration was deemed acceptable for use in the SMS.

## Summary

The need of detecting acetone in ambient environment in laboratories and factories to monitor leakage and prevent accidents for human safety and health protection has involved numerous studies. Also, in human breath, acetone at ppm level is present amongst more than two hundred kinds of other volatile organic compounds. The development of reliable gas sensors for breath analysis is aimed to detect acetone at sub-ppm level in human breath for diabetes diagnosis. Field effect transistor based gas sensors have shown great potentials in detecting analytes at molecular level.

In a first approach fluorinated-terminated monolayers have been formed on silicon nanowires, that can detect an organic gas (2-octanone) at 0.5 ppm level. Surface formation and stability of these fluorinated monolayers on silicon nanowires have been characterized; Preliminary results towards VOCs have shown high-quality monolayers in various extreme conditions with good surface passivation.

As a second approach new nanogap IDEs structures have been developed for acetone detection, and sensing performance could be enhanced by using a nanocomposite (PVPH) sensing layer. Adding functionalized silicon nanoparticles in the PVPH polymer network, a higher sensitivity has been obtained. The IDE-PVPH devices demonstrated good reproducibility after multiple cycles of gas exposure. By reducing the gap-width to the nanoscale, the sensitivity of the device in acetone detection is increased drastically. A detection limit with nanogap IDEs is found to a level of 10 ppm when using PVPH as the sensing layer. Both micro and nano-gap IDEs operate at room temperature and show a good stability even after long-term storage. At room temperature, the detection limit of nanogap capacitive sensors depends heavily on the thermal and mechanical stability of other (parasitic) components that limit the resolution of the measurement. Emphasis is given on the nanostructure of nanogap IDEs; this type of capacitive sensors provide a larger dynamic range of the capacitance as compared to micro IDEs and herewith the signal to noise ratio is considerably improved. The results illustrate an improvement in measurement resolution from pico farads to femto farads. When using nanogap structures, a larger absolute change in capacitance will improve thus the detection limit.

### *Summary*

---

Both micro and nano gap sensors showed a relative change of 0.2 % with respect to the bare IDE capacitance and the limit of detection increased by a factor of 12. Further downscaling feature sizes in micro and nano IDE structures are promising for the development of novel portable gas sensors that are applicable in many fields such as industrial and laboratorial security. They promote a new generation of gas sensors for detection of a variety of VOCs at low concentrations in environmental air monitoring as well as disease diagnosis.



## Samenvatting

Er zijn verscheidene onderzoeken gedaan naar het meten van aceton in laboratoria en fabrieken, om de veiligheid en gezondheid van de mensen die daar werken te waarborgen. In onze adem is aceton aanwezig in *ppm* hoeveelheden, tussen meer dan tweehonderd andere vluchtige organische verbindingen. De ontwikkeling van betrouwbare gassensoren voor ademanalyse in deze thesis is gericht op het bespeuren van aceton in adem op *sub-ppm* niveau voor diagnose van diabetes.

Eén aanpak was het ontwikkelen van nieuwe *nanogap IDE* (elektrodeparen met een kleine onderlinge afstand). De gevoeligheid nam toe na het toevoegen van een gevoelige laag bestaande uit nanocomposiet, poly(4-vinylphenol) (PVPH). Het toevoegen van gefunctionaliseerde silicium nanodeeltjes had een aanvullende verbetering tot gevolg. Zelfs na herhaaldelijke blootstelling aan gas, gaf deze methode reproduceerbare resultaten. Door de sensoren te verkleinen tot op de nanoschaal, waren we in staat om de gevoeligheid drastisch te vergroten. De detectielimiet van *nanogap IDE* werd vastgesteld op 10 ppm bij het gebruik van PVPH als gevoelige laag. Zowel *micro-* als *nanogap IDEs* werken bij kamertemperatuur en laten goede stabiliteit zien, zelfs op lange termijn. De detectielimiet van *nanogap* sensoren bleek sterk afhankelijk van de thermische en mechanische stabiliteit van, parasitaire componenten. Dit limiteerde de resolutie van de metingen. Maar de verkleining naar de nanoschaal van de structuren in de sensor heeft ook grote voordelen. Deze innovatieve sensoren hebben een groter bereik in capaciteit dan conventionele IDE op microschaal, hetgeen het signaal aanzienlijk verbetert; de resolutie van het signaal steeg van picofarad naar femtofarad. In *nanogap IDE* heeft eenzelfde absolute verandering in capaciteit een grotere relatieve verandering tot gevolg; derhalve verbetert dus de detectielimiet. Deze kon met een factor 12 worden verbeterd.

Een andere aanpak was het vormen van gefluorineerde monolagen op silicium *nanowires*. De vorming en stabiliteit daarvan is gekarakteriseerd. Het leverde monolagen van hoge kwaliteit op met goede oppervlakte-passivatie onder verschillende extreme omstandigheden. Deze sensoren konden een gas (2-octanone) waarnemen bij een concentratie van 0.5 ppm.

Het toepassen van fysische fenomenen die exclusief plaatsvinden op de nanoschaal is een belangrijk instrument in het ontwikkelen van de volgende generatie draagbare sensoren voor de detectie van organische verbindingen bij lage concentraties in zowel atmosferische controle als medische diagnostiek. Er zijn uiteenlopende andere toepassingen denkbaar, bijvoorbeeld in het waarborgen van gezondheid en kwaliteit in zowel industriële als academische sectoren.

## Acknowledgements

Never thought that I could come this far, 13 000 km away from home and now I have the opportunity to defense my work for the degree of Doctor. This period is tremendously memorable and it has become a special part in my life. And I know these words would never be enough to express my appreciation to everyone who stands by my side for this important period of life, to care, to cheer me up and help me reach out my dream...

With all my gratefulness, I would like to thank Prof. Cees van Rijn and Prof. Han Zuilhof for giving me this opportunity to pursue my PhD dream. Your guidance allowed me to learn, to work and further grow in this ambitious and challenging project. Cees, you took care and watched every step I have taken in the last four years. You always encourage me and believe in my capability without any doubt. Thank you for your helpful advice, your inspiration with inputs in innovations and technology, and also, our countless discussions about industry-oriented research topics. Han, thank you for your supervision and guidance not only as a supervisor in the initial stage of my research but also as an 'open-armed' teacher with your passion in Chemistry that you have transferred to a juvenile student like me during endless lessons when I was at my very first step in Chemistry. Each day with you is a valuable lesson I could carry with me in my *journey of Knowledge*.

I am especially thankful to Prof. Hossam Haick and Bin Wang from Israel Institute of Technology for the fruitful collaboration of studying the sensing properties of the monolayers in Chapter 2, Dr. Hien Tong from Nanosens B.V. for his unlimited supports throughout this project, and Dr. Franc van der Bent from University of Applied Sciences Utrecht for his technical supports and insightful discussions. Many thanks to all Aquamarijn members for discussing all scientific topics, together with lots of humorous in-life stuffs, for your kind assistance and making our Aquamarijn feel so homey whenever I am working with you.

#### *Acknowledgements*

---

I would like to extend my deepest gratitude to all staff members of Organic Chemistry Laboratory. You have contributed great support to the success of all PhD students in the department. As years passing by, we fly up high towards the destination of Career and Success while your every-day hard work turns your hairs into the colour of wisdom and thoughtfulness, 'Platinum'. You appear with all beautiful memories in our daily mentioned word: "ORC".

Special thanks to my mentor Sidhu for your extensive scientific guidance and discussions, your kindness and help during these entire four years. You always support me with humongous efforts to my research. You thoughtfully guide me through all challenges from the day I started working in the lab till this special moment. Sidhu, you have witnessed my whole PhD life, we have shared great talks, funs and all highs and lows in our life. Many thanks Anke and Pepijn for being my paranymphs with great pleasure. Thanks to all my office mates in Helix, who always bring such a delightful atmosphere everyday I come to work. I would also like to thank all my past and present colleagues during my PhD time in Wageningen from 2013 to 2017 for your help, collaboration work and all activities we had together.

To my entire dearest friends who are always around me, in the Netherlands, especially, in Wageningen and abroad, it was a wonderful time I had with you, with all fun and meaningful things we shared. You have made every corner we have been visited become more beautiful in my thoughts when I have you around me. Thank you for being always there for me, cheering me up, warming up this place like a second home to me. My heart melts when you told me that you do not want me to leave the Netherlands to make our friendship become everlasting.

Most of all, I am grateful for my family for their endless and unconditional love and care, with their immense support of all time. Mom and Dad, I know I have lived a meaningful life as you always wish for me. And with all my love and warmth, thanks to someone special who has come along with me during this journey, understood me and received me the way I am at all time.

With much respect and appreciation,

Christie

174



## Author Biography

Quyen Nguyen Minh was born on November 14<sup>th</sup> 1987 in Hanoi, Vietnam. She received her B.Sc. degree from the Department of Physical Engineering and Nanotechnology and M.Sc. degree in the field of Nanomaterials and Devices from Hanoi Vietnam National University. From 2013 to 2017, she worked at Wageningen University and Research in the Netherlands as a Ph.D. student at Organic Chemistry Laboratory under direct supervision of Prof. Dr. Cees van Rijn and Prof. Dr. Han Zuilhof. During this time, she also contributed to several projects at Aquamarijn Research B.V. and Nanosens B.V. the Netherlands as a principle researcher. Her research interests include synthesis and modifications of nanomaterials, nanocomposite and polymer-based gas sensors for air quality control and medical diagnosis.

*Author Biography*

---

## List of Publications

### Journal Papers

1. Quyen Nguyen Minh, Anke Kuijk, Hien D. Tong, Franc van de Bent, Pepijn Beekman, Han Zuilhof, and Cees J.M. van Rijn. *Excellent Gas Sensing Performance at Room Temperature of Nanogap Interdigitated Electrodes for the Detection of Acetone at Low Concentration*. Royal Society of Chemistry Advances, **2017**.
2. Quyen Nguyen Minh, Anke Kuijk, Sidharam P. Pujari, Franc van der Bent, Hien D. Tong, Han Zuilhof, and Cees J.M. van Rijn. *Preparation and Gas Sensing Properties of Nanocomposite Polymers on Micro-Interdigitated Electrodes for Detection of Volatile Organic Compounds at Room Temperature*. Sensors and Actuators B: Chemical, Elsevier, **2017**.
3. Franc J.F. van der Bent, Quyen Nguyen Minh, Hien D. Tong, and Cees J.M. van Rijn. *Improving the Limits of Detection in capacitive sensors systems*. Measurement Science and Technology, **2017**.
4. Quyen Nguyen Minh, Sidharam P. Pujari, Bin Wang, Zhanhua Wang, Hossam Haick, Han Zuilhof, Cees J.M. van Rijn. *Fluorinated alkyne-derived monolayers on oxide-free silicon nanowires via one-step hydrosilylation*, Applied Surface Science, 2016.
5. Nguyen Nang Dinh, Nguyen Minh Quyen, Do Ngoc Chung, Marketa Zikova, Vo-Van Truong. *Highly-efficient electrochromic performance of nanostructured TiO<sub>2</sub> films made by doctor blade technique*. Solar Energy Materials and Solar Cells, 2011.
6. Nguyen Minh Quyen, Dang Hai Ninh, Pham Duy Long, Nguyen Nang Dinh. *Electrochromic properties of multi-layer WO<sub>3</sub> / TiO<sub>2</sub> films made by electrochemical deposition*. VNU Journal of science, Mathematics - Physics 27, 2011.

### Conference Papers

7. Nguyen Minh Quyen, Dang Hai Ninh, Pham Duy Long, Nguyen Nang Dinh. *Preparation and characterization of electro-chromic properties of multi-layer thin films with nano-heterojunctions*. 7<sup>th</sup> National Solid State and Material Science Conference, SPMS11, 2011.
8. Nguyen Minh Quyen, Marketa Zikova, Do Ngoc Chung, Nguyen Nang Dinh, VO Van Truong. *Characterization of electro-chromic properties of nano porous TiO<sub>2</sub> films made by doctor-blade method*. The first academic conference on natural science for Master and Ph.D. students from Viet Nam – Laos – Cambodia Science Symposium, 2010.
9. Nguyen Duc Cuong, Dinh Thanh Khan, Do Ngoc Chung, Nguyen Minh Quyen, Le Ha Chi, Nguyen Nang Dinh. *Study of Photoluminescent Properties of Heterojunctions of Polymeric Nanocomposites*. 6<sup>th</sup> National Physics Conference, 2009.
10. Dinh N.N., Quyen N.M., Chi L.H., Thuy T.T.C., Trung T.Q. *Characterization of Solar Cells using Nano Titanium Oxide and Nanocomposite materials*. International Workshop on Advanced Material for New and Renewable Energy (AMNRE-2009) in Jakarta, Indonesia, 2009.
11. Thuy T.T.C., Quyen N.M., Dinh N.N., *White light emission from InGaN LED chip covered with MEH-PPV polymer and inorganic powder Y<sub>2</sub>Al<sub>5</sub>O<sub>12</sub>:Ce film*. Hanoi International Symposium on Nano-Materials, Technology and Applications, NANOMATA, 2009.



---

The research described in this thesis was supported by NanonextNL (10A.05), a micro and nanotechnology consortium of the Government of the Netherlands and 130 partners.

Financial support from Wageningen University for printing this thesis is gratefully acknowledged.

Thesis layout is designed by Q. Nguyen Minh.

Cover page includes a high-resolution SEM image of a nano-gap (250 nm).

Printed by Ipskamp Printing B.V., Enschede, The Netherlands.

